University College London

Formation and flow of droplets in complex fluids in microfluidic channels

by

Evangelia Roumpea

Submitted to the Department of Chemical Engineering for the degree of **Doctor of Philosophy**

March 2019

Declaration

I, Evangelia Roumpea, confirm that the work presented in this thesis is my own. Where information has been derived from other sources, I confirm that this has been indicated in the thesis.

March 2019

London, United Kingdom

Abstract

In this thesis, the flow dynamics and characteristics of liquid-liquid, organic-aqueous flows in small channels were studied for cases when the aqueous phase is a complex fluid. In particular, polymeric non-Newtonian solutions and solutions with surfactants were used to investigate the effects of two different physical properties i.e. shear-thinning viscosity and interfacial tension, on two-phase flows. The organic Newtonian phase was a silicone oil, with 0.0046 Pa s viscosity. For the studies with non-Newtonian fluids, two aqueous glycerol solutions containing xanthan gum (1000 and 2000 ppm) were used. The two immiscible phases were brought together in a glass T-junction microchannel (with 200 μm inner diameter), and the effects of flowrate and viscosity on the plug flow characteristics and velocity fields were examined. Experiments were carried out both at the inlet and in the main part of the microchannel. For the studies with the surfactant solutions two ionic surfactants, C_{12}TAB (50 mM) and C_{16}TAB (5 mM) were added in the water-glycerol solution separately. In this case, a flow-focusing channel inlet was used (with cross-junction equal to 190 μm x 195 μm). For all experiments, an innovative micro-Particle Image Velocimetry (μPIV) technique was developed as part of this project. In this technique, two laser wavelengths illuminated two different particle types, each seeded in one of the phases of the two-phase mixture, in order to capture the shape of the interface and to measure the velocity fields in both phases simultaneously.

From the studies with the non-Newtonian aqueous phases, two different flow patterns were identified, namely plug and parallel flow, depending on the competition among interfacial, inertia and viscous forces. The plug flow was further investigated because it offers enhanced transport rates and has many applications in (bio) chemical analysis and synthesis. It was found that in the squeezing regime the plug formation at the T-junction could be divided in three discrete stages: expansion, necking, and pinch-off. The experimental results revealed that the organic plugs formed in the non-Newtonian solutions had larger tip (bullet-shaped profile) and neck curvatures and smaller neck widths compared to the Newtonian ones. In addition, an increase in xanthan gum concentration shifted the break-up location of the neck of the forming plug further downstream inside the channel and resulted in higher continuous phase velocities. Based on the velocity profiles and the geometric characteristics of the forming plugs, the forces acting on them were estimated. It was found that drag forces gradually increased and overcame

the surface tension ones in the beginning of the pinch-off stage changing the curvature of the neck from convex to concave.

The hydrodynamic characteristics of the plug flow of the organic phase in the continuous non-Newtonian aqueous solutions were further studied in the main channel, downstream from the T-junction inlet. With increasing polymer concentration, longer plugs were produced with increased film thickness around them due to the increase in visocity. From the shear rate profiles, it was found that the polymer solution was in the shear-thinning region while the viscosity was higher in the middle of the channel compared to the region close to the wall. The velocity profiles obtained from the PIV measurements showed that the addition of xanthan gum resulted in higher plug velocity. Within the non-Newtonian slug, the velocity profiles were found to be flat in the middle of the channel as expected for a power law fluid, while the circulation times were increased with the concentration of xanthan gum.

When the surfactants were employed in the aqueous phase, three distinct drop formation stages were also identified, namely expansion, necking and pinch-off for all solutions studied. The surfactant-laden solutions produced smaller drops with larger tip curvature than the surfactant free system. The forces acting on the forming drop were estimated and showed that the drag force overcame the interfacial tension force at the transition between the expansion and necking stages. During this transition, the curvature of the neck of the forming drop changed from convex to concave while the thinning rate of the neck increased. The velocity profiles showed that during the expansion stage, an internal circualtion appeared at the centre of the forming drop which gradually weakened as the droplet moved into the main channel. This circulation was less prominent in the surfactant-laden system which was attributed to the accumulation of surfactants at the drop tip. The averaged velocity fields revealed that the addition of surfactants increased the local velocity difference between the two phases compared to the surfactant-free case, for the same phase flowrates.

Impact statement

'We are at the very beginning of the exponential expansion of microfluidics'

Dr. Adrien Plecis, CSO and co-founder of Elveflow, France

The importance of technologies based on microfluidics has increased significantly over the last two decades due to numerous applications in (bio)chemical synthesis and analysis, healthcare, food industries and enhanced oil recovery. Understanding, thus, the formation and flow of droplets in small conduits is an essential step to properly design small-scale multiphase systems.

More specifically, understanding the interaction of oil droplets with aqueous phase in small scales is the primary concern for oil companies globally as more than 50% of the world's discovered oil is inside reservoirs with high degree of heterogeneity and complex pore structures. During the oil and gas drilling a significant percentage of crude oil remains trapped in porous wells requiring a large amount of pressure to push the oil from the well and process it further. Injection of a dilute solution of an aqueous-soluble polymer or surfactant can alter the properties of the aqueous phase in order to improve oil mobility and increase oil production rates (Madani et al., 2019; Pal et al., 2018).

The findings of this thesis offer insights into the effects of polymers and surfactants on oil droplet formation and displacement in small conduits and can be used to validate numerical tools for enhanced oil recovery. Contrary to many studies in the literature that have focused on droplet formation in Newtonian fluids with low viscosity, solutions with non-Newtonian rheology and complex behaviour are used in the current study. On top of that, a novel two-colour micro-Particle Image Velocimetry (PIV) technique has been developed and used to study the dynamic evolution of the interfaces and the velocity profiles in both phases simultaneously.

Two aqueous glycerol solutions containing xanthan gum at 1000 ppm and 2000 ppm were used to investigate the shear-thinning non-Newtonian behaviour. The formation and flow of oil droplets inside these complex flows were experimentally investigated in a quartz microchannel (200 μm ID) using the two-colour micro-Particle Image Velocimetry technique. The results of this work were published and received 864 downloads in 1 year (AIChE Journal's top 20 most

downloaded papers) generating immediate impact on the field of two-phase flows in microchannels.

In addition, the droplet-based microfluidics technology has been used by academia and industry to generate multiform emulsions for a wide range of applications with high throughput such as encapsulation, chemical synthesis and biochemical assays. Surfactants are an essential part of this microfluidic technology as they both facilitate droplet formation and are involved in the stabilization of droplet interfaces by acting as electrostatic barriers against droplet coalescence. As a result, they increase the emulsion stability. Understanding, thus, the effects of different absorption kinetics of surfactants on droplet formation is crucial for the production of stable emulsions (Li et al., 2019). In collaboration with the University of Birmingham (as part of a large EPSRC funded research programme named Memphis Multiphase), the formation of an aqueous droplet in an organic continuous phase was studied experimentally inside a flow-focusing microchannel in the presence of surfactants. The two-phase flow regime transitions were studied in detail using the two-colour micro-PIV technique leading to the development of validated simulation tools for the industrial and academic community. The drop formation process and the velocity profiles in both phases were also studied and published in two journal articles and presented in academic conferences and industrial consortiums. The findings offer an insight into the design of the microfluidic devices for droplet formation and can be used by researchers to validate numerical models for droplet production in microscales. Also, the results on surfactant dynamics can be utilized to optimize the emulsification process in food and cosmetic industries.

Engagement with the public at science events and outreach activities like UCL Open Days, Summer Schools and Memphis Showcases, by demonstrating microfluidic experiments, raised awareness of the microfluidic technology and its applications in chemical reactions, separations, emulsifications and inkjet printing.

Refereed journal papers

Chinaud, M., Roumpea, E. and Angeli, P. 2015. Studies of plug formation in microchannel liquid–liquid flows using advanced particle image velocimetry techniques. Experimental Thermal and Fluid Science, 69, 99–110.

Roumpea, E., Chinaud M. and Angeli, P. 2017. Experimental investigations of non-Newtonian/Newtonian liquid-liquid flows in microchannels. AIChE, 63, 3599-3609.

Kovalchuk, N., Roumpea, E., Nowak, E., Chinaud M., Angeli, P. and Simmons, M. 2018. Effect of surfactant on emulsification in microchannels. Chemical Engineering Science, 176, 139-152.

Roumpea, E., Kovalchuk, N., Chinaud M., Nowak, E., Simmons, M. and Angeli, P. 2019. Experimental studies on droplet formation in a flow-focusing microchannel in the presence of surfactants. Chemical Engineering Science, 195, 507-518.

Roumpea, E., Chinaud M. and Angeli, P. 2019. Experimental study on plug formation in shear-thinning fluids using a T-junction microchannel. Manuscript submitted for review.

Acknowledgements

I would like to express my sincere gratitude to my supervisor Professor Panagiota Angeli for the immeasurable amount of support, guidance and encouragement she has provided throughout my PhD research. Her deep insight into this project has been a true blessing and I am truly honoured to have been able to do research under her mentorship.

Besides my supervisor, I would like to thank my second supervisor Dr. George Manos for his encouragement and his contribution in my work.

I would like also to thank Dr Maxime Chinaud for his collaboration, guidance and invaluable help with the experimental apparatus. Special acknowledgements go to Dr Dimitrios Tsaoulidis for the time spent with me discussing experimental techniques, for his encouragement, and his contribution with insightful comments and advices in my work. I want to express thanks to Professor Mark Simmons, Dr Nina Kovalchuk and Dr Emilia Nowak of University of Birmingham for their collaboration, fruitful discussions and help in my project. I would like to thank Dr Simon Barrass and Miss Becki Belgrave from UCL for their invaluable help in the lab. Finally, I would like to express my gratitude to Professor Spiros Paras and Professor Aikaterini Mouza of Aristotle University of Thessaloniki for their continuous support and help in my starting steps on the field of micro-fluidics.

I also want to acknowledge the UK Engineering and Physical Science Research Council (EPSRC) Programme Grant MEMPHIS, and TSI instruments for providing me the appropriate equipment to carry out the experiments.

Special acknowledgements go to all the PhD students and researchers in my group (ThAMeS Multiphase): Billy, Din, Eduardo, Giovanni, Kassandra, Kyeong, Maria, Marti, Nikola, Qi, Rashid, Simona, Teng, Vicky, Victor and Weheliye for sharing their lab experience with me and supported me in any possible way. I would also like to thank all my friends: Lina, Sofia, Zoi, Katerina, Dina, Stavros, Dimitris and Vasilis for their encouragement, moral support and understanding they have provided during my PhD studies.

Finally, I would like to express gratitude to my family, especially to my parents and my brother, for their love, belief and motivation. Without them, I would not have been able to face this challenge in my life.

Contents

List of figures

List of tables

Nomenclature

A	Cross-sectional area of the channel [m^2]
Bo	Bond number = $\frac{Dh^2 g\,(\rho_1 - \rho_2)}{\sigma}$ [dimensionless]
b	Penetration depth of a growing plug [μm]
Ca	Capillary number = $\frac{\mu \cdot u}{\sigma}$ [dimensionless]
Ca_C	Capillary number of the continuous phase [dimensionless]
Ca_D	Capillary number of the dispersed phase [dimensionless]
CMC	Critical micelle concentration [mM]
D	Inner diameter of the channel [μm]
D_D	Droplet axial diameter [μm]
D_{EFF}	Effective diffusion coefficient [$m^2\ s^{-1}$]
Dh	Hydraulic diameter of the channel [μm]
de	Effective particle diameter as appears on the camera [μm]
dp	Particle diameter [μm]
ds	Diffraction-limited resolution [μm]
F_D	Drag force [$kg\ m\ s^{-2}$]
F_{MAX}	Maximum force acting on Du Nouy ring [$kg\ m\ s^{-2}$]
Fσ	Interfacial tension force [$kg\ m\ s^{-2}$]
g	Gravity = 9.81 [$m\ s^{-2}$]
h	Height of channel [μm]
K	Consistency index [$Pa\ s^n$]
L	Droplet length [μm]
La	Laplace length = $\sqrt{\frac{\sigma}{g(\rho_1 - \rho_2)}}$ [dimensionless]
L_P	Plug length [μm]
L_S	Slug length [μm]
L_W	Wetted length of the Du Nouy ring [m]
M	Magnification of lens [dimensionless]
M_W	Molecular weight [$g\ mol^{-1}$]
m	viscosity ratio, μ_C/μ_D [dimensionless]
N	Newtonian solution
NA	Numerical aperture of the microscope [dimensionless]

N1	1000ppm xanthan gum solution
N2	2000ppm xanthan gum solution
n_D^{20}	Refractive index at 20°C [dimensionless]
n	Flow behaviour index [dimensionless]
O	Silicone oil
Q_C	Volumetric continuous phase flowrate [$cm^3\ min^{-1}$]
Q_D	Volumetric dispersed phase flowrate [$cm^3\ min^{-1}$]
R	Gas constant = 8.314 [$J\ K^{-1}\ mol^{-1}$]
R_C	Inner radius of the channel [μm]
Re	Reynolds number = $\frac{\rho \cdot u \cdot D}{\mu}$ [dimensionless]
R_N	Neck width of plug [μm]
R_T	Radius of leading edge tip [μm]
T	Absolute temperature [K]
T_L	Time for the liquid to move from one end of the plug to the other [s]
T_P	Travel time of the plug [s]
t	Droplet formation time [s^{-1}]
U	Velocity [$m\ s^{-1}$]
U_C	Continuous phase velocity [$m\ s^{-1}$]
U_D	Dispersed phase velocity [$m\ s^{-1}$]
U_{MIX}	Mixture velocity [$m\ s^{-1}$]
U_P	Plug velocity [$m\ s^{-1}$]
U_S	Slug velocity [$m\ s^{-1}$]
V_{FILL}	Volume of a growing plug [μm^3]
V_T	Averaged velocity at the top part of droplet [$m\ s^{-1}$]
v	1 for non-ionic surfactants
	2 for ionic surfactants
v(r)	Poiseuille velocity profile [$m\ s^{-1}$]
W	Width of channel [μm]
W_C	Width of the continuous phase channel [μm]
W_D	Width of the dispersed phase channel [μm]
We	Weber number = $\frac{\rho \cdot u^2 \cdot D}{\sigma}$ [dimensionless]
W_N	Neck width of droplet [μm]
W_T	Width of plug [μm]

y_o	location of stagnation point [μm]

Greek letters

α	Filling volume of plug / width of main channel [dimensionless]
β	Constant based on T-junction inlet [dimensionless]
Γ_{CMC}	Surface coverage at CMC [mol m^{-2}]
$\dot{\gamma}$	Shear rate [s^{-1}]
δ	Film thickness [μm]
θ	contact angle [^{o}]
λo	Barrier filter for imaging [nm]
μ	Dynamic viscosity [Pa s]
μ_C	Dynamic viscosity of the continuous phase [Pa s]
μ_D	Dynamic viscosity of the dispersed phase [Pa s]
μ_{N1}	Dynamic viscosity of 1000ppm xanthan gum solution [Pa s]
μ_{N2}	Dynamic viscosity of 2000ppm xanthan gum solution [Pa s]
μ_0	Zero-shear dynamic viscosity [Pa s]
μ_∞	Infinite-shear dynamic viscosity [Pa s]
ρ	Density [kg m^{-3}]
σ	Interfacial tension [mN m^{-1}]
σ_{eq}	Equilibrium interfacial tension [mN m^{-1}]
σ_S	Surface tension [mN m^{-1}]
τ	Shear stress [Pa]
τ_{cir}	Circulation time [dimensionless]
τ_o	Yield stress [Pa]
$\tau_{1/2}$	Shear stress when viscosity is $\mu_0/2$ [Pa]

To my family

for their unconditional love and support

1. Chapter: Introduction

1.1 Motivation

The importance of microfluidic technology has increased significantly over the last two decades due to numerous applications in (bio)chemical synthesis and analysis, enhanced oil recovery, healthcare and food industries (Whitesides, 2006). Compared to large-scale processes, microfluidic systems (Figure 1.1) offer advantages in terms of low sample consumption, increased safety, fast processing, disposability and portability. Their small characteristic dimensions result in high surface-to-volume ratios, which enhance the importance of interfacial phenomena and allow better control over the flow patterns in multiphase systems. These properties lead to process intensification and to development of energy-efficient technologies that are promising to change chemical process industries (Angeli and Gavriilidis, 2008). To this end, microfluidic devices appear to be an attractive option for process analysis and for production. However, there are still many challenges regarding the understanding and application of multiphase microfluidic processes (i.e. flow patterns that form under different conditions, difficulty in scaling-out and integration of multiple functions).

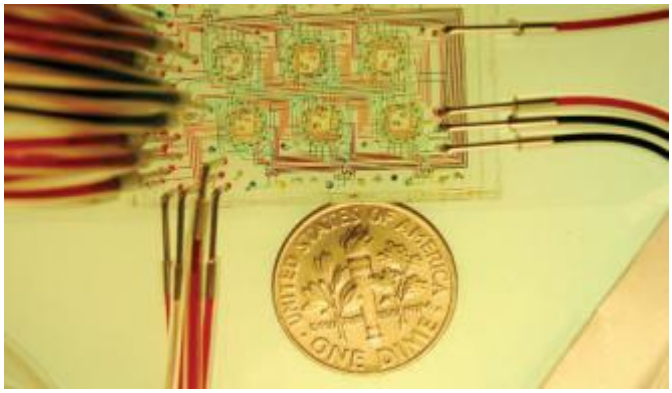

Figure 1.1: Typical microfluidic device with six micro-reactors for studies on microbial populations (Whitesides, 2006).

Microchannel multiphase flows have found many applications in areas such as chemicals analysis and synthesis, pharmaceuticals processing and thermal management systems (Chinaud et al., 2015). Flows in small scales are generally laminar and governed mainly by viscous and interfacial forces while inertial and gravity forces are small. The absence of turbulent effects and the increased importance of the surface tension forces favours the formation of regular and

well-defined flow patterns which can, however, be different to those observed in large-scale flows (Tsaoulidis and Angeli, 2016). Understanding the hydrodynamic properties of the different flow patterns and their transitions is an essential step to properly design small-scale multiphase systems.

In contrast to the large number of investigations on fully developed two-phase flows, there are few experimental studies on liquid-liquid droplet formation at the inlet of the channels, which provide detailed measurements of velocity fields and interface deformation. The difficulty arises from the high speed of the droplet formation process especially during the breakage of the droplet at the channel inlet. Different inlet geometries (e.g. T-junction, Y-junction, flow-focusing) have been studied in the literature (Anna, 2016; Chen et al., 2015; Garstecki et al., 2006; Gupta and Kumar, 2010; Steegmans et al., 2010) to produce droplets of controlled size at high frequency that have found applications in chemical reactions, separations, emulsifications, inkjet printing and pharmaceuticals (Fu et al., 2015). However, most of the studies are concerned with droplet formation in Newtonian fluids with low viscosities although fluids with complex behaviour (e.g surface active agents) and non-Newtonian rheology are widespread in industrial applications. The flow behaviour of these systems in small channels is complicated, including flow through thin fluid layers, recirculation patterns within phases and convection induced by surface tension gradients. It is very difficult to explain all these dynamic phenomena in micro-scale by using conventional measurement techniques. Therefore, the right experimental approach to the study of micro flows is very important and critical for the understanding of liquid-liquid flows especially when complex fluids are involved.

1.2 Scope and objectives

The main aim of the thesis is to study the formation and flow of dispersions of immiscible liquids in microchannels and the effects of non-Newtonian rheology and surfactants. For a better understanding of these complex flows, knowledge of the hydrodynamic properties and of the velocity fields in both liquid phases is necessary for evaluating the viscosity and interfacial tension effects. To this end, an innovative optical technique, namely two-colour Particle Image Velocimetry, was developed as part of this project to investigate the flow fields and shear rates in both liquid phases simultaneously.

For the study of the non-Newtonian, shear-thinning behaviour, two aqueous glycerol solutions containing xanthan gum were used at different concentrations. The effect of shear-thinning viscosity on the hydrodynamic characteristics, the droplet formation process and velocity profiles of both phases was examined for different flowrate conditions. In addition, the flow patterns and droplet formation process were studied for different surfactants that were diluted in the aqueous phase. For the investigations of interfacial tension effect on the droplet formation and velocity fields in both liquids, two ionic surfactants (C_{12}TAB and C_{16}TAB) were tested. The mechanism of droplet generation in the microchannels was examined for two different inlet geometries, namely a T-shaped junction and a flow-focusing junction. Both inlet designs have been widely studied and adopted due to the simplicity of fabrication, the ease of operation and the high stability and control they offer on droplet formation.

The objectives of the thesis can be summarized as follows:

- Develop a two-colour micro-PIV technique to measure the velocity fields in both phases simultaneously.
- Characterise the spatial configuration of the two phases during liquid-liquid flows.
- Analyse the hydrodynamic properties of the liquids during drop formation at the inlet i.e. drop size formed, tip and neck radius, film thickness under different liquid physical properties.
- Investigate the velocity profiles, recirculation patterns and shear rates during the drop flow.
- Develop an one-dimensional force balance model to estimate the relative importance of the forces acting on the forming drop, using the drop geometric characteristics and the velocity profiles obtained with PIV.
- Study the effects of shear-thinning viscosity and interfacial tension on the drop formation process in small channels.

1.3 Outline of thesis

The dissertation is structured in 7 Chapters. A brief introduction to the topic and the objectives of the thesis were given in the current Chapter 1 and a thorough literature review follows in Chapter 2. The aim is to outline the fundamental theory needed to understand the phenomena observed in the experiments. Starting with microfluidic devices, the different geometries used for droplet formation are discussed. An overview of the flow patterns that can occur in small channels is given together with a discussion of the physical mechanisms that

control the plug and droplet formation and flow. The theoretical background of the complex liquids used in the thesis and a review of the two-colour micro-PIV techniques are also discussed. Chapter 3 gives a detailed description of the materials, characterization methods, procedures and experimental setup used. In Chapter 4, the plug formation of a non-Newtonian and a Newtonian liquid is experimentally investigated in a T-junction microchannel. Using the two-colour Particle Image Velocimetry technique useful information regarding the effect of flowrate and shear-thinning viscosity on the hydrodynamic characteristics and the velocity profiles of both phases is obtained. A mechanistic model is also developed, based on the PIV data, to describe the evolution of the forces acting on the plug during the formation process. In Chapter 5, the plug flow of the above-mentioned non-Newtonian system is studied downstream from the T-junction. The results on plug length, film thickness and circulation patterns are presented and discussed in depth. Chapter 6 investigates the formation of an aqueous droplet in an organic continuous phase inside a flow-focusing microchannel in the presence of surfactants. The drop formation process and the velocity profiles in both phases in the squeezing and dripping regimes were studied in detail using the PIV technique. Finally, in Chapter 7, the conclusions of the thesis and recommendations for future work are given.

2. Chapter: Literature review

2.1 Multi-phase flows in microchannels

Research on microfluidic devices has significantly increased, over the last decades, driven by process intensification demands. Such systems have found several process engineering applications in, among others, chemical synthesis, emulsifications, pharmaceutical processes, and food industry. In this Chapter, the theory and literature describing the geometrical configurations of the microdevices and the dynamics of liquid-liquid flows in small scales are presented. The flow patterns that can be occurred in small channels are discussed together with explanations of the physical mechanisms that control the plug and droplet formation and flow.

2.1.1 Microfluidic devices

Microfluidic devices, with typical dimensions in sub millimetre scale, have gained importance over the last decades and are the subject of many studies related to intensified production and processing. Numerous applications of microcontactors can be found in mixing or separation procedures and in chemical reactions holding the promise of increasing efficiency and fast parallel processing. Microfluidic devices have several advantages compared to large scale systems offering confined, well controlled and safe process environment. Due to their small scale, the Reynolds numbers are usually small (laminar flow regime) which in the case of two-phase flows can provide a high degree of control on droplet or plug formation. In addition to that, the large surface-to-volume ratios enhance the role of surface tension over the gravitational forces leading to regular and well characterised flow patterns (Dessimoz et al., 2008; Gupta and Kumar, 2010). This high degree of control over operation and production that microchannels offer, is crucial for micro-reaction systems such as hydrogenation that require large surface area between immiscible phases (for mass and heat transfer) and controllable phase dispersion (Yao et al., 2018). In addition, the ability to precisely control flow within channels for biological applications such as DNA synthesis is critical for protein sequencing. Biotechnology industry manipulates flows by varying the electrowetting properties of the micro-channels.

In the early stages of microfluidic technology, research was meanly focused on single-phase flows. Considering, though, the increasing demand for process intensification, two-phase

droplet-based microfluidics was introduced and has been a rapidly growing scientific area in the last decades. Droplet-based microchannels have been designed to bring two or more immiscible fluids into contact with one another within a device of reduced size. This channel size reduction has been found to have different effects on different processes. As a result, a channel classification based on the hydraulic diameter was firstly adopted in literature. Mehendale et al. (2000) considered the channel sizes from 1 μm to 100 μm as microchannels, 100 μm to 1 mm as mesochannels, 1 mm to 6 mm as compact passages, and > 6 mm as conventional passages. Based on this preliminary classification a more general and slightly modified scheme (Table 2.1) has been suggested by Kandlikar and Grande (2002).

Table 2.1: Channel classification scheme.

Conventional channels	D > 3 mm
Minichannels	3 mm ≥ D > 200 μm
Microchannels	200 μm ≥ D > 10 μm
Transitional Microchannels	10 μm ≥ D > 1 μm
Transitional Nanochannels	1 μm ≥ D > 0.1 μm
Nanochannels	0.1 μm ≥ D

D: channel diameter

However, a criterion of channel transition that takes account not only the channel size but also the operating conditions and fluid properties is needed to express the forces (interfacial tension, viscous forces) during the flow. The following criterion that has been proposed by researchers (Garstecki et al., 2006) is based on different dimensionless numbers, among which Laplace length, La and Bond number, Bo described as:

$$La = \sqrt{\frac{\sigma}{g(\rho_1 - \rho_2)}} \qquad \text{(Equation 2.1)}$$

$$Bo = \frac{Dh^2 g\,(\rho_1 - \rho_2)}{\sigma} \qquad \text{(Equation 2.2)}$$

The dimensionless numbers in Equation 2.1 and Equation 2.2 refer to two-phase systems where σ is the interfacial tension, g is the gravitational acceleration, Dh is the hydraulic diameter of the channel and ρ_1, ρ_2 is the density of phase 1, phase 2 respectively. For the gravitational force to be negligible the Bond number, which express the ratio of gravity to interfacial tension, has to be less than 1. This criterion is the most frequent used to categorize the channels.

The geometry of the inlet can determine the local flow fields and consequently the interfacial configuration of the fluids. Different microchannel geometries have been studied in the literature (Anna, 2016; Chen et al., 2015; Garstecki et al., 2006; Gupta and Kumar, 2010; Steegmans et al., 2010) in order to produce droplets or plugs with controlled size at high frequency for applications in chemical reactions, separations, emulsifications and inkjet printing. The most commonly used inlet configurations can be divided into three categories: *cross-flow*, *flow-focusing* and *co-flow* geometries (Figure 2.1). This discrimination of different geometries is based on the nature of the flow fields near the droplet detachment region. Also, the above categories have been characterized as passive methods of droplet formation where the interface is deformed only by the flow field at the inlet and not by external actuations or moving parts (as in the active methods of droplet formation) (Anna, 2016).

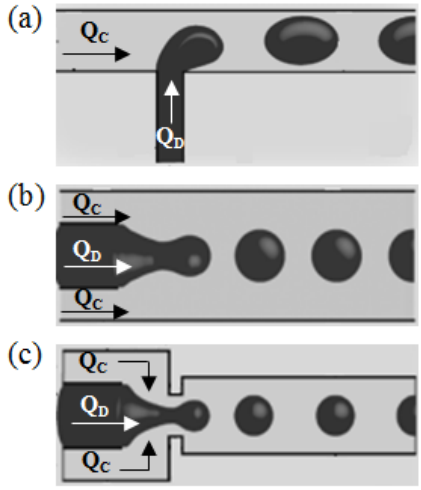

Figure 2.1: Typical microfluidic geometries used for droplet formation: (a) cross-flow stream in a T-shaped junction, (b) co-flow and (c) flow-focusing geometry. Q_D and Q_C represent the dispersed and continuous phase flowrate respectively. Source: Christopher and Anna (2007).

In cross-flow geometries, the continuous and the dispersed phase channels can meet at an angle in a Y-shaped junction (Dummann et al., 2003; Kashid and Agar, 2007) or perpendicularly in a T-shaped junction (Christopher et al., 2008; Garstecki et al., 2006). A typical example of a T-inlet can be seen in Figure 2.1a where the main channel carries the continuous phase flow and the orthogonal channel supplies the dispersed phase. The two fluids meet at the channel inlet forming an interface. The pressure that builds up in the continuous phase, distorts the forming droplet in the downstream direction until eventually the droplet detaches. The characteristic dimensions and the shape of the branches and main channel such as the width and the height have a significant effect on the size, length and detachment of the

droplets. The T-junction design has been widely studied and adopted due to the simplicity of fabrication and ease of operation, having only two inlets and one outlet (Chiarello et al., 2017).

During droplet formation in co-flow geometries (Figure 2.1b) the dispersed phase (Q_D) flows into the middle channel whereas the continuous phase (Q_C) flows through the two outside channels. The two immiscible fluids flow together until the shear stress exerted by the continuous phase on the forming interface leads to droplet breakup. Depending on the properties and velocities of the fluids, the dispersed phase can form a thin thread which eventually breaks into droplets either inside the junction or further down in the main channel (Utada et al., 2007). Despite the ease of operation that co-flow geometries offer, the fabrication process is still a challenge due to the difficulty in aligning the capillaries in a concentric manner.

The flow-focusing designs (Figure 2.1c), were an improvement of the co-flowing devices offering higher stability and control over droplet formation due to the confined and symmetrical geometry of the flow-focusing junction (Chen and Ren, 2017). The dispersed phase still has to be injected through the middle channel whereas the continuous phase flows through the two outside channels. The two fluids are then forced to flow through a small orifice that is located downstream in the main channel offering larger control over the droplet size. As discussed by Anna et al. (2003), the pressure and shear stresses exerted by the continuous phase on the dispersed phase leads to the formation of thin thread which eventually breaks forming the droplets.

Despite the fact that flows of mixtures of two immiscible liquids in small channels are very common in industrial processes (i.e. chemical and pharmaceutical industries include nitration, extraction, polymerization and highly-controlled formation of droplets for emulsions), their flow behaviour has not yet been fully understood. The main liquid-liquid flow characteristics and the flow patterns that can be occurred inside a small channel are detailed discussed in the following subsections.

2.1.2 Liquid-liquid flow patterns in microchannels

Depending on the channel properties (inlet size and geometry, channel dimensions and material, wettability), fluid properties (viscosity, surface tension, density) and experimental conditions (flow rates of fluids, pressure drop and temperature) liquid-liquid flows can generate different flow patterns inside the microchannels.

Dessimoz et al. (2008) studied the influence of Y- and T-shaped glass microchannels on liquid-liquid two-phase flow patterns. Based on their results, the Y-shaped microchannel was used to generate parallel flow (Figure 2.3f) while the T-shaped one generated plug flow (Figure 2.3b). Kashid and Agar (2007) experimentally investigated how different capillary diameters affect the boundaries of well-defined flow patterns (drop and plug flow, Figure 2.3a and b). For small capillaries, the most uniform flow behaviour (i.e. plug/drop flow) was observed at low and approximately equal flow rates of the phases. However, as the capillary size increases, higher and unequal flow rates are required to achieve similar results.

In addition, density, surface tension, and viscosity of liquids have an important effect on the flow configuration. Several authors (Boogar et al., 2013; Jovanovic et al., 2011; Zhao et al., 2006) have experimentally studied different liquid-liquid systems and how their physical properties affect the hydrodynamic characteristics of the flow and the corresponding flow patterns. As it is expected, different values of viscosity and surface tension showed different effect on both the flow pattern and the interfacial area.

Finally, operating conditions such as the phase flow rate ratio, the pressure drop, and the nature of the first fluid injected into the channel influence significantly the produced flow pattern map. Salim et al. (2008) investigated the effects of the wall wettability and the interfacial tension on the flow patterns of liquid-liquid systems inside glass and quartz microchannels. The authors found that depending on which fluid was injected into the channel, a different flow configuration occurred. The flow rates were also found to affect the flow patterns and the pressure drop. On the contrary, the microchannel material had no influence on the patterns revealing no difference between the glass and the quartz channel.

A number of liquid-liquid flow patterns have been identified in microchannels namely annular, parallel, drop and plug flow driven by the competition between interfacial tension, shear stress and pressure drop forces (Figure 2.2). As the dispersed phase grows inside the channel inlet, it obstructs the continuous phase resulting in a pressure difference across the emerging interface as well as in shear stresses. These two forces are opposed by the interfacial tension force, which resists deformation (Garstecki et al., 2006; Glawdel et al., 2012b).

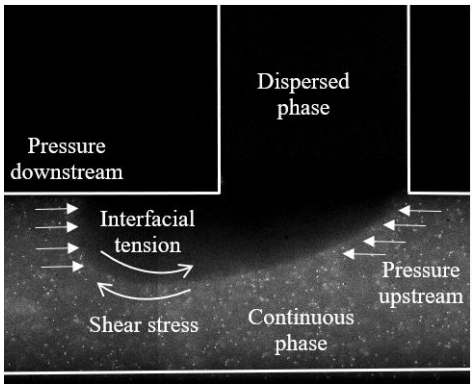

Figure 2.2: Schematic indicating the forces acting on the droplet during formation.

In order to define quantitatively the influence of these main forces on the flow patterns, dimensionless numbers are often used (Table 2.2). Depending on the dimensionless numbers, different flow regimes can be observed in a flow pattern map (Anna, 2016; Anna et al., 2003; Chiarello et al., 2015; Garstecki et al., 2006; Glawdel et al., 2012a; Kovalchuk et al., 2018; Steijn et al., 2007).

Annular and parallel flows are observed when inertial forces are dominating over interfacial forces (We > 1). Annular flow with either smooth or wavy interface (Figure 2.3c, d and e) occurs when one fluid occupies the space adjacent to the tube wall and surrounds the other fluid that flows in the centre of the channel.

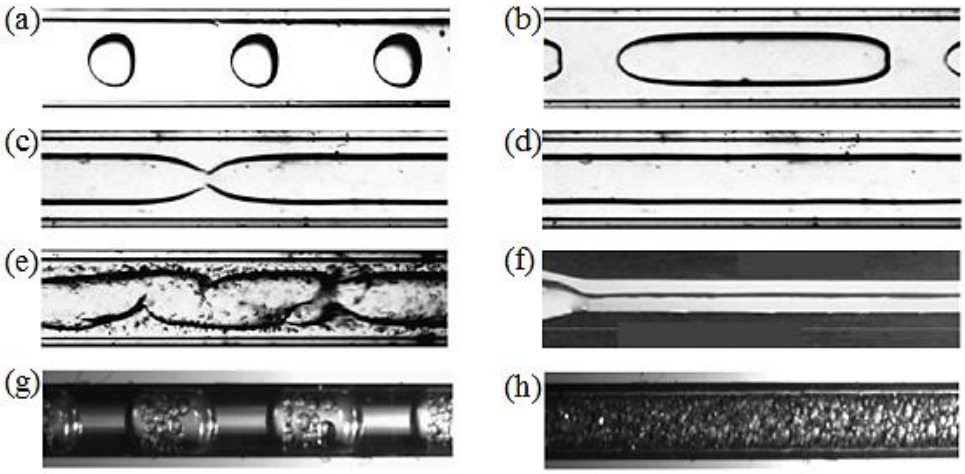

Figure 2.3: Flow patterns in microchannels (a) Drop flow (b) Plug flow (c) and (d) Annular flow with smooth interface (e) Annular – droplet flow with wavy interface (f) Parallel flow (g) Plug-dispersed flow (h) Dispersed flow (Foroughi and Kawaji, 2011).

Additionally, as it can be seen from Figure 2.3f the two immiscible liquids can be separated with the less dense liquid flowing on the top of the heavier fluid forming that way the parallel

regime. Combinations of flow patterns such as the plug-dispersed flow (Figure 2.3g) can also be achieved under specific conditions. During this regime, part of the continuous phase flows in the form of droplets into the plugs. The dispersed flow (Figure 2.3h) appears when the total flow rate is generally increased and fine droplets of one phase are formed into the other phase. These patterns can be further sub-divided to other flow regimes depending on the operational conditions and channel characteristics (Tsaoulidis and Angeli, 2016). Finally, drop and plug flow (Figure 2.3a and b) have attracted a lot of interest and have been extensively studied (Carrier et al., 2015; Dore et al., 2012; Jovanovic et al., 2011; Kashid and Agar, 2007; Riaud et al., 2018) due to the high degree of control over the hydrodynamics, the well-defined interface and the potential applications in (bio) chemical analysis and synthesis.

Table 2.2: Dimensionless numbers relevant to liquid-liquid flows.

Dimensionless numbers	**Definition**	
Reynolds number	$\frac{\text{Inertial forces}}{\text{Viscous forces}}$	$\text{Re} = \frac{\rho \cdot U \cdot D}{\mu}$
Capillary number	$\frac{\text{Viscous forces}}{\text{Interfacial tension forces}}$	$\text{Ca} = \frac{\mu \cdot U}{\sigma}$
Weber number	$\frac{\text{Inertial forces}}{\text{Interfacial tension forces}}$	$\text{We} = \frac{\rho \cdot U^2 \cdot D}{\sigma}$

Where ρ density, μ viscosity, U fluid velocity, D channel diameter , σ interfacial tension

Plug flow, where one phase forms elongated plugs with equivalent diameter larger than the channel diameter, is particularly favoured in small-scale processing as it enhances mass transfer rates. This is because of the circulation patterns within the dispersed phase plugs and the continuous phase slugs, which improve radial mixing, and the thin liquid films surrounding the plugs. These merits make plug flow an ideal pattern for improving reaction performance (Yao et al., 2018). Plug flow usually occurs at low flow rates for volumetric ratios of the two phases close to 1 (Su et al., 2013) whereas drop flow appears at higher flowrates of the phases.

Understanding the mechanisms of plug and drop formation in microchannels is one of the main aims of this thesis. To this end, the fundamental theory of plug and drop formation of immiscible liquids is examined further.

2.1.3 Plug and drop formation process in microchannels

Plug and drop formation inside a T-junction channel

The T-inlet configuration is one of the most commonly used for studies of plug formation due to the high level of control of the flow patterns and the simple design. During plug flow (Figure 2.3b), the dispersed phase forms the plugs whereas the continuous phase is the medium carrying the plugs. Figure 2.4 illustrates an example of plug formation in a T-junction inlet.

The plug formation process is controlled mainly by the competition between the interfacial tension, the shear, and the pressure drop forces. The shear stress and the increasing pressure inside the continuous phase (as the forming plug blocks the inlet) elongate and push the forming plug downstream whereas the interfacial tension acts against the plug deformation.

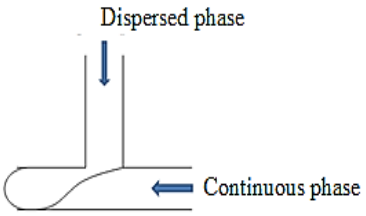

Figure 2.4: Example of plug formation inside a T-junction inlet.

The evolution of the forces and their dependence on fluid properties (surface tension, viscosity) and flow conditions of both phases have been investigated in a T-junction channel by several researchers (Christopher et al., 2008; Garstecki et al., 2006; Glawdel et al., 2012b; Husny and Cooper-White, 2006; Steijn et al., 2007). Depending on which of these three forces dominates on the break-up mechanism, different flow regimes have been identified, namely *squeezing*, *dripping*, and *jetting*.

In the squeezing flow regime, which occurs at low Capillary numbers ($Ca < 0.01$), the breakup of the plug is dominated by the excessive pressure that builds up in the continuous phase at the back of the plug as it forms and gradually blocks the main channel. Figure 2.5 presents typical steps of the plug formation in the squeezing regime inside a T-junction. The plug formation is generally divided into 3 stages namely expansion or filling, necking and pinch-off. Under constant dispersed phase flowrate, the plug expands from the dispersed phase channel into the main one filling the T-shaped inlet. During this expansion stage (Figure 2.5a-d) the volume of the plug (V_{FILL}) grows until it reaches a maximum penetration depth (b) which depends on the forces acting on the interface (Glawdel et al., 2012a). The forming plug

obstructs the T-inlet and restricts the flow of the continuous phase to a thin film on the channel walls.

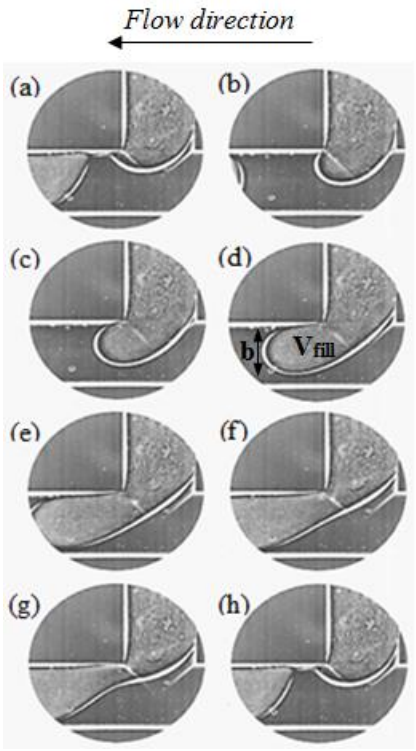

Figure 2.5: Typical plug formation cycle in the squeezing regime inside a T-shaped channel consisting of three stages: (a)-(d) expansion, (e)-(g) necking and (h) pinch-off stage. V_{FILL} and b represent the filling volume and the penetration depth of the growing droplet respectively.

As a result, the increasing pressure inside the continuous phase overcomes the interfacial tension force that resists deformation and 'squeezes' the plug neck (necking stage, Figure 2.5e-g). Under the effect of the continuous phase, the thinning rate of the neck accelerates leading eventually to the plug detachment (pinch-off stage, Figure 2.5h) (Anna, 2016). Several researchers have suggested different predictive models (either empirical or based on physics) to describe the plug size and the phenomena governing plug formation. Garstecki et al. (2006) who studied droplet formation in the squeezing regime inside a T-junction microchannel found that the size of droplets is determined only by the ratio of the volumetric flowrates (Q_D/Q_C) of the two immiscible liquids. They described the droplet formation by considering three main forces: the interfacial tension force resisting the break-up, the shear stress acting on the droplet by the continuous phase and the pressure difference across the droplet.

To investigate the impact of these forces on the droplet during the break-up process Garstecki et al. (2006) measured the droplet length, L, as a function of the flow rate ratio and suggested the following scaling law:

$$\frac{L}{D} = \alpha + \beta \cdot \frac{Q_D}{Q_C}$$ (Equation 2.3)

where L and D are the droplet length and the diameter of the channel respectively, α represents the dimensionless growth of the droplet (penetration depth /width of main channel), β is a constant which depends on the geometric characteristics of the T-junction and $\frac{Q_D}{Q_C}$ is the dispersed to continuous phase flowrate ratio. In the model of Garstecki et al. (2006) the fitting parameters a and β are assumed to be of the order of one. This simple scaling law was developed to predict the size of droplets during the break-up process in T-junctions for low Ca numbers and for channels where the dispersed to continuous phase channel width ratio W_D/W_C varies from 0.25 to 1. Their results revealed that in the squeezing regime (low Ca numbers) the viscosity of the continuous phase does not affect the size of the droplets and that the droplet formation process is dominated by the pressure that builds up in the continuous phase. Steijn et al. (2010) who also developed a theoretical model to predict the size of plugs formed in the squeezing regime, studied how the shape of the channel can affect the α and β constants. Using a three-dimensional description of the droplet (2-D top view area and droplet perimeter) and the continuity equation (droplet volume equals the dispersed phase flowrate integrated over the time duration of plug formation), they determined the α and β parameters based entirely on the geometry of the channel and the fraction of the continuous phase that flows between the droplet and the channel walls.

Despite of their predictive ability in the squeezing regime, these models are not applicable in the transitional regimes, where the plug formation process is dominated by both the squeezing pressure and the viscous shear stress. The transition from squeezing to dripping regime occurs at a critical Capillary number Ca = 0.018 which has been calculated based on the continuous phase viscosity and velocity (Liu and Zhang, 2011). Glawdel et al. (2012b) and Christopher et al. (2008) used a detailed force balance to predict the filling volume and frequency of drops formed in a T-junction channel in the transition regime. Glawdel et al. (2012b) predicted the size of droplets formed in the squeezing to dripping transition regime by using a three-dimensional shape of the droplet throughout the formation process and a force balance, which estimates the penetration depth (b) of the droplet. Similar force balance was used by Christopher and co-workers who investigated plug formation in the squeezing to dripping transition regime over a wide range of viscosity ratios and T-shaped microchannels. In all cases, de-ionized water was used as the dispersed phase (μ_{Disp} = 1 mPas) whereas different viscosities (μ_{Cont} = 6-350 mPas) of oil were the continuous phase. They found that the viscosity

ratio (μ_{Disp}/μ_{Cont}) of the two phases plays an important role on the formation process only when it is close to 1 (viscosities of the two phases are close to each other). When there is a large viscosity difference, the formation mechanism and the droplet size are independent of the viscosity ratio.

In the dripping flow regime, the drop formation process is controlled by the balance of viscous shear and interfacial forces (Wang et al., 2009). The dripping flow regime occurs at higher Ca numbers ($0.018 < Ca < 0.1$) compared to the squeezing regime ($Ca < 0.01$) and the droplets generated with this mode are highly monodispersed (Xu et al., 2008). The same three stages of formation as in the squeezing regime (expansion, necking, pinch-off stage) are also identified in the dripping regime (Figure 2.6).

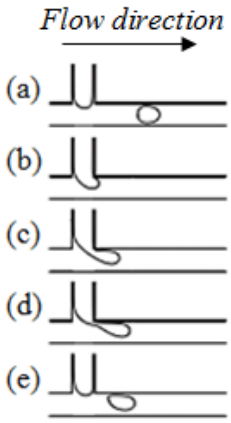

Figure 2.6: Typical droplet formation cycle in the dripping regime inside a T-junction generator: (a)-(b) expansion stage, (c)-(d) necking stage (e) pinch-off stage (Liu and Zhang, 2011).

During the expansion stage (Figure 2.6a-b), the interfacial tension force that acts on the forming drop initially dominates and controls the growth rate. As the droplet grows into the main channel, the shear stress inside the continuous phase increases and exceeds the interfacial tension force, thinning the neck (necking stage, Figure 2.6c-d). In addition, the pressure inside the continuous phase increases, because its flow is restricted by the droplet. The pressure that builds up in the continuous phase is less in the dripping regime than in the squeezing as the growing droplet has smaller size and blocks a smaller area inside the T-shaped inlet. The neck of the dispersed phase eventually breaks (pinch-off stage, Figure 2.6e) and a new droplet is formed.

In contrast to the squeezing regime, Tice et al. (2004) showed the importance of the continuous phase viscosity on droplet formation during the dripping regime. The experimental results indicated that as the continuous phase became more viscous and the Ca number

increased, greater resistance (viscous stress) was exerted on the growing droplet by the continuous phase flow leading to smaller droplets. Xu et al. (2008), who investigated droplet formation in the dripping regime inside a T-shaped inlet, developed a modified Ca number ($Ca_C \cdot \frac{wh}{wh-0.785D_D^2}$, where Ca_c is the continuous phase Capillary number ($\frac{\mu_C U_C}{\sigma}$), w is the channel width, h is the channel height, D_D is the droplet diameter) to take into account the influence of the growing droplet size on the continuous phase flowrate. By using this modified Ca, they predicted the droplet diameter, which was found to be almost independent of the flow rate of the dispersed phase.

Under the presence of flow, confined fluid threads break in the jetting regime at high Capillary numbers, Ca > 0.1. During this regime (Figure 2.7c), the dispersed phase forms a filament (jet) near the channel wall and parallel to the flow direction of the continuous phase. A droplet grows at the tip of this filament and detaches when the thread keeping the droplet attached to the bulk pinches-off (Steegmans et al., 2010). Droplet formation takes place downstream from the T-junction and two different types of jets can be observed depending on the continuous and dispersed phase flowrates. An increase in the flowrate of the continuous phase leads to a higher viscous shear of the continuous phase exerted on the dispersed phase resulting in a jet with small thickness. On the contrary, with increasing dispersed phase flowrate the jet thickness increases because of the increased inertia of the dispersed phase which overcomes the viscous shear from the continuous phase (Anna, 2016). The transition to jetting regime depends on the Capillary number of the continuous phase (viscous drag is the driving force) and the Weber number of the dispersed phase (inertia is dominant).

Figure 2.7 presents the three regimes as numerical simulation results for water/glycerol solution and silicone oil obtained by Li et al. (2012).

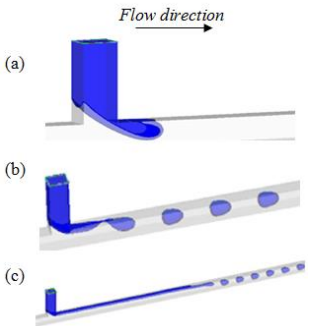

Figure 2.7: Regimes of drop/plug formation (a) squeezing (b) dripping and (c) jetting. Simulation results of water/ glycerol solutions and silicone oil in PDMS channel (Li et al., 2012).

A PDMS T-junction channel was used as the test section whereas silicone oil and aqueous glycerol solution were the continuous and dispersed phase respectively. The authors performed simulations for different superficial velocities of both phases to cover a large range of Capillary numbers and the corresponding regimes. It was found that as the Ca number increased, the flow pattern changed from droplets to parallel stream.

Plug and drop formation inside a flow-focusing channel

Flow – focusing is one of the most effective approaches for the production of uniform drop sizes at high frequency in microchannels. There are two types of flow-focusing geometry: the geometric flow-focusing and hydrodynamic focusing. In both methods, a liquid flows into the two outside channels (Fluid 1) and a second liquid flows into the main channel (Fluid 2), as can been seen in Figure 2.8. In the geometric flow-focusing case (Figure 2.8a) the two immiscible fluids are forced to flow through an orifice with size smaller than the main channel width (Anna et al., 2003; Garstecki et al., 2005) whereas in the hydrodynamic focusing case (Figure 2.8b) the droplet formation occurs in a cross-junction (Cubaud and Mason, 2008; Kovalchuk et al., 2018).

The mechanism of droplet formation in a flow – focusing inlet, is similar to that in a T-junction (Chen et al., 2015). Four different flow regimes can be identified within the flow-focusing devices namely *squeezing*, *dripping*, *jetting*, and *threading* (Kovalchuk et al., 2018).

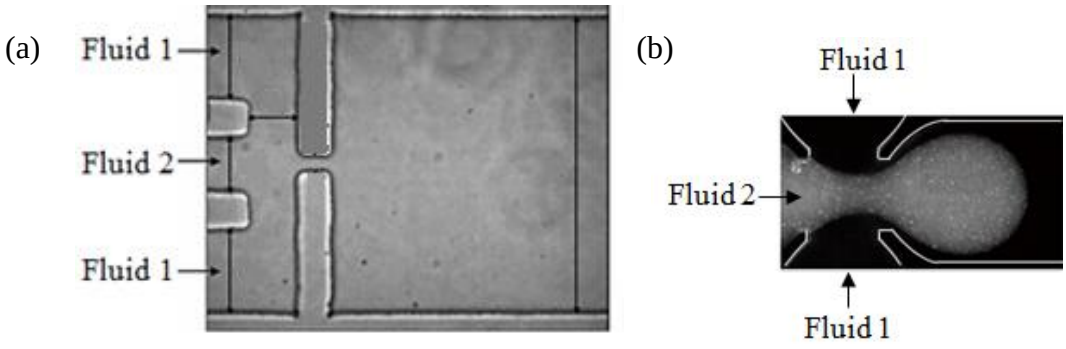

Figure 2.8: Different types of flow – focusing methods: (a) geometric flow-focusing (Anna et al., 2003) (b) hydrodynamic focusing.

In the squeezing regime (Figure 2.9a), that occurs at low Ca numbers (Ca < 0.01), the newly formed drop obstructs the junction restricting the continuous phase flow. Consequently, the pressure inside the continuous phase increases leading to the squeezing of the dispersed phase and to the detachment of the droplet (Chen and Ren, 2017).

An increase in the continuous phase flowrate results in a transition from squeezing to dripping regime where the drop formation process is controlled by the balance of viscous shear and interfacial tension forces (Anna, 2016). As can been seen in Figure 2.9b, the forming drops do not obstruct completely the flow of the continuous phase and their lengths (L) are smaller than the main channel width (W). High dispersed and continuous phase flowrates result in the jetting regime (Figure 2.9c).

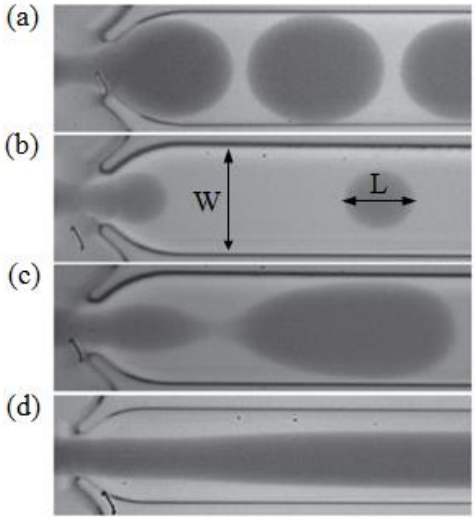

Figure 2.9: Flow regimes in flow-focusing devices (a) squeezing (b) dripping (c) jetting (d) threading (Kovalchuk et al., 2018).

In this regime, the dispersed phase is mainly driven by the continuous phase flow that pulls it downstream and the jet becomes destabilized. Drops are formed at the end of this unstable jet downstream of the flow-focusing inlet. A further increase in the flowrate (either of the continuous or the dispersed phase) results in the threading regime (Figure 2.9d) where a stable thread of the dispersed phase is produced and drops are no longer formed.

At high viscosity ratios of continuous to dispersed phase and moderate surfactant concentrations a fifth regime can be observed in the flow-focusing device namely *tip streaming* (see Figure 2.10).

Figure 2.10: Tip streaming in a flow-focusing geometry (Anna, 2016).

Under the presence of flow, surfactants are swept along the interface and towards the emerging tip. Surfactants that cannot desorb rapidly enough, accumulate at the tip region leading to a

dramatic reduction of the interfacial tension. A thin fluid thread is drawn from the nearly conical interface and breaks into small droplets.

Driven by the need to improve the prediction of drop size and frequency, the influence of various parameters on droplet formation in flow-focusing devices has been studied by several researchers, including the effect of viscosity (Fu et al., 2016), surfactant concertation (Carrier et al., 2015), inlet width and length (Gupta et al., 2014) and Ca number (Cubaud and Mason, 2008). Lee et al. (2009) investigated droplet formation in flow-focusing devices varying the flowrates and viscosities of fluids in order to gain insight into the physical mechanisms of droplet break-up. They concluded that droplet detachment in the squeezing and dripping regimes depends only on the upstream geometry and corresponding flow field and not on the geometry of the channel downstream of the flow-focusing inlet. On the contrary, the break-up of a filament and the production of droplets in the jetting regime depend mainly on the geometry and the flow field in the downstream channel. Recently, Chen et al. (2015) developed a physical model to describe the droplet formation in the squeezing regime, considering the 3D curved interface of the forming drop. Assuming that the mass of both the dispersed and the continuous phases is conserved and based on the pressure-driven squeezing mechanism proposed by Garstecki et al. (2005), they modelled the shape of the droplet during a formation cycle.

2.1.4 Plug characteristics: film thickness and plug velocity

Plug flow is one of the most frequently observed and favourable regimes in microchannels and has found several applications in fine chemical synthesis, food science, and encapsulation. A key feature of this type of flow is that each plug acts an individual sub-volume with well-defined interfacial area serving two principle transport mechanisms: 1) convection within the plugs and 2) interfacial diffusion between plugs and slugs (continuous phase). Internal circulation patterns that develop within the plugs and slugs reduce the thickness of interfacial boundary layer and consequently augment diffusive penetration. Mass transfer depends on the plug geometry and circulation patterns, which vary with the physical properties of the liquids as well as with operating parameters and the channel dimensions and geometry (Kashid et al., 2011).

Because of the importance of the plug flow regime, plug formation has attracted significant attention during the last decade. Several experimental works have been reported in the literature regarding to the liquid-liquid plug formation systems. Studies on liquid-liquid droplet

formation and plug flow are presented in Table 2.3. During plug flow, a film of the continuous phase often surrounds the plugs and separates them from the channel wall, as can be seen in Figure 2.11. The significance of this film is that the whole plug surface area can take part in mass transfer between the two phases (Kashid et al., 2005). However, the thickness of the film, δ, is not uniform along the entire length of the plug.

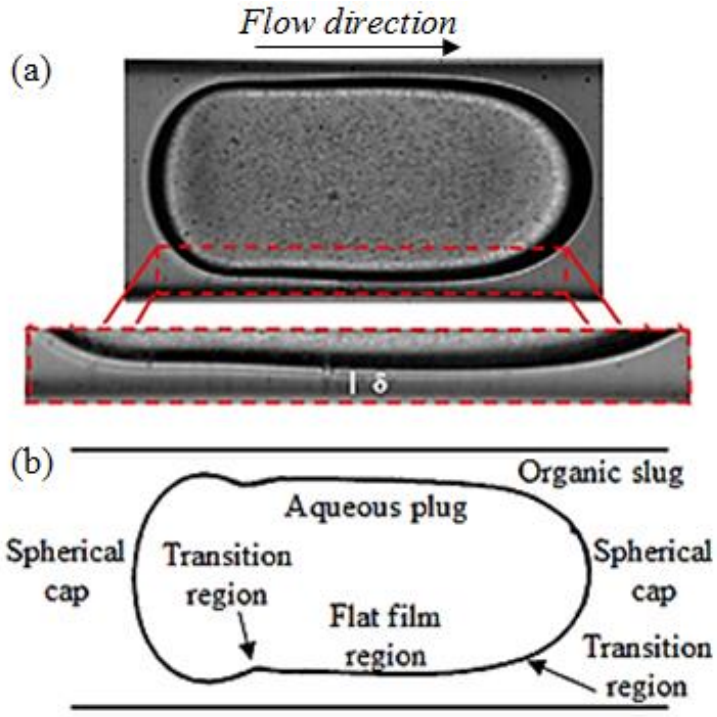

Figure 2.11: (a) Continuous phase film surrounding the plug (b) Schematic illustration of the different regions of film along the bubble (Bretherton, 1961).

The plug profile can be divided into three different regions (Figure 2.11b) according to Bretherton (1961), who investigated the motion of bubbles in tubes. The front and rear parts of the plug are spherical caps with different curvature defined by the balance between the pressure difference across the interface and the interfacial tension. These caps join in the region of a uniform film thickness. It was found that at the point where the back cap joins the main body of the plug, there is a slight dip of the interface profile and consequently an increase in the film thickness.

While there are several studies for film thickness in gas-liquid two-phase flows, limited literature regarding liquid-liquid systems is available. Most of the models in the literature (Table 2.4) show the dependence of the film thickness on the dimensionless Capillary number which is defined below as a function of continuous phase viscosity, μ_C (kg/ms), mixture velocity, U_{MIX} (m/s), and interfacial tension between the phases, σ (kg/s^2):

$$Ca = \frac{\mu_C \cdot U_{MIX}}{\sigma} \quad \text{(Equation 2.4)}$$

$$u_{MIX} = \frac{Q_D + Q_C}{A} \quad \text{(Equation 2.5)}$$

where A denotes the cross section of the channel and Q_D and Q_C represent respectively the flow rate of the dispersed and the continuous phases.

Table 2.3: Literature review on liquid-liquid plug flow system

Author	Conditions	Study
Garstecki et al. (2006)	• PDMS T - shaped microchannel • Water/oil • Q_D = 0.004 – 0.14 µL/s • Q_C = 0.003 – 0.27 µL/ s	Experimental work on flow regimes, pressure drop and plug size
Christopher et al. (2008)	• PDMS T-shaped microchannel • Water / silicone oil • $Q_D = Q_C$ = 4 – 2000 µl/h	Experimental work on droplet formation
Funfschilling et al. (2009)	• Glass flow-focusing microchannel • Silicone oil/Aqueous SDS solution • Q_D = 0.18 µL/ s • Q_C = 1.39 µL/ s	Experimental study on flow field during droplet formation
Li et al. (2012)	• PDMS T-shaped microchannel • Aqueous glycerol solutions /oil • Q_D = 8.0 – 20.0 µL/h • Q_C = 23.9 – 100.0 µL/h	Numerical/analytical droplet formation
Eain et al. (2013)	• Teflon T-junction tubes/segmenters • Water / oil (Pd5, FC40, AR20) • Ca = 0.002 – 0.119	Experimental study on film thickness during plug flow
Tsaoulidis and Angeli (2016)	• Teflon T-junction mixer • Aqueous nitric acid +ionic liquid • Q_D = 3.5 – 227.8 cm^3/h • Q_C = 3.5 – 112.2 cm^3/h	Experimental work on mass transfer during plug flow
Chen and Ren (2017)	• PDMS flow-focusing microchannel • Aqueous glycerol solutions /oil • Q_D = 1.62 µL/min • Q_C = 4 µL/min	Experimental study on droplet formation

Table 2.4: Film thickness correlations from the literature.

Author	Correlation	Parameters
Bretherton (1961)	$\frac{\delta}{R_C} = 1.34\ Ca^{2/3}$	$10^{-4} \leq Ca \leq 10^{-2}$ Gas-liquid flow
Irandoust and Anderson (1989)	$\frac{\delta}{R_C} = 0.36[1 - \exp(-3.08\ Ca^{0.54})]$	$9.5\times10^{-4}<Ca< 1.9$ Gas-liquid flow
Aussillous and Quere (2000)	$\frac{\delta}{R_C} = \frac{1.34\ Ca^{2/3}}{1 + 3.35\ Ca^{2/3}}$	$10^{-3} \leq Ca \leq 1.4$ Gas-liquid flow
Dore et al. (2012)	$\frac{\delta}{R_C} = 0.30[1 - \exp(-6.90\ Ca^{0.54})]$	$0.007<Ca<0.159$ Liquid-liquid flow
Eain et al. (2013)	$\frac{\delta}{R_C} = 0.35 Ca^{0.354} We^{0.097}$	$0.002<Ca< 0.119$ Liquid-liquid flow

*R_C is the inner radius of the channel

As the velocity, and consequently the Ca number increases, the film thickness is also increased. The rate of the film increase follows an asymptotic trend until a threshold Ca number is reached, due to the tube confinement. The Dore et al. (2012) model, presented in Table 2.4 is a modification of the Irandoust and Anderson (1989) model whereas the Eain et al. (2013) model uses two non-dimensional groups, Capillary and Weber number, where both viscous and inertia effects are accounted for. The dimensionless Weber number, which relates the inertial and the surface tension forces, is defined by Eain et al. (2013) as:

$$We = \frac{\rho \cdot U_P^2 \cdot D}{\sigma} \qquad \text{(Equation 2.6)}$$

where the plug velocity, U_P, is used for the calculation of both the Ca and We numbers instead of the mixture velocity. According to Eain et al. (2013), the film thickness depends on a number of parameters, including the relative velocity between the phases. This velocity, at low continuous phase flow rate, is assumed to be the mixture velocity whereas as the continuous phase flow rate increases, the film thickness increases and the plug velocity increases as well. As a result, a Capillary number based on plug velocity provides a better representation of the forces influencing the film thickness and it can be defined as follows.

$$Ca = \frac{\mu_C \cdot U_P}{\sigma}$$ (Equation 2.7)

Another interesting characteristic of the plug flow is the recirculation patterns in the plugs and slugs. When the plugs move through the capillary, depending on the physical properties and operating conditions, internal circulations (Figure 2.12) arise because of the shear between the channel wall and the plug. Dore et al. (2012) observed that there are different recirculation regimes depending on the plug length.

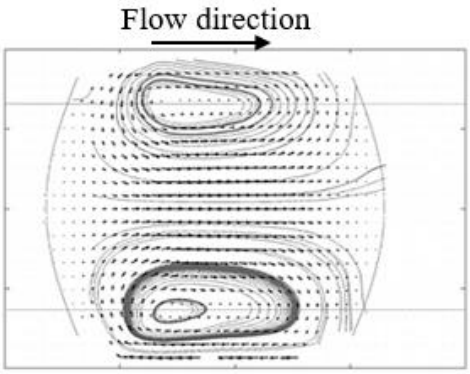

Figure 2.12: Schematic representation of recirculation pattern inside plug (Dore et al., 2012).

As the length increases with increasing mixture velocity a clear recirculation pattern forms, which consists of two distinct vortices, counter rotating and symmetrical about the channel axis. On the contrary, the two vortex cores move towards the rear of the plug when the plug length decreases. The recirculation inside the plugs promotes mixing which can be quantified via the circulation time, T_L, defined as the time for the liquid to move from one end of the plug to the other (Thulasidas et al., 1997).

The circulation time can be normalized with the plug travel time, T_P, which is defined as the time needed by the plug to travel a distance of its own length, and is given by $T_P = L_P / u_P$ where L_P is the plug length and u_P the plug velocity. The ratio of the two characteristic times is the non – dimensional circulation time, τ_C:

$$\tau_{cir} \equiv \frac{T_L}{T_P} = \frac{T_L U_P}{L_P}$$ (Equation 2.8)

The evaluation of τ requires the knowledge of the velocity field and of the circulation pattern within the plug. Assuming that the plug length is long enough for a fully developed Poiseuille profile to form in the middle area of the plug and neglecting the end effects close to the interface, the dimensionless circulation time is defined by Thulasidas et al. (1997) as follows:

$$\tau_{cir} = \frac{U_P r_o^2}{2\int_0^{r_o} V(R)\, R_C\, dR} \qquad \text{(Equation 2.9)}$$

where r_o is the location of the stagnation surface and V(R) is the Poiseuille velocity profile in a moving frame within the plug in a circular channel with radius R_C. Considering a xy observation plane at the centre of a moving plug, Dore et al. (2012) used a two-dimensional definition for the dimensionless circulation time:

$$\tau_{cir} = \frac{U_P y_o}{\Delta y \sum_{i=1}^{i=N} v_i} \qquad \text{(Equation 2.10)}$$

where y_o is the location of the stagnation point projected onto the observation plane.

2.2 Surfactants

Several products (for example mayonnaise, milk, paint and shampoo) are emulsion-based systems that are produced using high shear devices under the presence of surfactants. Surfactants are surface-active agents that are added to either the continuous or the dispersed phase to lower the interfacial tension so that smaller droplets can be formed and to enhance drop stability during the droplet formation process. They stabilize the droplet through the formation of an interfacial layer that provides steric and/or electrostatic repulsions preventing droplets from coalescing (Chen et al., 2015; Muijlwijk et al., 2015). Surfactants are also beneficial in maintaining desired wetting conditions at the channel walls and in encapsulating cell applications (Anna, 2016). Due to these reasons, surfactants are used extensively in multiphase applications in microfluidic devices. They add, however, complexity in the system since they can induce interfacial tension gradients (Marangoni effects) and alter the dynamics of droplet breakup (Wang et al., 2009).

Therefore, choosing the appropriate surfactant is crucial in the formation of droplets. A typical surfactant molecule consists of a hydrophilic head and a hydrophobic tail where each group shows affinity for a different immiscible phase (i.e. water/oil, water/air). Due to this characteristic, surfactants accumulate at the interface reducing the interfacial tension (Baret et al., 2009). Depending on the surfactant adsorption rate and interface expansion rate, the interfacial tension changes dynamically during the droplet formation process within the range bounded by the value at pure liquids and the system with the added surfactants in equilibrium (Glawdel and Ren, 2012). When the surfactant adsorption last longer than the droplet

formation, the dynamic interfacial tension may be equal to the interfacial tension of the pure system (without surfactants). On the contrary, when the adsorption time is faster than the formation rate, the dynamic interfacial tension can vary (within the above-mentioned range). Baret et al. (2009) who investigated the adsorption of surfactants to the interface using fluorescently labelled surfactants observed that the interface is nearly bare after the droplet is formed and the coverage increases with time as the droplet travels in the microchannel. Kovalchuk et al. (2016) studied experimentally how the kinetics of thinning of liquid bridges during the breakage of surfactant-laden drops (using C_{10}TAB, C_{12}TAB, C_{16}TAB, Triton X-100) are affected by both the surfactant activity and concentration. They found that the less active surfactants (with high critical micelle concentration, CMC) behave like pure liquids with constant interfacial tension value. When more active surfactants were used (low CMC values), the kinetics of the neck thinning close to the pinch-off were found to depend mainly on the dynamics of adsorption of the surfactant to the drop neck. Riaud et al. (2018) who studied both numerically and experimentally the dynamics of surfactants during drop formation in a T-junction, found that higher concentration of surfactant prevents recirculation inside the dispersed phase, makes the interface more rigid and results in a more uniform velocity field compared to the surfactant-free case.

The surfactant adsorption to the interface depends on the characteristics of surfactant (concentration, diffusion coefficient, micelle kinetics) and the mass transfer process (convection, diffusion) which are found to have a significant effect on interfacial tension and droplet formation. One of the most notable works in the literature about surfactant adsorption belongs to Glawdel and Ren (2012) who studied the formation of water/glycerol droplet in an organic continuous phase in the presence of surfactants. They developed a theoretical model to predict the interfacial tension, σ, based on the surfactant properties, flow conditions and microchannel design:

$$\Delta\sigma(t) = \frac{vRT\Gamma_{CMC}^2}{CMC}\sqrt{\frac{3\pi}{4D_{EFF}}}\sqrt{\frac{f_3^2\, t}{(f_3 t)^2+3f_3 t+3}} \qquad \text{(Equation 2.11)}$$

where v = 1 for non-ionic surfactants and v = 2 for ionic surfactants, R is the gas constant, T is the absolute temperature, CMC is the critical micelle concentration, Γ_{CMC} is the surface coverage at CMC, D_{EFF} is the effective diffusion coefficient, t is the formation time and $f_3 = \frac{2Q_D}{W_D h^2}\left(1 + \left(\frac{h}{W_D}\right)^{1/2}\right)$ (Q_D is the dispersed phase flowrate, W_D is the width of the channel for the dispersed phase and h is the channel height). The above model shows that the deviation of

interfacial tension from the equilibrium value decreases with an increase of the formation time, surfactant diffusion coefficient and CMC value. On the contrary, the deviation of σ from the equilibrium value increases with the square of Γ_{CMC}. Taking into account that the Γ_{CMC} is of the same order of magnitude for most surfactants whereas CMC can differ by several orders of magnitude (Kovalchuk et al., 2018), it can be concluded that CMC is the most important property determining the effect of surfactants on droplet formation.

2.3 Non-Newtonian fluids

Many industrially relevant fluids exhibit complex rheological behaviour and non-Newtonian properties (Chiarello et al., 2015). Non-Newtonian flows in microchannels find applications in the contamination of soils and underlying aquifers by non-aqueous phase liquids (NAPLs) (e.g. crude oil, asphalt, suspensions of engine oils etc.), in enhanced oil recovery operations involving the injection of non-Newtonian fluids of controlled rheology (e.g. polymer solutions, foam solutions, emulsions, etc.), in catalytic polymerisation reactions and food processing (Tsakiroglou, 2004).

Newtonian are the fluids where there is a linear relationship between the applied shear stress, τ (Pa) and the shear rate, $\dot{\gamma}$ (1/s). Mathematically, this relationship is known as Newton's Law of Viscosity:

$$\tau = \frac{F}{A} = \mu\dot{\gamma} \qquad \text{(Equation 2.12)}$$

where μ is the viscosity (mPa-s) that is independent of the strain rate. Some examples of Newtonian fluids include water and organic solvents. For these fluids, viscosity is only dependent on temperature. The viscosity of Newtonian fluids will remain constant and independent of their flow velocity.

When fluids exhibit a deviation from Equation 2.12, they are called non-Newtonian. The apparent viscosity, defined as $\tau / \dot{\gamma}$, is not constant and is a function of shear stress or shear rate. The non-Newtonian behaviour can be divided into three main categories:

- Time-independent fluids: the value of $\dot{\gamma}$ at a point within the fluid is determined only by the current value of τ at that point;
- Time-dependent fluids: the relation between τ and $\dot{\gamma}$ shows further dependence on the duration of shearing and kinematic history;

- Visco-elastic fluids: a blend of viscous fluid behaviour and of elastic solid-like behaviour.

It is worth mentioning that this classification is quite general as most of the materials often display a combination of two or even all these types of behaviour under appropriate conditions. Characteristic examples are some polymer melts that exhibit time-independent and visco-elastic behaviour at the same time. Those fluids that exhibit a combination of properties from more than one of the above groups are described as complex fluids, though this term may be used for non-Newtonian fluids in general (Astarita and Marrucci, 1974).

2.3.1 Time-independent fluid

The majority of studies on liquid-liquid flows in microchannels have concentrated on Newtonian fluids (Chen and Ren, 2017; Jovanovic et al., 2011; Kashid and Agar, 2007; Salim et al., 2008; Su et al., 2010) while few works have focused on flows with time-independent non-Newtonian liquids (Arratia et al., 2008; Husny and Cooper-White, 2006; Nooranidoost et al., 2016). In the literature, a number of models have been suggested to describe the rheological behaviour of non-Newtonian fluids. Some common models are presented in Table 2.5.

Table 2.5: Examples of non-Newtonian rheological models

Model	Equation
Power-Law	$\mu = K\,\dot{\gamma}^{n-1}$
Ellis	$\mu = \frac{\mu_0}{1 + (\frac{\tau}{\tau_{1/2}})^{a-1}}$
Carreau	$\mu = \mu_\infty + \frac{\mu_0 - \mu_\infty}{[1 + (\dot{\gamma} t_C)^2]^{\frac{1-n}{2}}}$
Herschel-Bulkley Maxwell	$\tau = \tau_O + C\,\dot{\gamma}^n (\tau > \tau_O)$

where μ viscosity, K consistency index, $\dot{\gamma}$ shear rate, n flow behaviour index, μ_0 zero-shear viscosity, τ shear stress, $\tau_{1/2}$stress when $\mu = \mu_0/2$, a rheological parameter, μ_∞ infinite-shear viscosity, t_C characteristic time of flow system, τ_O yield-stress.

Husny and Cooper-White (2006) experimentally investigated the formation of drops in a T-junction microfluidic device using non-Newtonian aqueous solutions of polyethylene oxide

(PEO) as the dispersed phase and organic solutions as the continuous phase. Their results showed that by increasing the continuous phase viscosity the drop size decreased whereas the presence of PEO elasticity had negligible effect on the size of the drop produced. Numerical simulations of droplet formation in non-Newtonian fluids in T-junction channels were made by Sang et al. (2009) for several power-law fluids with different consistency values (K) and power-law exponents (n). They observed that when K increased, the droplet diameter decreased and the dispersed phase was pulled downstream to the main channel forming a longer segment before the droplet detachment. Based on a force balance, Sang et al. (2009) introduced an analytical model to predict the droplet size. Fu et al. (2011) studied N_2 bubble formation in different concentrations of shear-thinning polyacrylamide (PAAm) solutions in a T-junction microchannel using a high-speed camera. The experimental results showed that as the concertation of the PAAm solutions increased, the bubble size decreased whereas the bubble edge curvature increased. Chiarello et al. (2017) investigated the formation of oil droplets in shear-thinning xanthan gum aqueous solutions and introduced an effective Capillary number that took into account the shear-thinning rheology. They observed that the droplet size increased with the ratio of the dispersed to continuous phase flowrate whereas the droplets generated in xanthan gum solutions were more elongated compared to the Newtonian ones.

2.4 Particle image velocimetry (PIV)

Over the last decade the interest in complex flows e.g. non-Newtonian liquids, added surfactants in small channels is constantly growing. However, the flow behaviour of these systems is complex, including diffusion through thin fluid layers and recirculation patterns within phases. It is important to have appropriate experimental approaches to study the liquid-liquid flows in small channels when complex fluids are involved (Sathe et al., 2010; Shinohara et al., 2004).

Particle image velocimetry (PIV) refers to a class of methods used in experimental fluid mechanics to determine instantaneous fields of the velocity vector by measuring the displacement of small particles that accurately follow the motion of the fluid (Adrian and Westerweel, 2011). Over the last 15 years, there are many studies in the literature referring to the use of PIV in large-scale applications. Broder and Sommerfeld (2002) measured the velocity field of both gas and liquid phases in a laboratory scale, bubble column operated at a relatively high void fraction. Wissen et al. (2005) have measured the flow pattern of a

condensation jet in a water vessel using PIV whereas Deshmukh et al. (2008) carried out PIV measurements in the annular region of centrifugal extractors. Ganguli et al. (2010) investigated the natural convection phenomenon in the presence of boiling in cylindrical enclosures heated by a centrally placed pipe using PIV technique.

The first description of a modern micro-PIV was given by Santiago et al. (1998) and through this technique multipoint information of the velocity inside the liquids in small channels can be extracted with high accuracy and spatial resolution and in a non-intrusive manner. In literature, there are four main aspects that differentiate micro-Particle Image Velocimetry (μ-PIV or micro-PIV) from traditional PIV. First, Brownian motion effects on tracer particles with diameters smaller than 1 μm can play a role adding uncertainty in the final result. Secondly, instead of using a laser light sheet the flow field is volume illuminated resulting in background noise from out-of-focus particles when the concentration of the seed particles is high. Thirdly, the use of tracer particles smaller than the laser light wavelength invalidates the employment of light scattering techniques. Finally, fluorescent particles are commonly used in microchannels to overcame reflections of the surrounding channel walls and enhance the signal of the tracer particles (Silva et al., 2008).

The micro-particle image velocimetry technique has been widely used to investigate micro-scale fluidic transport and mixing on liquid-liquid Newtonian flows (Carrier et al., 2015; Dore et al., 2012; Kashid et al., 2005; Sathe et al., 2010; Silva et al., 2008). In these studies, some of them presented in Table 2.6, μ-PIV has been used to visualize the internal recirculation in aqueous slugs or plugs during aqueous/oil two-phase flows. Shinohara et al. (2004) investigated the transient fluidic phenomena in a counter-cross microfluidic device, in which two channels were connected to one channel in a X configuration. The velocity profiles of the counter-current flow of water and butyl acetate were studied using high-speed μ-PIV. Steijn et al. (2007) studied the formation of bubbles in a T-junction microchannel using a micro-PIV system and constructed three-dimensional velocity fields of the continuous phase by taking measurements at different channel depths. Funfschilling et al. (2009) used μ-PIV to study the droplet formation mechanism and to measure the velocity fields in aqueous SDS solutions around a forming droplet (organic phase) in a flow focusing microchannel. The instantaneous flow fields in the continuous phase revealed that the increasing pressure that builds up inside the continuous phase, and not the shear, is the dominant mechanism that initiates the droplet detachment. Meyer et al. (2014) used the micro-PIV technique to study the liquid film between Taylor bubbles and the channel walls in a square shaped channel. They found that a recirculation flow pattern forms inside the liquid film. Kim et al., studied the thermal effects

on liquid – vapour interfaces during thermal-buoyant capillary flows inside microtubes (680 - 1560 μm) using a high-resolution micro-PIV technique. The PIV data revealed complex vortex flow structures and Marangoni effects due to temperature gradients creating by evaporation effects close to the vapour-liquid interface. Kim and co-workers (2019) found that this arise of Marangoni gradients resulted in weak recirculation patterns inside the buoyancy-driven flows.

Table 2.6: Liquid-liquid micro-systems studied with PIV system.

Author	Conditions	Study
Dore et al. (2012)	• Glass T-junction channel • Water/ionic liquid • Double pulsed micro-PIV	Experimental work on plug velocity and circulation patterns
Oishi et al. (2011)	• PDMS T-shaped microchannel • Aqueous glycerol solutions/oil • Confocal micro-PIV	Experimental study on velocity during droplet flow
King et al. (2007)	• FEP Teflon tubing • Water/FC-40 • Double pulsed micro-PIV	Experimental study on plugs velocity and circulation time
Shinohara et al. (2004)	• Glass counter-cross microchannel • Water/butyl acetate • High-speed micro-PIV	Experimental work on counter-current flow

In two-phase μ-PIV application, as the above mentioned systems, one of the phases is seeded with fluorescent tracers and the velocity profile of this phase only is obtained. Attempts to measure the velocity fields in both phases simultaneously have resulted in the *two-colour micro-PIV systems*. In this case, two different wavelengths are generated and two types of tracer particles are dispersed into each phase separately with different fluorescent characteristics i.e. they absorb at different wavelengths and emit fluorescent light at different Stokes shifted wavelengths (Adrian and Westerweel, 2011). In this work, the same laser unit was used to generate simultaneously both wavelengths.

2.5 Overview

The hydrodynamic behaviour of two-phase flows in small channels has been extensively studied by many researchers. However, most of the studies involved plug or drop formation in

Newtonian fluids with low viscosities although fluids with complex behaviour and non-Newtonian rheology are widespread in industrial applications, such as in enhanced oil recovery and food processing. The understanding of liquid-liquid flows when one of the liquids has complex rheology is still limited compared to flows of Newtonian fluids. In addition, the knowledge of the hydrodynamics inside and outside the droplet during formation is incomplete when surface active agents are present.

Based on the above, in the following Chapters, liquid-liquid formation and flow in small channels are studied for liquids with complex rheology and in the presence of surfactants. A novel two-colour micro-Particle Image Velocimetry technique is developed and used to obtain velocity profiles in both phases. Flow patterns and hydrodynamic characteristics such as plug (or drop) length, plug shape, neck radius and film thickness have been investigated in channels with different inlet geometries. A mechanistic model was also developed, based on the PIV data, to describe the evolution of the forces acting on the plug during the formation process.

3. Chapter: Materials and experimental methods

The scope of this chapter is to provide a detailed description of the experimental techniques and equipment used in this thesis. The properties of fluids and characterisation methods are also discussed as well as the methodology for carrying out the experiments.

3.1 Materials

3.1.1 Characterization of shear-thinning fluids

For the investigation of non-Newtonian fluids in small channels, two aqueous glycerol solutions containing xanthan gum at different concentrations (from Sigma-Aldrich) were used. Xanthan gum is a polysaccharide bio-polymer with high molecular weight and great industrial importance with applications in the food, pharmaceutical and oil industries (Ghannam et al., 2014). The examined aqueous solutions with xanthan gum exhibit shear-thinning non-Newtonian behaviour with the shear viscosity decreasing with shear rate (Figure 3.1). Experiments were also carried out with the corresponding Newtonian aqueous solution (N, without xanthan gum) for reference and comparison. Although the xanthan gum molecule is quite stiff, elastic effects can be noticed in concentrated solutions, which are due to network interactions. However, in dilute and semi-dilute solutions the dominant behaviour is that of viscous shear-thinning.

As for the Newtonian, organic phase, a low viscosity, 0.0046 Pa s, silicone oil was used. In order to match the refractive index between the aqueous (refractive index of pure water, n_D^{20} = 1.33) and the organic phases (n_D^{20} = 1.39), as required for the PIV measurements, glycerol was added in the aqueous phase to eliminate any light refractions and optical distortions. It was found that a mixture of 48% w/w water and 52% w/w glycerol matches the oil refractive index. The properties, viscosity and interfacial tension of the fluids have been measured using corresponding techniques and are presented in the Table 3.1. With these fluids, the aqueous solutions were the continuous phase and the silicone oil formed the dispersed plugs.

The Advanced Rheometric Expansion System (ARES, TA Instruments®), which subjects a sample to either dynamic or steady shear strain, is used to study the rheological behaviour of the non-Newtonian solutions. All measurements were carried out at 21 ^oC. A water bath was used to control the temperature in the rheometer and the Couette geometry was used with bob

diameter 16.5 mm and cup size 17 mm. Figure 3.1 shows the viscosity profile as a function of the shear rate for two different concentrations of xanthan gum. N1 and N2 represent the non-Newtonian solutions with 1000 ppm and 2000 ppm xanthan gum respectively.

Table 3.1: Properties of the working fluids (T = 21°C).

Fluid system			μ, Pa s		σ_{eq}^{*}, (mN/m)	ρ, (kg/m^3)	$\varphi_{N/O}$, deg
			K	n			
Continuous phase	N2	Aqueous solution +2000 ppm	0.85	0.36	30.70	1144	54
	N1	Aqueous solution + 1000 ppm	0.55	0.39	31.40	1143	50
	N	Aqueous glycerol solution	0.007		29.00	1142	61
Dispersed phase	O	Silicone oil	0.0046		-	920	-

*equilibrium interfacial tension

As can be seen, the shear-thinning behaviour, is pronounced in both cases. It is noted that the viscosity of the Newtonian solution (0.007 Pa s) is always lower than that of the non-Newtonian ones even at high shear rate values (above 1000 s^{-1} where μ_{N1} = 0.014 Pa s and μ_{N2} = 0.016 Pa s).

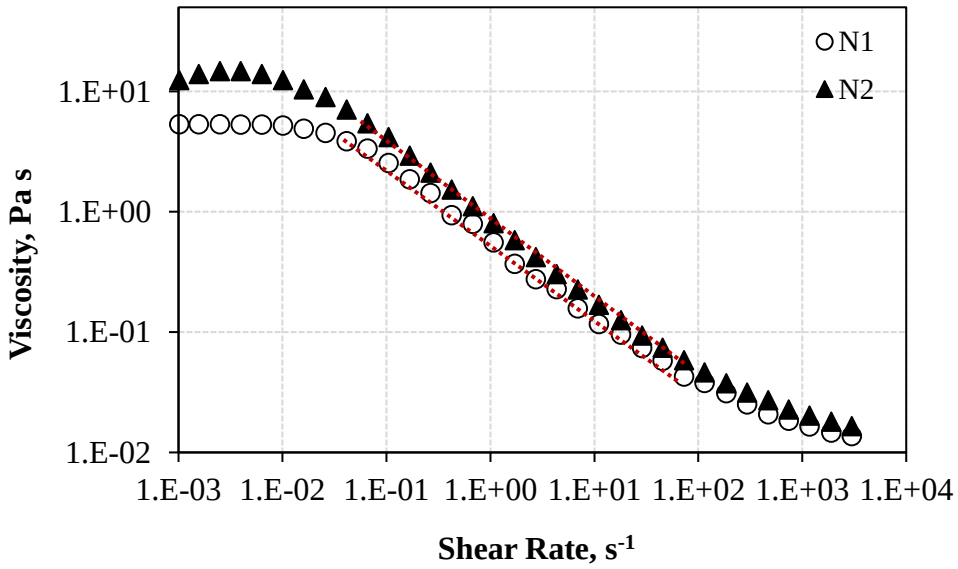

Figure 3.1: Viscosity vs. shear rate curve of the non-Newtonian fluids used. Dashed lines represent the power-law fitting of the viscosity curves. N1 and N2 are the non-Newtonian 1000 ppm and 2000 ppm solutions respectively.

The produced viscosity data are fitted with the power-law model (Harris, 1977) $\mu = K \cdot \dot{\gamma}^{n-1}$, with n < 1 for shear-thinning fluids. Here $\dot{\gamma}$ is the shear rate; K is the consistency index; n is the flow behaviour index. In the case of plug flow with non-Newtonian solutions as the continuous phase, a modified Capillary number needs to be defined. (Chiarello et al., 2017; Fu et al., 2016). In order to define a representative Ca, the calculation of the shear rate is crucial. In total, three different definitions of mean shear rate were tested based on geometric average $\left(\dot{\gamma} = \frac{U_S}{D}\right)$, Newtonian parabolic profile $\left(\dot{\gamma} = \frac{3U_S}{D}\right)$ and power-law profile $\left(\dot{\gamma} = \frac{2 \cdot U_S \cdot (1+2n)}{D(1+n)}\right)$ (Lindner et al., 2000). All these definitions are using the mean continuous phase velocity, U_S and indicate how strong or weak the shear-thinning behaviour is. For weak shear-thinning solutions (1 > n > 0.65), the continuous phase approaches Newtonian behaviour and the velocity profile can be assumed as quasi parabolic so the mean shear rate derived from it, is equal to $\left(\dot{\gamma} = \frac{3U_S}{D}\right)$. For stronger shear-thinning behaviour (n < 0.65) as it is in the current study, this assumption fails and the third definition ($\dot{\gamma} = \frac{2U_S(1+2n)}{D(1+n)}$) becomes necessary. Thus, the Capillary number for non-Newtonian solutions is calculated as follows (based on Equation 2.7):

$$Ca = \frac{\mu_C \cdot U_P}{\sigma} \qquad \text{(Equation 3.1)}$$

where $\mu_C = K \cdot (\dot{\gamma})^{n-1}$ is the continuous phase viscosity, U_P is the plug velocity, σ is the interfacial tension and K is the consistency index. The average shear rate across the channel diameter, D, is calculated as $\dot{\gamma} = \frac{2 \cdot U_S \cdot (1+2n)}{D(1+n)}$ where U_S represents the mean continuous phase velocity and n the flow behaviour index. This definition assumes a power law velocity profile in the channel. In the case of $n \rightarrow 1$, then $\mu_C' \rightarrow$ constant across all shear rates and Equation 3.1 defines the Capillary number for Newtonian fluids.

The shear-thinning fluids are considered to have constant interfacial tension value, σ, during plug formation, which is measured with the Du Noüy ring method (K100 KRUSS GmbH®). The maximum force, F_{MAX}, on the wetted length , L_W, acting on the ring as it moves from one phase to another (lamella) gives the interfacial tension between the liquids. The maximum force is determined with the help of an electronic force sensor and can be obtained repeatedly without tearing the two-phase boundary. The equilibrium interfacial tension then is found as follows:

$$\sigma = \frac{F_{MAX}}{L_W \cdot \cos\theta} \quad \text{(Equation 3.2)}$$

where θ is the contact angle between the ring and the liquids (θ = 0° as the ring is platinum made).

Finally, the contact angles of the liquids with substrates made from similar materials as the channel walls are measured using the Kruss DSA 100 system. Liquid-liquid-solid contact angles are obtained. The substrate is immersed in water/glycerol solution and a drop of oil is put on top of it to replicate the flow inside the channel. Depending on the value of θ° (Figure 21) the wettability of the surface could be characterised as, spreading (θ=0°); good wetting (θ<90°); incomplete wetting (θ=90°); poor wetting (θ>90°), and no wetting (θ=180°) for the oil phase. The contact angle of a liquid drop is described by the mechanical equilibrium of the drop under the action of three interfacial tension forces, Young equation:

$$\sigma_{F1/F2} \cos\theta = \sigma_{s/F2} - \sigma_{s/F1} \quad \text{(Equation 3.3)}$$

where $\sigma_{F1/F2}$, $\sigma_{S/F2}$, $\sigma_{S/F1}$ represent the Fluid 1-Fluid 2, surface-Fluid 2 and surface-Fluid 1 interfacial tensions, respectively. From Table 3.1, it can be seen that the contact angle of all aqueous solutions with the silicone oil is less than 90° indicating that wetting of the surface is favourable and the fluid is spreading over the channel surface.

3.1.2 Characterization of surfactant-laden solutions

Two ionic surfactants, dodecyltrimethylammonium bromide (C_{12}TAB), (Across organics, 99 %, M_W = 308 g/mol) and hexadecyltrimethylammonium bromide (C_{16}TAB), (Sigma, BioXtra, ≥ 99 %, M_W = 364 g/mol) were tested in order to investigate the effect of interfacial tension on the droplet formation process. The low viscosity, 0.0046 Pa s, silicone oil (Sigma-Aldrich) was used again as the organic phase whereas the water/glycerol solution (48% w/w water and 52% w/w glycerol) was the aqueous phase. The surfactants were dissolved in the aqueous phase and one concentration of each surfactant was used: 50 mM for C_{12}TAB and 5 mM for C_{16}TAB. Under these physical properties of the fluids, the silicone oil was now the continuous phase and the water/glycerol solution was the dispersed phase. The properties of the surfactant solutions are presented in the Table 3.2.

The interfacial tension isotherms for C_{12}TAB and C_{16}TAB surfactant solutions are presented in Figure 3.2. From the interfacial tension isotherms for C_{12}TAB and C_{16}TAB surfactant solutions the CMC values can be found. These are the surfactant concentrations above which

there is no: further decrease in the interfacial tension and they are equal to ~ 20 mM and ~2 mM for C_{12}TAB and C_{16}TAB respectively.

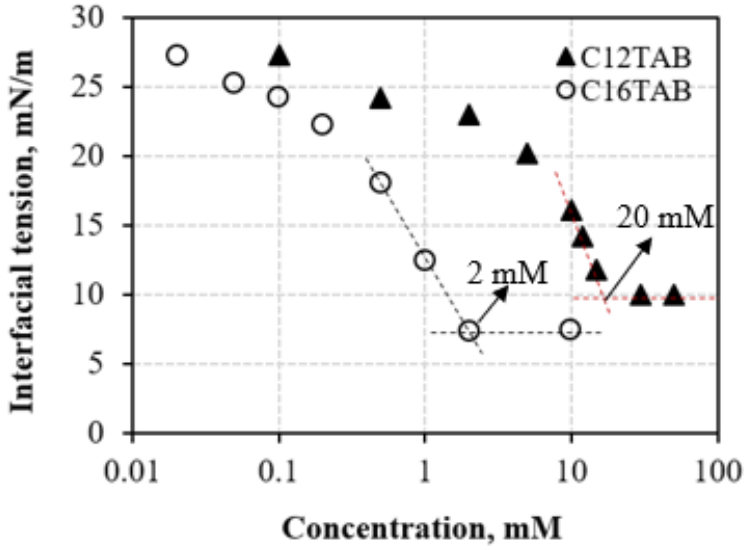

Figure 3.2: Equilibrium interfacial tension against concentration for the surfactants C_{12}TAB and C_{16}TAB.

Concentrations above CMC were chosen to ensure that an adequate surfactant concentration will be adsorbed on any newly formed interface (Funfschilling et al., 2009). In addition, in a previous work with the same surfactants (Kovalchuk et al., 2018) it was found that low surfactant concentrations did not affect the flow pattern map significantly.

Table 3.2: Properties of the test fluids (T = 21°C).

Fluid system			**μ, Pa s**	**σ_{eq}^{*}, (mN/m)**	**ρ, (kg/m^3)**
Dispersed phase	Surfactant-free	Aqueous glycerol solution	0.007	29	1142
	C_{12}TAB	Aqueous glycerol solution + 50 mM	0.007	10	1142
	C_{16}TAB	Aqueous glycerol solution + 5 mM	0.007	7.3	1142
Continuous phase	O	Silicone oil	0.0046	-	920

*equilibrium interfacial tension

For this reason, surfactant concentrations above the CMC values were chosen which have a more pronounced effect on the flow pattern map. The two concentrations (50 mM for C_{12}TAB and 5 mM for C_{16}TAB) were selected because at equilibrium they result in systems with similar interfacial tension; these two surfactants, however, have different absorption kinetics during the droplet formation process (Kovalchuk et al., 2018).

The viscosity of each surfactant was measured with an Advanced Rheometric Expansion System (ARES, TA Instruments®); all solutions are Newtonian. Given the lack of a reliable method for the measurement of the dynamic interfacial tension on the time scales of droplet formation in microchannels (Berry et al., 2015) (the drop formation time in the present study is below 1s), the dynamic surface tension (liquid/air interface,) is used as a guideline for the dynamic interfacial tension. The dynamic surface tension measurements were conducted using a maximum bubble pressure tensiometer technique which can provide results in a milli-second time scale (Kovalchuk et al., 2018). C_{12}TAB and C_{16}TAB were found to have different adsorption kinetics. The C_{16}TAB system has high surface tension (close to the surfactant-free system ~ 66 mN/m) at short times and low surface tension values (close to the C_{12}TAB system) at long times. The C12TAB system equilibrates much faster having similar surface tension values at both short and long times (Kovalchuk et al., 2018).

During the maximum bubble pressure measurement, gas bubbles are produced through a capillary which is submerged into the sample liquid and its radius is known. The maximum pressure, ΔP_{MAX}, inside the gas bubble is obtained when the gas bubble has a completely hemispherical shape (at the top of the capillary) and its radius corresponds to the radius of the capillary, R_C. This maximum pressure correlates with the surface tension, σ_S, according to the Young-Laplace equation:

$$\sigma_S = \frac{\Delta P_{MAX} \cdot R_C}{2} \qquad \text{(Equation 3.4)}$$

3.1.3 Tracers and dyes

In order to measure the velocity profiles in both phases simultaneously, a fluorescent wavelength separation technique is adopted in the micro-PIV system. To separate the phases, two types of tracer particles with different fluorescent characteristics are added into each phase separately.

The specifications of particles and their behaviour into the fluids are crucial for the quality of the final PIV result. For example, fine particles degrade the image quality by making a murky

background and overly large particles do not follow the flow and distort the image interrogation process (Adrian and Westerweel, 2011). Firstly, an essential challenge is the identification of appropriate tracer particles that absorb and emit at suitable wavelengths and can be suspended in the liquid phases. The density and the refractive index of the particles are secondary considerations whereas the degree of agglomeration of dried particles in liquids is a crucial parameter to examine.

Although there are many options for particles that can be used in aqueous phases, there are very few commercial particles available for organic phases. In this work, the aqueous phase was seeded with 1 μm carboxylate-modified microspheres FluoSpheres® with red fluorescent colour (540/560 nm) whereas in the organic phase 2 different trace particles were tested separately: (1) 1 μm blue polystyrene microspheres Fluoro-Max® (350/440 nm) were used after a drying process (2) 1 μm blue silica microspheres Sicastar® (350/440 nm).

Since there are no commercial oil-dispersed fluorescent particles that satisfy the limitations of the existing set-up of the micro-PIV, i.e. sufficient fluorescent intensity, and wavelength of the laser beams available, a drying method has been developed for the polystyrene microspheres particles. Dyed polystyrene microspheres particles in water (Fluoro-Max®) are used as a base material. Some basic characteristics of polystyrene particles are presented in Table 3.3. These particles were dried in a vacuum oven at 30 degrees for 8 hours. After the drying process the particles were dispersed in the oil phase.

Table 3.3: Properties of the dyed polystyrene microspheres particles

Specifications	
Colour	Blue
Composition	Polystyrene
Concentration	1% solids
Mean diameter	1 μm
Refractive index	1.59 (25^{o}C)
Stability	>24 months

The challenge regarding the dispersion is to limit the production of clustered particles because of their hydrophilicity. A suggested in literature method to reduce clusters is to use a centrifugal separator (Oishi et al., 2011) where the heavier clustered particles are moving to the bottom. However, this technique did not work for the polystyrene particles causing gum-

like particles into the oil. Thus, they were suspended in the oil phase within an ultrasound bath to reduce or break any clusters (Figure 3.3a).

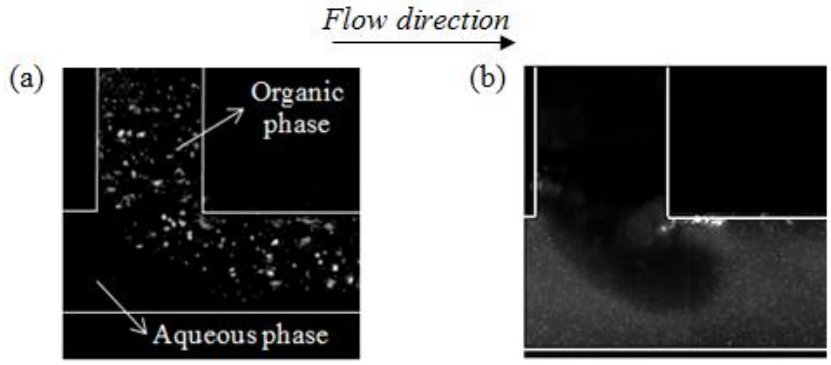

Figure 3.3: Micro-PIV illustration of (a) polystyrene fluorescent particles into the oil phase (b) rhodamine 6G into the aqueous phase during an aqueous/organic flow at the T-junction.

In order to reduce the degree of particle clustering and simplify the use of tracers, silica microspheres particles (Sicastar®) were also tested. They are white, spherical, silica particles with a surface modification namely trimethysilyl (TMS) which makes them stable in organic solvents. Silica particles were in a powder form and were suspended directly in the oil phase. They were found to produce better results compared to the dyed polystyrene particles with regards to agglomeration (less clustered particles), flow behaviour (fine particles that follow the flow) and background noise (less image distortion).

In the aqueous phase, a fluorescent dye is also added (in addition to the fluorescent red particles) to improve the detection of the aqueous-organic interface. 1 ppm of rhodamine 6G is diluted in the aqueous phase and used to increase the intensity between the two-phases as shown in Figure 3.3b. The organic phase is illustrated with a black background whereas the aqueous phase with a white one (Figure 3.3b). As a result, the interface is smoother and easier to detect with the micro-PIV. Furthermore, the precision of the measurement of the plug characteristics (plug length and shape) increases as the dye determines a sharp liquid-liquid interface. Without the dye, the only determination of the interface would be by the fluorescent particles which result in less well defined boundary. It was found that neither the fluorescent dye nor the tracer particles affected the properties of the phases or the flow pattern map.

3.2 Experimental set-up

3.2.1 T-junction test section used for the study of the shear-thinning fluids

The T-junction microchannel (Figure 3.4), used for the experiments with shear-thinning fluids, was made of two semi-circular channels, etched on quartz chips that were bonded together thermally (Dolomite® microfluidics). The inner diameter of the circular main channel was 200 μm. The T-junction inlet was etched in the same quartz chip as the main channel and its branches had the same size as the main channel. Using separate syringe pumps (KDS Scientific®), the two fluids were brought together into the T-junction inlet. The silicon oil was used as the dispersed phase and it was pumped via the side channel (see Figure 3.4).

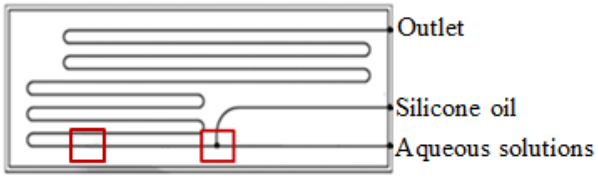

Figure 3.4: Schematic of the T-junction microchannel (Dolomite® microfluidics) used for the investigation of the shear-thinning fluids. Rectangular frame indicates the areas of measurements.

The water/glycerol solutions containing xanthan gum were the continuous phase and were injected into the central channel. Experiments were conducted at different combinations of flowrates of the two phases that varied from 0.01 to 0.1 cm^3/min and the areas of interest were both the T-junction inlet and the main channel (Figure 3.4). In each set of experiments, the aqueous (continuous) phase flow rate was kept constant whereas the organic (dispersed) phase flow rate was increased stepwise. Plug flow (Figure 2.4) was observed at low dispersed phase flowrates (Q_D = 0.01 - 0.03 cm^3/min) and at medium continuous phase flowrates (Q_C = 0.06 - 0.08 cm^3/min) both for Newtonian and non-Newtonian continuous phases. To ensure steady conditions inside the microchannel, an incubation time of 20 minutes was allowed before capturing data. This time was enough for the microflows to reach a periodic state (continuous flow of plugs and slugs) as can be seen by the small variability of the plug length data from the mean value: CV = 2-5% (for all flowrate conditions, CV = S.D/mean value)

3.2.2 Flow-focusing test section used for the study of the surfactants

The experiments on surfactants were conducted in a glass flow-focusing device with cross-junction equal to 190 μm x 195 μm (depth x width) and feed and main channels equal to 190 μm x 390 μm (Dolomite® microfluidics). Two syringe pumps (KDS Scientific®) were used to feed separately the two phases into the test section. The aqueous surfactant solutions (dispersed phase) were injected into the central channel whereas the silicone oil (continuous phase) was pumped via the two side channels. For each set of runs, the aqueous phase flow rate was kept constant and the organic phase flowrate was increased stepwise. The aqueous phase flow rates ranged from 0.01 to 0.1 cm^3/min, whereas the organic phase flow rates varied from 0.003 to 0.1 cm^3/min. The flow-focusing channel that was used to study droplet formation when surfactants are present is shown in Figure 3.5.

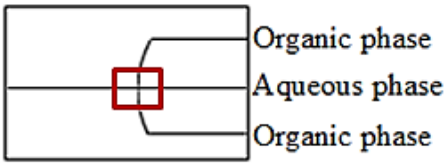

Figure 3.5: Schematic of the flow-focusing microchannel (Dolomite® microfluidics) used for the investigation of the surfactant-laden solutions. Rectangular frame indicates the area of interest.

3.2.3 Two-colour micro-PIV

A schematic of the two-colour micro-PIV experimental setup is shown in Figure 3.6. This technique is based on the use of two laser wavelengths to illuminate two different particle types, each seeded in one of the phases of a two-phase mixture, as mention before. For the illumination a double pulsed Nd:YAG laser unit (Nano PIV Litron Lasers®) with two independent laser cavities was used. The initial beam has a wavelength in IR (1066 nm). Using heated crystals, two different wavelengths, a blue (355 nm) and a green (532 nm) are generated by each laser cavity. The time delay between the two cavities is controlled by a synchronization unit (TSI synchronizer). Both laser beams are guided through an optical fibre to the microscope unit (Nikon Ti-400) with a 10x magnification and are reflected by a dichroic mirror on to the microscope objective where the test section is placed. The microscope dichroic mirror is designed to pass the 440 ± 40 nm and the 560 ± 40 nm wavelengths reflected from the particles.

Consequently, the incoming wavelengths from the laser are reflected while the emitted signals by the particles pass through the mirror. The fluorescent signals emitted from the particles are then directed through the objective and the dichroic mirror into a beam splitter unit (Andor® Technology).

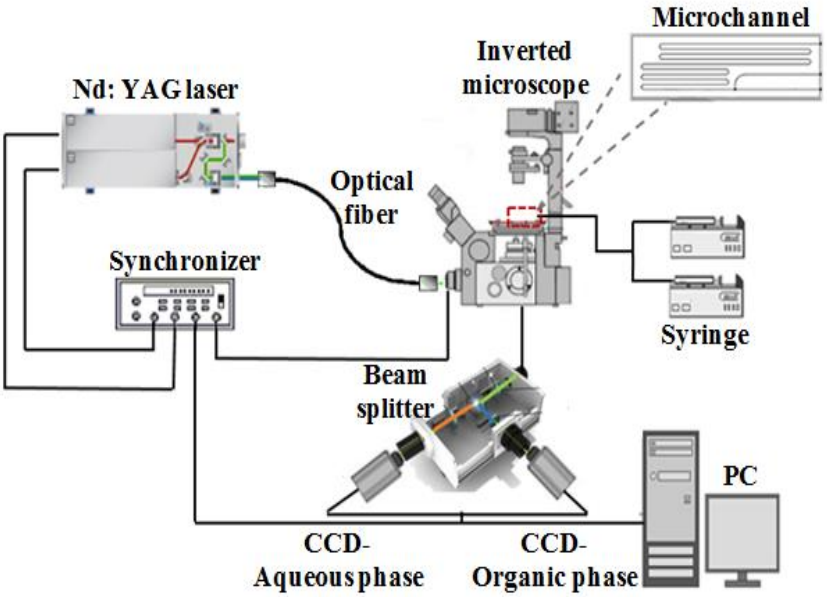

Figure 3.6: Schematic diagram of two-colour micro-PIV system.

Within the beam splitter unit, the fluorescent light from the particles is brought into a second dichroic mirror, which reflects the 440 ± 40 nm and passes the 560 ± 40 nm wavelengths. As a result, the red wavelength (560 nm) is led through the dichroic mirror and a high-pass filter towards a 4MP, 34fps CCD camera Link® Base (TSI, Powerview 4MP, with 2048 x 2048 pixels resolution and 2x magnification lens). The blue light (440 nm) emitted from the particles in the organic phase is reflected by the mirror and is led through a band pass filter to a 12-bit CCD camera Dicam pro® (PCO Sensicam, Dicam pro® with 1270 x 512 pixels resolution and 1x magnification lens). Both cameras are connected to the laser pulse synchonizer (TSI®), which controls the laser pulse delay time and the time between pulses necessary for the flow visualization and the image acquisition. The PIV acquisition frequency is 7 Hz per image pair (Roumpea et al., 2019)

One of the challenges of this micro-PIV system is the use of two different cameras to observe the two different phases. With this configuration, the phase discrimination is easier but additional barrier filters need to be installed in front of each camera increasing the energy losses. For the blue signal, the barrier optical filter is a pass band filter centred at 440 ± 50 nm, while for the red signal a high pass filter with a cut wavelength around 560 nm is used. It is

worth mentioning that if a single camera is used, beam energy losses will be reduced but the discrimination between the two phases will be more difficult. An additional complexity when using two cameras is that each has a different resolution, 1270×512 pixels for the blue camera and 2048 x 2048 pixels for the red CCD camera. Post- processing is then necessary to match the signal recorded by the two cameras.

Another issue to take into account is the weak signal of the blue fluorescent light. There is significant energy loss of the initial laser beam in the generation of harmonics and the blue laser beam is the weakest one (approximatively 50% of the initial beam energy). In addition, the multiplication of the dichroic mirror is further decreasing the beam energy. Further energy losses occur at the optical filters. Consequently, the fluorescent signal after the beam splitter unit is quite weak. Therefore, the sensitive camera, and more specific its gain, is crucial for recording the blue particles signal (Chinaud et al., 2015).

3.3 Data analysis

3.3.1 Two-colour μ-PIV image processing

The acquired PIV images are processed using the image processing software Insight 4G, TSI® and processing routines programmed in MATLAB R2014a. The data-processing steps are illustrated in Figure 3.7 using a newly growing droplet that forms inside a cross-junction channel. The droplet is a water/glycerol solution containing both carboxylate-modified microspheres (FluoSpheres® with red fluorescent colour) and rhodamine 6G. The organic phase is illustrated with a black background. To trace the interface based on the fluorescent 6G dye signal, the raw images (Figure 3.7a) are filtered by using a median filter based on 7×7 pixels computation and binarized to black and white using a threshold value (Figure 3.7b). The threshold is calculated based on the intensity histogram of the grayscale image. This process takes care of the non-uniform background illumination and improves the velocity field computation as the difference in the mean intensity between two consecutive images is enhanced and consequently the displacement of the seeding particles can be measured with higher accuracy. For both phases, the threshold value is also used to reconstruct the liquid-liquid interface by fitting the contour of the binarized region (Figure 3.7c).

A velocity range filter is defined and valid velocity vectors are chosen based on standard deviation and a primary-to-secondary correlation peak ratio (Gaussian peak algorithm). For

both cameras, the removed false vectors are replaced by the median value computed from the neighbour velocity values and vectors outside the corresponding seeded phase are set to zero.

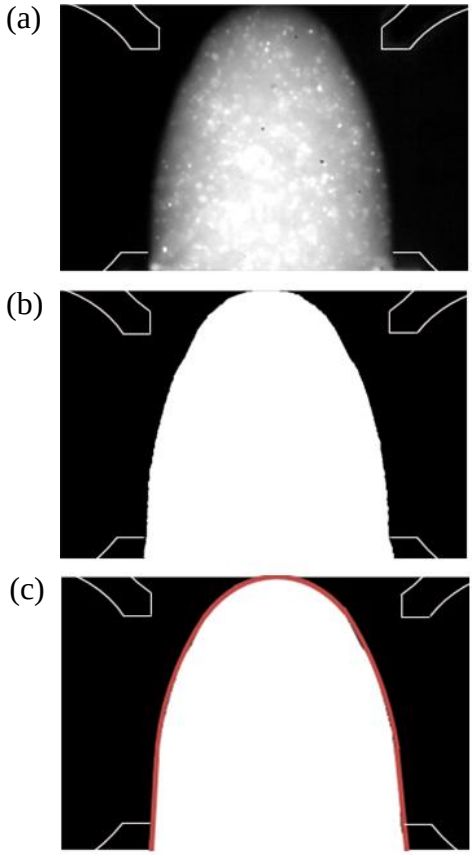

Figure 3.7: Steps of PIV processing: (a) raw PIV data (b) binarization of image (c) adaptive mask. The channel walls have been added for clarity.

The PIV correlation box size was set to 64×64 pixels with 50% spatial overlapping which results in a final spatial resolution of 11.9×11.9 μm. For the camera recording the organic phase, the interrogation area was set to 128×64 pixels, without overlapping, leading to a spatial resolution of 132.8×66.4 μm and a clear displacement of the organic phase vectors. For the computation of the velocity fields, a recursive Nyquist grid with an FFT correlation was used and the two-component velocity field was reconstructed within the Eulerian frame of reference.

To match the velocity fields of the two phases in the same frame, the contours of the reconstructed and binarized interfaces of both the aqueous and the organic phase images were used as an adaptive mask for the image of each camera. Further to this, a raw image of the microchannel boundaries was acquired and used as calibration target to match the two recorded signals of the cameras. For each experiment, the time delay between the two laser pulses was adjusted from 40 μs to 3000 μs (depending on the flow rate of both phases) so that the maximum particle displacement would not exceed half of the final correlation box size.

Image pairs were recorded during the droplet formation process. Since the acquisition frequency of the system is low (7 Hz), the drop formation process could not be resolved in time; instead image pairs were acquired at different positions of the droplet tip (for the flow-focusing experiments) and at different positions of the droplet neck inside the channel (for the T-junction experiments). To calculate averaged velocity fields at the inlet, 1000 micro-PIV images were obtained in each run. Depending on the flowrates, about 100-200 of the images were averaged to obtain the velocity fields at each droplet position.

Different plugs were recorded, during the plug flow in the main channel, which were not necessarily in the same position. To calculate average velocity fields in each phase, the images obtained from each camera were centred using the tip plug position as reference. For the average velocity fields, 600 micro-PIV images were acquired in the main channel. However, only 200 to 300 of the images, depending on the flowrate conditions, corresponded to full-length plugs and were used for the velocity field calculations.

3.3.2 Two-colour μ-PIV error sources

PIV is one of the most advanced experimental methods in fluid mechanics for the measurements of instantaneous velocity fields. However, due to the complexity of the configuration, a number of error sources affect the results. Understanding all the constrains of the system, i.e. laser energy, suitable optical system (field of view, spatial resolution), transparent fluids, appropriate seeding of fluids, test section design, etc. is crucial for the final accuracy of the results (King et al., 2007).

A primary source of error is related to the inertia effects between the particles and the fluid motion. If external forces (gravitational, centrifugal and electrostatic) can be considered negligible, the tracking capability of particles is influenced by the particles shape, diameter and density and by the fluid density and viscosity. Using the Stokes drag-law analysis for small particles and small Reynolds number ($Re < 1$), the time response for a particle immersed in a flow at rest and suddenly set into constant acceleration is estimated to be 10^{-8} s (Silva et al., 2008). For the present system, the characteristic time scale of flow, defined by the time interval between two consecutive laser pulses, varies from 10^{-5} s to 10^{-3} s (depending on the flowrates of both phases) and is several orders of magnitude larger than 10^{-8} s. Thus, the error due to the inertial effects of particles is negligible.

An additional uncertainty that has to be taken into account is the computation of the highest peak in the correlation plane during the in-plane velocity calculation. This uncertainty in

locating the correlation peak is closely related to the particles image size (d_e), which is the size that the particle appears on the camera, and is calculated according to the following equation:

$$d_e = \sqrt{M^2 d_P^2 + d_S^2} \quad \text{(Equation 3.5)}$$

$$d_S = 2.44M \frac{\lambda_O}{2NA} \quad \text{(Equation 3.6)}$$

where M is the magnification of lens, λ_O is the barrier filter for imaging, NA is the numerical aperture, d_S is the diffraction-limited resolution and d_P is the particle diameter. Based on the optical parameters of the setup, the effective particle diameter, d_e, was found to be 25 μm for the red fluorescent particles and 20 μm for the blue ones providing an uncertainty equal to $d_e/10M$ = 0.25 μm for the aqueous phase and $d_e/10M$ =0.20 μm for the organic phase (Silva et al., 2008). Given that the interrogation area is 11.9×11.9 μm for the aqueous phase and of 132.8×66.4 μm for the organic phase, the uncertainty is two orders of magnitude smaller and consequently does not influence significantly the velocity measurements.

The focal plane was located at the centre of the channel using the front wall as reference and maximizing the channel width adding an uncertainty of ±2% in any data that was based on pixel measurement (one pixel has ±1% uncertainty). The depth of the measurement volume in the μPIV measurements, δ_Z, was also calculated as follows:

$$\delta_Z = \frac{3n\lambda}{NA^2} + \frac{2.16d_p}{tan\theta} + d_p$$

where n is the refractive index of the medium in which the lens is working, λ is the wavelength of the laser, NA is the numerical aperture of the objective lens, d_P, is the particle diameter and θ is the half-cone angle of light captured by the objective lens. The PIV measurement depth for the blue (355 nm) and green (532) wavelengths is 20 and 26 μm respectively using the 10x objective lens.

Finally, the syringe pumps (KDS Scientific®) were calibrated (by collecting an amount of liquid over a period of time) and the maximum uncertainty of the flow rates was ±2%.

3.4 Overview

A detailed description of the liquids and the experimental setup used in the thesis were presented in Chapter 3. The properties of the complex fluids (xanthan gum and surfactant-laden solutions) were given together with the characterization methods used for the examination of

the solutions. In addition, the characteristics of the two different channel geometries i.e. T-junction and flow-focusing, utilized for the flow experiments were presented along with a thorough illustration of the two-colour micro-PIV technique. Finally, the processing methodologies used to analyse the PIV images and to acquire the local velocities of both phases were discussed.

4. Chapter 4: Plug formation in shear-thinning fluids using a T-junction microchannel

The formation of organic plugs in non-Newtonian aqueous solutions is experimentally investigated in the T-junction microchannel and compared against the results with Newtonian solutions. The effects of flowrate and shear-thinning viscosity on the hydrodynamic characteristics and the velocity profiles in both phases are studied using the Two-colour Particle Image Velocimetry technique. A mechanistic model is also developed to describe the evolution of the forces acting at the plug during the formation process.

4.1 Flow pattern map

For the investigation of the shear-thinning behaviour in small channels, two aqueous glycerol solutions (52% w/w) containing xanthan gum at different concentrations (1000 and 2000 ppm) were used as the non-Newtonian fluids whereas a silicone oil was used as the organic phase. The shear-thinning experiments were conducted in the T-junction channel as it has been presented in Section 3.2.1. For all conditions studied (i.e. phase flowrates between 0.01-0.1 cm^3/min) two different flow patterns were found, namely *plug* and *parallel flow*. In plug flow, the organic 0.0046 Pa s Newtonian phase always forms the plugs (Figure 4.1a) irrespective of the side branch of the T-junction used to introduce it in the main channel. In the parallel flow pattern (Figure 4.1b), the two liquids come in contact at the T-junction and then move in parallel along the channel.

The different flow patterns are attributed to the competition among interfacial, inertia and viscous forces. The interfacial forces tend to minimize the interfacial area resulting in plug flow whereas the viscous forces tend to keep the interface smooth. The inertial force extends the interface in the flow direction and dominates in the parallel flow pattern (Foroughi and Kawaji, 2011). The different patterns are plotted in Figure 4.1 for the Newtonian and the 1000 ppm non-Newtonian aqueous phase, in a map with the phase flowrates as coordinates. The patterns for the 2000 ppm non-Newtonian solution are the same as those for the 1000 ppm solution and therefore they are not presented. The flow patterns were found to remain constant across the length of the channel (see also Appendix A). As can be seen in Figure 4.1, for the Newtonian aqueous phase, the plug flow is limited to low dispersed and medium continuous

phase flowrates (points inside the dashed square). The range of conditions for plug flow is however, significantly expanded when the non-Newtonian aqueous solution is used. In particular, plug flow occurred for the whole range of the continuous (aqueous) phase flowrates studied and for an extended range of dispersed (organic) phase flowrates. As the dispersed phase flow rate is further increased and the shear force of the continuous phase is not large enough to break the interface into plugs, parallel flow forms (Figure 4.1b).

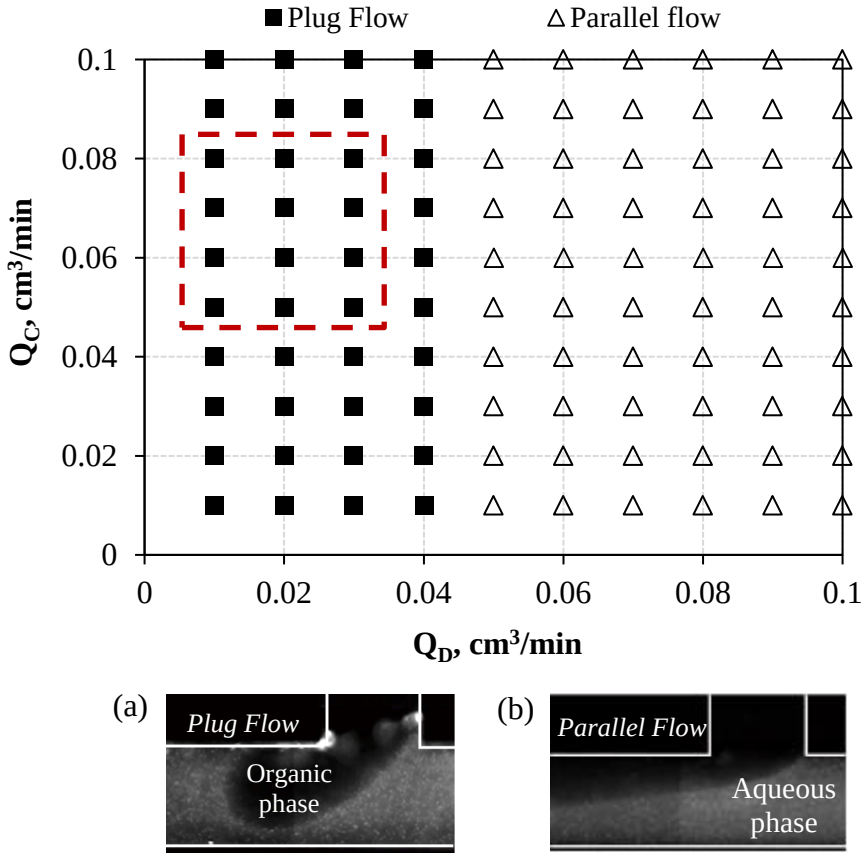

Figure 4.1: Flow pattern map of the aqueous Newtonian (N) and non-Newtonian 1000 ppm solution and the silicone oil. Representative flow patterns (a) plug flow (b) parallel flow. The dashed rectangular indicates the area of plug flow when the Newtonian aqueous phase is used.

The shift in the boundary between the plug and the parallel flows with the polymer addition could be due to both the change in the viscosity and the non-Newtonian rheology of the aqueous continuous phase. A similar trend was also found by Fu et al. (2015) who investigated the flow patterns of cyclohexane (dispersed phase) and shear-thinning non-Newtonian aqueous solutions (continuous phase) containing different concentrations of carboxylmethyl cellulose. They observed that the transition from droplet to parallel flow occurs at lower superficial velocity of the continuous non-Newtonian phase with increasing carboxylmethyl concentration. Numerical simulations of droplet formation in power law fluids in T-junction

channels by Sang et al. (2009) revealed that the droplet diameter decreases with an increase of both the consistency index, K, and the flow behaviour index, n. The authors found that with increasing K (viscosity behaviour) and under constant exponent, n (shear-thinning behaviour) the dispersed phase is pulled downstream into the main channel forming a longer segment before plug detachment. On the contrary, the plug breaks closer to the T-junction inlet as the shear-thinning behaviour becomes stronger (exponent n decreases) under constant K. Generally, for the 1000 and 2000 ppm non-Newtonian systems a transition region was found for all the continuous phase flowrates studied. As the dispersed phase flowrate increases, for constant Q_C, plugs with irregular sizes appeared before parallel flow was established. This transition region occured for Q_D between 0.04 and 0.05 cm^3/min.

The hydrodynamic characteristics and velocity fields of the plug flow are further studied in the T-junction inlet using the two-colour micro-PIV system for the cases indicated below in Table 4.1. $Ca_{(N)}$, $Ca_{(N1)}$, $Ca_{(N2)}$ (as they have been defined in Section 3.1.1, Equation 3.1) represent the Capillary number of the Newtonian, 1000 ppm and 2000 ppm solutions respectively.

Table 4.1: Experimental conditions corresponding to plug formation.

Test	**Q_C (cm^3/min)**	**Q_D (cm^3/min)**	**$Ca_{(N)}$**	**$Ca_{(N1)}$**	**$Ca_{(N2)}$**
1	0.06	0.01	0.007	0.012	0.022
2	0.06	0.02	0.008	0.013	0.022
3	0.06	0.03	0.009	0.014	0.024
4	0.07	0.01	0.010	0.014	0.023
5	0.07	0.02	0.011	0.015	0.024
6	0.07	0.03	0.013	0.015	0.025
7	0.08	0.01	0.011	0.014	0.025
8	0.08	0.02	0.012	0.015	0.026
9	0.08	0.03	0.013	0.017	0.027

4.2 Plug formation process

Plugs form at the T-junction at low dispersed phase flowrates (Q_D = 0.01-0.03 cm^3/min), where the Capillary numbers ($Ca = \mu_C \cdot U_P/\sigma$, where μ_C is the shear-thinning viscosity, u_P is the average plug velocity and σ the interfacial tension) are typically small, ~10^{-3}. As a result,

the shear forces between the liquids are low and the pressure that builds up in the continuous phase behind the plug leads to break-up (Garstecki et al., 2006). During this squeezing regime, the formation of a plug inside the Newtonian aqueous solution (N) can be divided in three discrete stages: expansion, necking, and pinch-off, as can be seen in Figure 4.2. At the expansion stage (Figure 4.2a-b) the forming interface is expanding into the T-junction inlet and the plug grows along the y-axis towards the opposite channel wall. When it reaches its maximum length (or minimum gap, see Figure 4.2b) inside the T-junction, the shear forces exerted by the continuous phase on the interface deform the plug and cause it to grow in the direction of the flow in the main channel (Figure 4.2b). This corresponds to the end of the expansion stage and the beginning of the necking stage (Figure 4.2c).

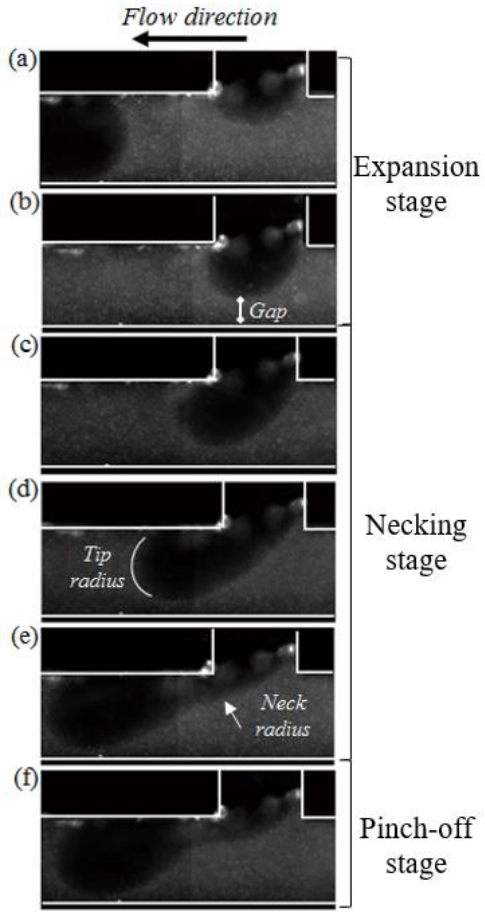

Figure 4.2: Typical PIV images of plug formation in Newtonian continuous phase (N) in the T-junction channel: (a)-(b) expansion stage, (c)–(e) necking stage, (f) pinch-off stage (for Q_D =0.02 cm^3/min and Q_C = 0.07 cm^3/min). Gap is the distance between the forming interface and the far channel wall; Tip radius is the radius of the leading edge of the plug; Neck radius is the radius of the back part of the plug.

The forming plug obstructs the main channel and the continuous phase has to flow through a smaller gap next to the wall while the pressure at the back of the plug increases. The high shear in the continuous phase and the increased pressure at the back of the plug lead to the formation of a neck (necking stage, Figure 4.2c-e). During the necking stage, the back part of the plug is pushed by the continuous phase towards the inner corner of the T-junction. As a result the neck radius increases and eventually its curvature changes sign, which indicates the beginning of the pinch-off stage (Figure 4.2f). Similar observations regarding the change of the neck curvature during plug formation in T-junction channels have also been made by Steijn et al. (2010) and Glawdel et al. (2012b). Eventually, the thinning of the neck accelerates and the plug detaches. The newly formed plug is pushed downstream by the continuous phase and the formation process is repeated.

When the xanthan gum polymer is added in the aqueous phase, the same three stages of formation (expansion, necking, pinch-off) can be observed. However, during the expansion stage the plug occupies a smaller area in the T-junction inlet compared to the Newtonian case (N). For example, the gap between the dispersed phase and the opposite channel wall at the end of the expansion stage (Figure 4.2b) increases approximately from 65 μm in the N solution to 112 μm in the N1 solution under the same flowrates (Q_D =0.02 cm^3/min and Q_C = 0.07 cm^3/min).

The differences in the plug formation process in the T-junction inlet between the Newtonian solution and the 1000 ppm xanthan gum solution (N1) can be seen in Figure 4.3, for Q_D =0.02 cm^3/min and Q_C = 0.07 cm^3/min. Since the process cannot be time resolved (low-speed micro-PIV) different plug propagation positions have been identified by tracking the axial location of the thinnest part of the neck with a MATLAB code. The measurements of the neck location start from the right, upper corner of the T-inlet (neck location equals to zero). The time difference between the positions is unknown and the successive images based on the neck location, as shown in Figure 4.3, demonstrate the plug formation process. The addition of xanthan gum in the aqueous phase increases the viscosity and the viscous shear forces exerted by the continuous phase to the plug. As a result, the plugs in the non-Newtonian solutions do not expand as much into the main channel in the expansion stage compared to the Newtonian ones but instead they are pushed against the upper channel wall, further into the main channel, and form a filament. The location of detachment moves further downstream from the inlet into the main channel as can be seen in Figure 4.3b (neck location 353 μm). The plug fronts at the later stages of plug formation for the 1000 ppm solution are outside the camera field of view and are not shown in Figure 4.3 (neck locations 235 μm, 309 μm and 353 μm).

The 2000 ppm system was found to have similar behaviour to the 1000 ppm case. With increasing amount of xanthan gum (N2 solution), the K consistency index (indicating viscosity) increases from 0.55 (N1 solution) to 0.85 (see Table 3.1) whereas the flow behaviour index n (indicating shear-thinning behaviour) is similar in both solutions. The increased viscosity of the 2000 ppm solution shifts the neck break-up location further downstream from the inlet compared to where the N1 solution breaks into plugs; for example at Q_D =0.02 cm^3/min and Q_C = 0.07 cm^3/min the plug forming in the N2 solution breaks at 370 μm from the inner T-junction corner compared to the 353 μm distance in the N1 case. Similar results were found by Yao et al. (2018) who studied liquid-liquid droplet formation in PDMS T-junction channel using octane as the dispersed phase and different concentrations of glycerol/water solutions as the continuous phase. They found that with increasing amount glycerol concertation and thus increasing continuous phase viscosity the plug detachment happened further downstream the T-junction. The break-up location was also found to be shifted downstream from the T-junction inlet with increasing dispersed phase flowrate.

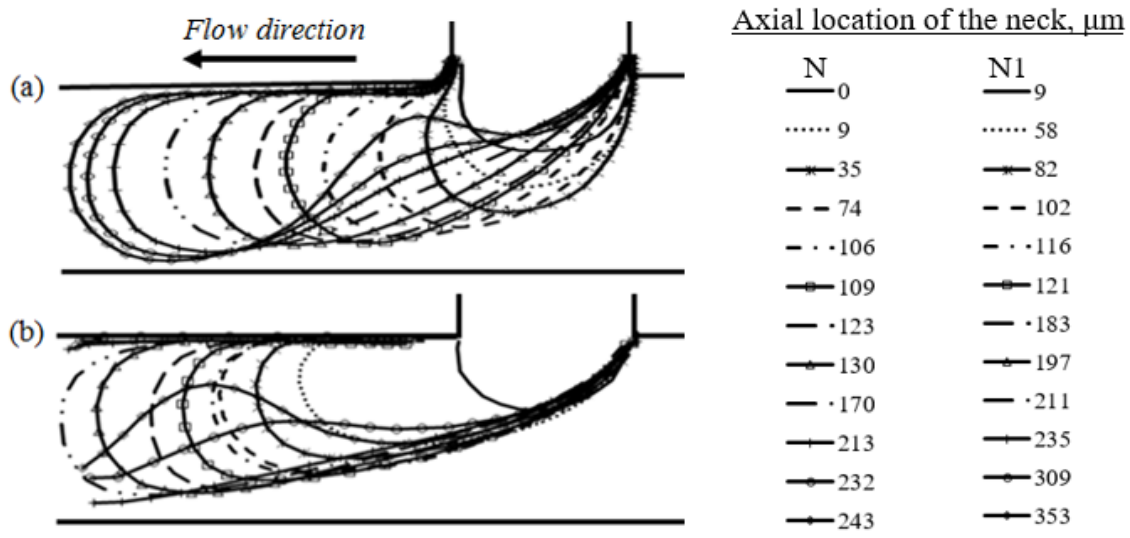

Figure 4.3: Plug formation in T-junction inlet for (a) N and (b) N1 continuous phase for constant flowrates Q_D =0.02 cm^3/min and Q_C = 0.07 cm^3/min. Channel walls have been added for clarity.

4.3 Plug characteristics

4.3.1 Tip radius

The addition of xanthan gum is found to affect the curvature of the leading tip of the plug. This is shown in Figure 4.4 where the tip radius, R_T, is plotted against the location of the thinnest part of the neck measured from the right, upper corner of the T-inlet. The radius was obtained from the μPIV images by fitting a circle on the plug tip (see Inset in Figure 4.4). Generally, during plug formation the tip radius increases (tip curvature decreases) as the plug grows into the main channel for all three aqueous solutions (Figure 4.4). The increase in the tip radius is more pronounced after the beginning of the necking stage (where the tip of the forming plug is growing in the direction of the flow) at 74 μm, 82 μm and 90 μm for the N, N1 and N2 solutions respectively.

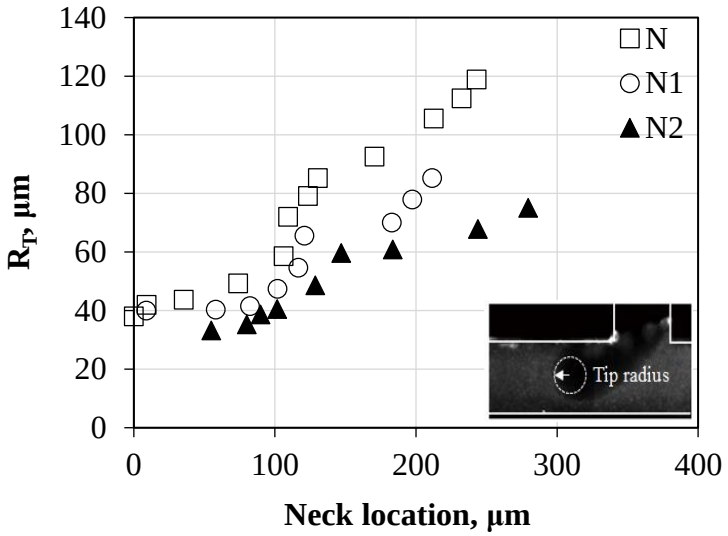

Figure 4.4: Effect of non-Newtonian rheology on the tip radius during plug formation for constant flowrates Q_D =0.02 cm^3/min and Q_C = 0.07 cm^3/min. The last points ○ and ▲ of the 1000 ppm and 2000 ppm respectively are missing as the plug tip is out of the field of view of the cameras. Inset: Tip radius of plug.

With increasing xanthan gum concentration, the tip radius decreases (tip curvature increases), and the forming plug acquires a more bullet-shaped profile compared to the Newtonian solution. In the N2 system, the measurements of the tip radius start at 54 μm, instead of 0 μm, as the first plug position captured with the PIV is already inside the main channel (there were no images captured in the expansion stage as the plug breaks further downstream from the T-junction and the dispersed phase never returns into the dispersed phase channel).

During the expansion stage (Figure 4.4, neck position < 74 μm) the forming plug is restricted to the upper part of the main channel where the shear rates are large (~ 800 s^{-1}; as shown later in Figure 4.9) and the viscosities of the non-Newtonian solutions are low (~ 0.018 Pa s for N1 and ~ 0.023 Pa s for N2, see Figure 3.1) approaching that of the Newtonian one (μ ~ 0.007 Pa s). Because of this, all three solutions have similar tip radius ~ 40 μm at this stage. During the necking stage, though (Figure 4.4, neck location > 74 μm), the plug tip is mainly located at the middle part of the channel where the shear rate values are lower (~ 15 s^{-1}, Figure 4.9) than the ones close to the channel wall. As a result, the viscosities of the non-Newtonian solutions are higher compared to the Newtonian one; the viscous forces seem to overcome the surface tension forces in the non-Newtonian solutions and the plug front becomes more pointed with an increased tip curvature. Generally, the tip radius was also found to increase with increasing continuous and dispersed phase flowrates.

4.3.2 Neck width and radius

The change in the neck width, W_N, during plug formation is presented in Figure 4.5 for the three aqueous solutions and for constant flowrates Q_D =0.02 cm^3/min and Q_C = 0.07 cm^3/min.

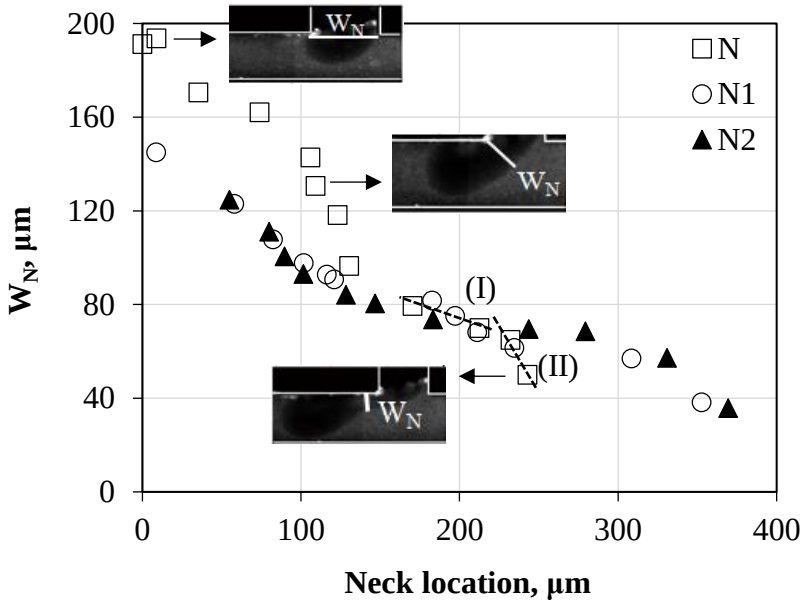

Figure 4.5: Neck width as a function of the neck position for all three aqueous systems studied. Constant flowrates Q_D =0.02 cm^3/min and Q_C = 0.07 cm^3/min. Inset: Neck width during plug formation. The dashed lines (I) and (II) have been fitted to the N data to show the change in the slope of the neck width from the necking to the pinch-off stage.

The last points of the neck width for all solutions correspond to the last images captured with the PIV system before the plugs detached. In the Newtonian case, N, the initial width of the plug is equal to the dispersed phase inlet channel width (200 μm) (Figure 4.5). As the plug grows into the main channel (expansion stage), the pressure that builds-up into the continuous phase starts to "squeeze" the dispersed phase and decrease slightly the neck size. The necking stage for the Newtonian solution takes place from 74 μm to 213 μm where the width of the neck decreases significantly. Eventually, a change in the neck curvature is observed indicating the end of the necking stage and the beginning of the pinch-off stage (Inset, Figure 4.5). This change in the curvature coincides with a change in the slope of the neck width as shown with the dashed lines (I) and (II) in Figure 4.5 and leads to the plug break-up.

The high viscosities of the N1 and N2 solutions compared to the N system increase the shear forces on the forming plug leading to smaller neck widths during plug formation (Figure 4.5). The two non-Newtonian systems give similar neck widths due to their similar rheological behaviour (Figure 3.1). The shift of the plug detachment location further downstream into the main channel can also be clearly seen; in the N case the plug pinch-off stage starts at 213 μm whereas in the N1 and N2 solutions this stage starts at 235 μm and 280 μm respectively.

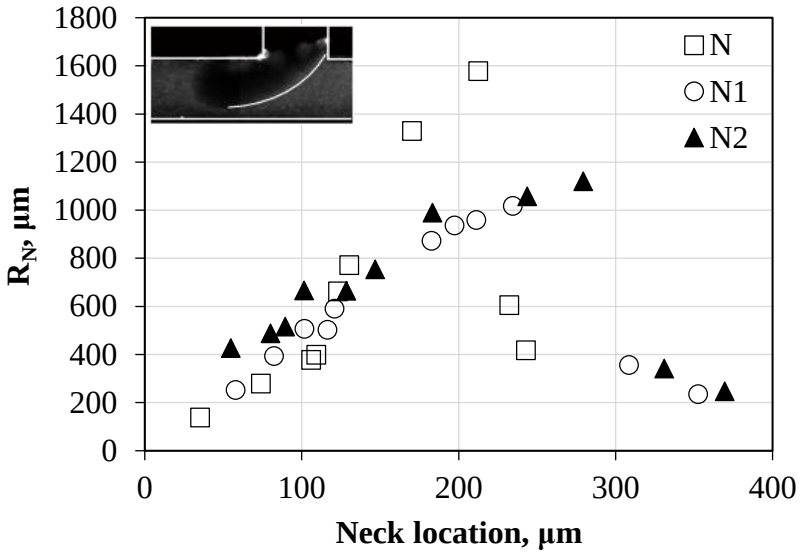

Figure 4.6: Neck radius as a function of the propagation steps for all three aqueous solutions studied. Q_D =0.02 cm^3/min and Q_C = 0.07 cm^3/min. Inset: Neck radius of plug.

The radius of the neck, R_N, was also measured during the plug formation as a function of the location of the neck inside the channel. Figure 4.6 presents the neck radius which is measured at the back part of the plug (see inset in Figure 4.6) for all the three aqueous solutions and Q_D =0.02 cm^3/min, Q_C = 0.07 cm^3/min. For all solutions the radius of the neck increases

significantly (curvature decreases) with plug formation. During the necking stage (which begins at 74 μm, at 82 μm and 90 μm for the N, N1 and N2 solutions respectively), the neck radius in the Newtonian case becomes larger than in the non-Newtonian solutions showing that the N plug grows towards the bottom channel wall (see Figure 4.3).

Conversely, the plugs in the non-Newtonian solutions are pushed by the continuous phase towards the upper channel wall and a neck with larger curvature forms. At the end of the necking stage, the radius decreases sharply at 213 μm for N, 235 μm for N1 and 280 μm for N2. The decrease signifies the change of the neck shape from convex to concave and the start of the pinch-off stage (last two points of neck radius for each solution in Figure 4.6) where the neck collapses towards the upper channel wall. The first data points corresponding to the expansion stage for the N (neck location 0 and 9 μm) and N1 (neck location 9 μm) solutions are not presented as the plug has not entered the main channel yet and neck has not formed.

4.4 Velocity fields and shear rate

Averaged velocity fields in both continuous and dispersed phases during plug formation are presented in Figure 4.7 and Figure 4.8 for the Newtonian and 2000 ppm solution respectively.

In the Newtonian case (Figure 4.7), as the dispersed phase leaves its inlet, a weak recirculation pattern is observed at the tip of the forming plug (Figure 4.7a-i). This recirculation probably happens because after the plug detachment, the dispersed phase pulls back slightly into its inlet channel before it moves forward again into the T-junction. The plug then grows into the main channel and no recirculation pattern is observed in the dispersed phase at the beginning of the necking stage (Figure 4.7b-ii). During the necking stage (Figure 4.7c-iii and Figure 4.7d-iv respectively), the forming plug obstructs the continuous phase and forces it to flow through a smaller gap, where the velocity increases. At the pinch-off stage (Figure 4.7e-v), the velocity acquires large values at the back part of the plug both for the continuous and the dispersed phases. During this stage, the neck curvature changes and the neck width decreases forming a recirculation pattern at the base of the neck. As a result, the dispersed phase stretches over two opposite directions i.e. back into the dispersed phase inlet and into the main channel. In Figure 4.7iv –v the tip of the plug was out of the field of view of the Dicam pro®camera (camera capturing the dispersed phase) and it is not shown here. Overall, during the plug formation, the maximum velocity in the continuous phase in front of the plug tip is always slightly larger than the velocity in the continuous phase before the forming plug (see

Figure 4.10a-b, Inset). Inside the plug the velocities increase gradually at the neck area, as the continuous phase pushes the plug downstream.

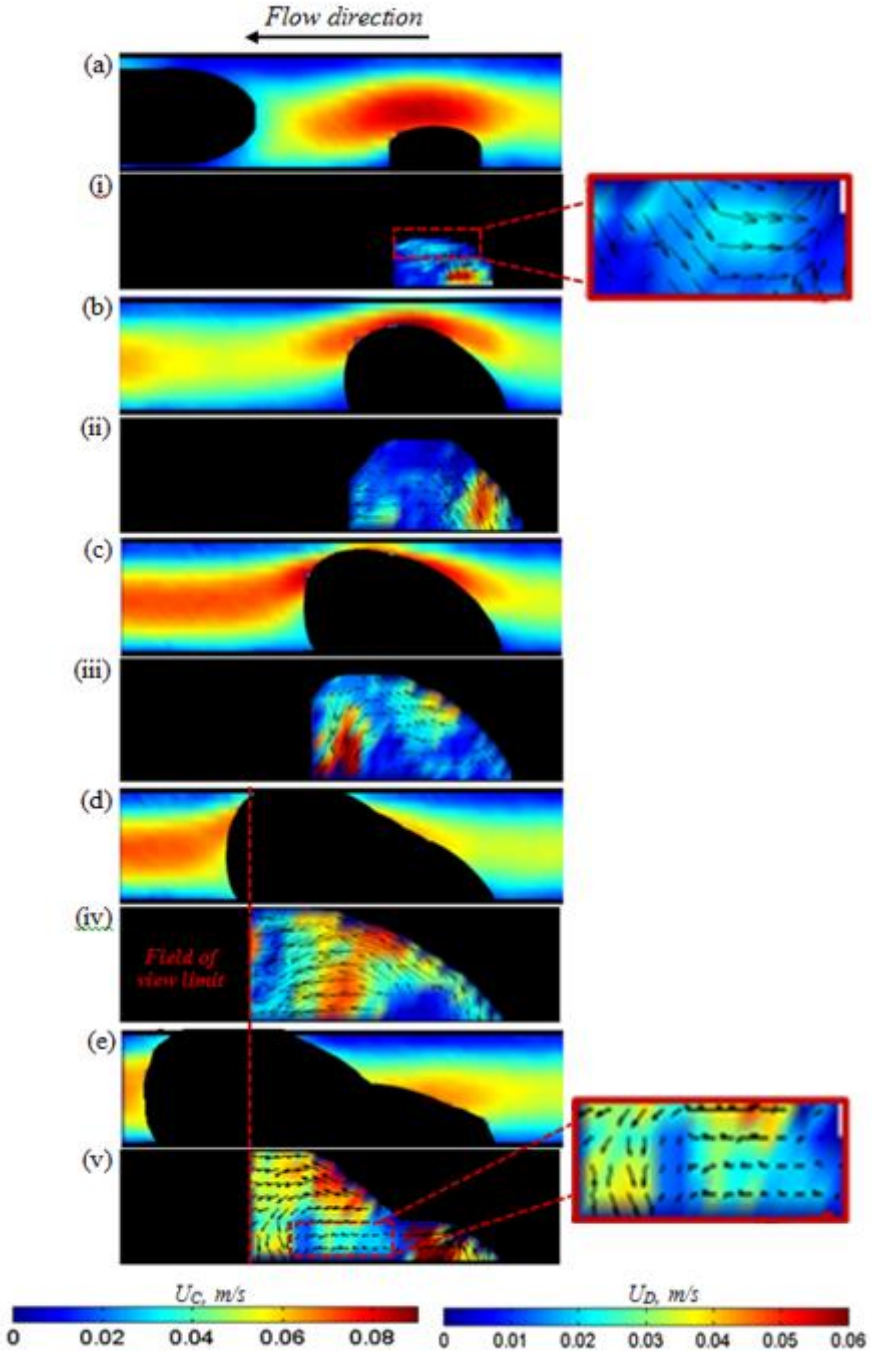

Figure 4.7: Averaged total velocity fields (a-e) in the continuous phase for the Newtonian solution and (i-v) in the dispersed phase. Q_D =0.02 cm^3/min and Q_C = 0.07 cm^3/min. Inset: Recirculation pattern inside the forming plug. Images a-i correspond to the expansion stage, images b-ii, c-iii, d-iv to the necking stage and images e-v to the pinch-off stage.

For the 2000 ppm solution (Figure 4.8), the flow inside the dispersed phase is generally slower compared to the Newtonian case, while no recirculation patterns can be observed during the expansion stage (Figure 4.8a-i) or the detachment stage (Figure 4.8e-v).

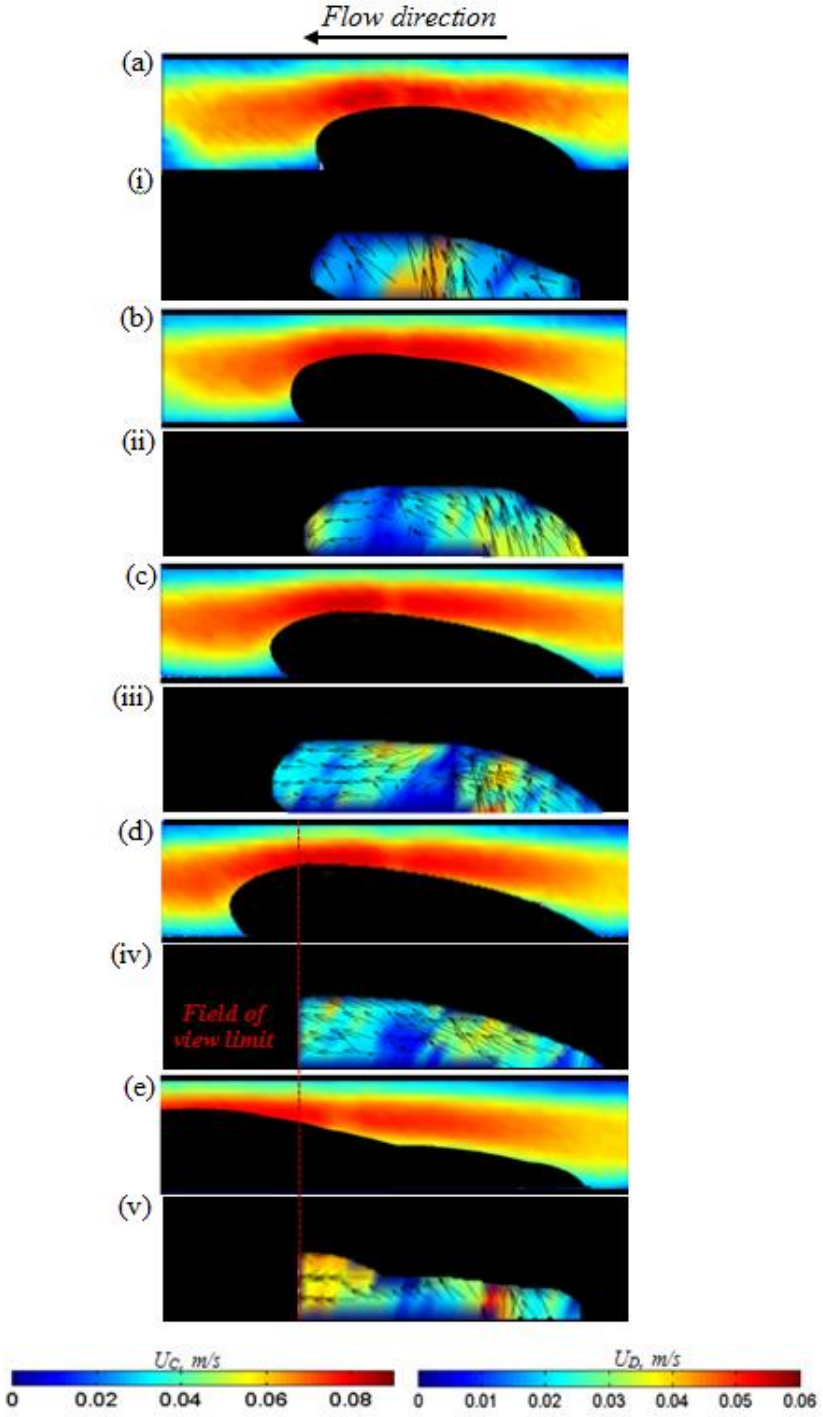

Figure 4.8: Averaged total velocity fields (a-e) in the continuous phase for the 2000 ppm solution and (i-v) in the dispersed phase. Q_D =0.02 cm^3/min and Q_C = 0.07 cm^3/min. Images a-i correspond to the expansion stage, images b-ii, c-iii, d-iv to the necking stage and images e-v to the pinch-off stage.

This is attributed to the higher viscosity (lower shear rate) of the continuous phase. The averaged shear rates in the continuous phase were calculated from the velocity fields and are plotted in Figure 4.9 for the Newtonian and 2000 ppm solutions and for the first image pairs obtained with the μPIV (Figure 4.7a and Figure 4.8a respectively). The shear rate was measured across the channel diameter and in front of the plug tip. As can be seen in Figure 4.9, the shear rate varies from ~ 800 s^{-1} close to the channel wall (D = 200 μm) to ~ 15 s^{-1} in the middle of the channel (D = 100 μm) leading to an increase in the N2 viscosity from ~ 0.023 Pa s (in the channel wall) to 0.12 Pa s (based on the rheological behaviour of the xanthan gum shown in Figure 3.1). In addition, the shear rate values obtained in the 2000 ppm solution are always lower than the corresponding ones in the Newtonian case at the centre of the channel for all the flowrates studied and for all the formation stages.

As the plug expands into the main channel (Figure 4.8b-ii - Figure 4.8d-iv) and the neck width reduces, the highest velocities in the dispersed phase are found at the neck area, similar to the Newtonian case. At the same time, the N2 continuous phase has slightly higher velocities at the back of the forming plug compared to the Newtonian system (Figure 4.7) for all formation stages.

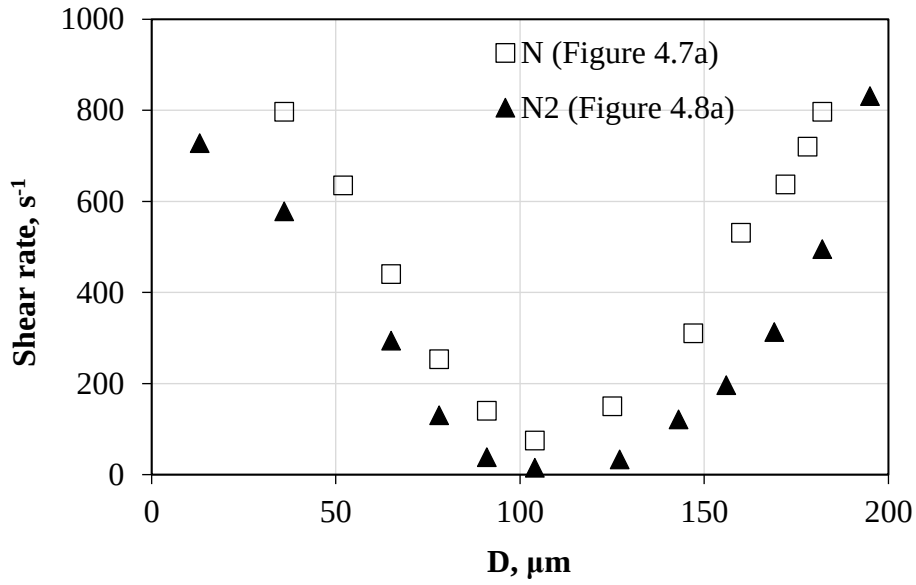

Figure 4.9: Averaged shear rate profile in the Newtonian (N) and 2000 ppm (N2) solution for the first image at the expansion stage obtained from the two-colour PIV. Q_D =0.02 cm^3/min and Q_C = 0.07 cm^3/min.

On the contrary, the maximum velocity in the N2 continuous phase is smaller in front of the forming plug for the first stages of plug formation than in the N case. This can be demonstrated

in Figure 4.10 where the average velocity profiles of the continuous phase are shown at two different positions inside the microchannel: (a) in front of the plug tip and (b) at the back of the plug neck for both the Newtonian and the 2000 ppm solutions (Figure 4.10, Inset). As can be observed, in the 2000 ppm solution, the continuous phase velocity remains almost constant (~0.075 m/s maximum velocity in front of the plug; ~0.06 m/s maximum velocity at the back of the plug) during plug formation whereas in the Newtonian solution the velocity reduces as the plug propagates inside the main channel (Figure 4.10a).

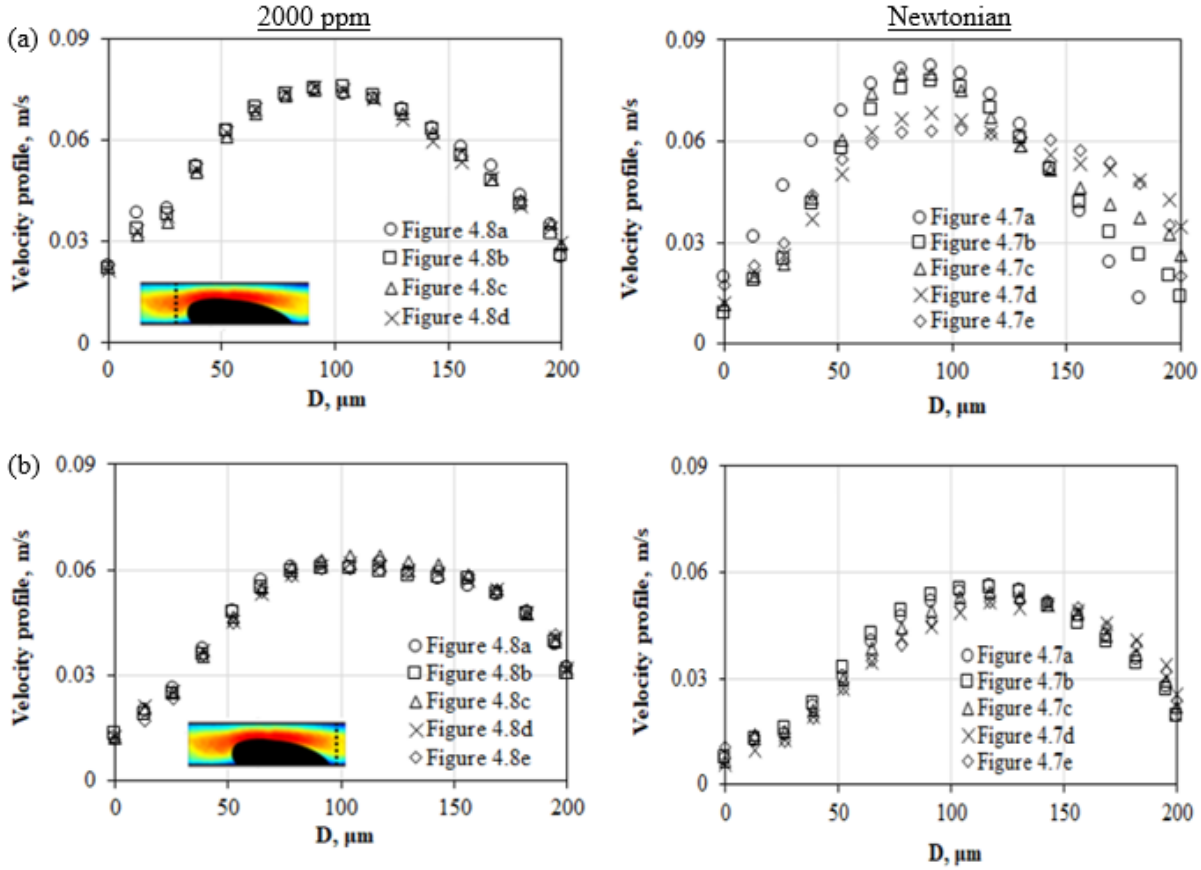

Figure 4.10: Average velocity profiles of the continuous phase velocity measured (a) in front of the plug tip (b) before the forming plug for the 2000 ppm and the Newtonian solution. Inset: Dotted lines indicate the area of measurement of the velocity profiles.

In addition to that, a no symmetrical parabolic profile (shifted to the right) can be observed at the back of the forming plug (Figure 4.10b) both for the N and N2 solution showing that the plug formation obstructs the continuous phase towards the bottom channel wall. Furthermore, it can be noticed that the velocity in the continuous phase in front of the plug (Figure 4.10a) is generally larger than the velocity in the continuous phase at the back of the plug (Figure 4.10b) both for the N and N2 solutions. The plug front at the last position of plug formation (Figure

4.8e) in the 2000 ppm case is outside the camera field of view and the velocity profile is not shown in Figure 4.10a.

4.4.1 Force balance during plug formation

The velocity profiles and the plug characteristics from the PIV measurements together with the rheology data of the xanthan gum solutions can be used to estimate the forces that govern the plug formation in a T-junction. In particular, the interfacial tension force that resists the plug formation and the drag force by the continuous phase that promotes the plug formation will be considered (Figure 4.11). The inertia force of the dispersed phase was found to be of the order of magnitude of 10^{-09} Kg m/s^2 and it was not taken into account. Following the models by Garstecki et al. (2006) and Glawdel et al. (2012b) the interfacial tension force, F_σ, can be found from the Laplace pressure difference, ΔP_L, between the tip and the neck of a forming plug:

$$\Delta P_L = \sigma(r_a^{-1} + r_r^{-1}) \qquad \text{(Equation 4. 1)}$$

where σ is the interfacial tension, r_a is the axial curvature and r_r is the radius of the radial curvature. Using the tip and neck radius data obtained by the PIV in Equation 4.1, the Laplace pressure at the tip and neck of a forming plug is equal to:

$$P_T = -\sigma\left(\frac{1}{R_T} + \frac{2}{h}\right) \qquad \text{(Equation 4.2)}$$

$$P_N = \sigma\left(\frac{1}{R_N} + \frac{2}{h}\right) \qquad \text{(Equation 4.3)}$$

where $\frac{1}{R_T}$ (R_T is presented in Figure 4.4) and $\frac{1}{R_N}$ (R_N is presented in Figure 4.6) represent the axial curvature of the plug tip and neck respectively whereas the radial curvature is bounded by the channel height, $\frac{2}{h}$. The minus sign in Equation 4.2 signifies that the Laplace stress at the tip is oriented upstream. The sum of the two Equations 4.2 and 4.3 multiplied by the area of the neck width, W_N, gives the interfacial tension force:

$$F_\sigma = -\left(\sigma \cdot \left(\frac{1}{R_T} + \frac{2}{h}\right) - \sigma \cdot \left(\frac{1}{R_N} + \frac{2}{h}\right)\right) \cdot \left(\pi \cdot \frac{W_N^2}{4}\right) \qquad \text{(Equation 4.4)}$$

which is oriented upstream resisting to any plug deformation (Figure 4.11). The neck width is chosen as characteristic parameter of the system instead of the cross-section of the channel (as in the work of Garstecki et al., 2006) which overpredicts the interfacial tension force.

In addition, the forming plug is subjected to a drag force by the continuous phase in the positive direction of the flow. The shear stress and the pressure gradient arising in the continuous phase as the plug forms into the main channel, lead to a hydrodynamic drag force, F_D that changes the neck curvature at the end of the necking stage.

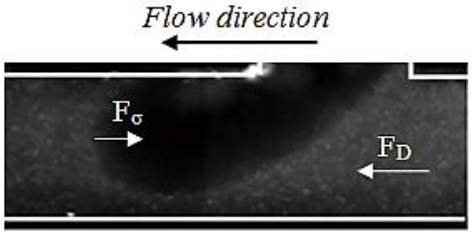

Figure 4.11: Schematic indicating the drag force (F_D) and the interfacial tension force ($F\sigma$) during the necking stage.

The drag force is defined as in the work of Husny and Cooper-White (2006) who studied the effects of the non-Newtonian rheology on the mechanism of drop formation and break-up inside a T-junction inlet:

$$F_D = \frac{1}{2} \cdot C_D \cdot \rho_C \cdot (U_C - U_D)^2 \cdot A_D \qquad \text{(Equation 4.5)}$$

where $C_D = \frac{8}{Re} \frac{2m+3}{m+1}$ is a modified drag coefficient that takes into account the effect of viscosity ratio, $m = \mu_C/\mu_D$ ($Re = \frac{\rho_c \cdot (U_C - U_D) \cdot D_D}{\mu_C}$ where D_D is the drop diameter and μ_C is the continuous phase viscosity), ρ_C is the density of the continuous phase fluid, U_C is the continuous phase velocity, U_D is the dispersed phase velocity and A_D is the cross-sectional area of a drop. By replacing C_D and Re and using the width of the tip, W_T, as characteristic parameter in Equation 4.5, the drag force is equal to:

$$F_D = 4 \cdot \mu_C \cdot \frac{(2m+3)}{(m+1)} \cdot \frac{1}{W_T} \cdot (U_C - U_D) \cdot \frac{\pi W_T^2}{4} = \pi \cdot \mu_C \cdot \frac{(2m+3)}{(m+1)} \cdot W_T \cdot (U_C - U_D) \quad \text{(Equation 4.6)}$$

It is worth mentioning, that Husny and Cooper-White (2006) expressed the continuous phase velocity by $U_C^* = 2 \cdot U_C \cdot \left[1 - (\frac{D - D_{drop}}{D})^2\right]$ (where D is the channel diameter and U_C is the averaged continuous phase velocity) assuming a parabolic flow profile inside the continuous phase channel. In the present study, the averaged continuous phase velocity in front of the plug, measured with the PIV, is used to calculate the U_C. For the plug velocity calculation, the dispersed phase flow rate (Q_D) and the channel area that corresponds to the plug growth during formation ($W_T \cdot \text{Height of channel}$) are used ($U_D = \frac{Q_D}{W_T \cdot H}$). This is because the plug tip is out

of the field of view for both the Newtonian and the 2000 ppm solution at the last stages of formation and therefore experimental U_D could not be measured. In addition, for the non-Newtonian continuous phase, the viscosity μ_C is defined as $\mu = K \cdot \dot{\gamma}^{n-1}$ (based on the averaged shear rate in front of the plug).

The evolution of these two forces is presented in Figure 4.12a and b for the Newtonian and 2000 ppm solutions against the axial location of the thinnest part of the neck. The evolution of the forces gives information on which parameters have great influence on the plug formation process and can predict when the pinch-off stage begins.

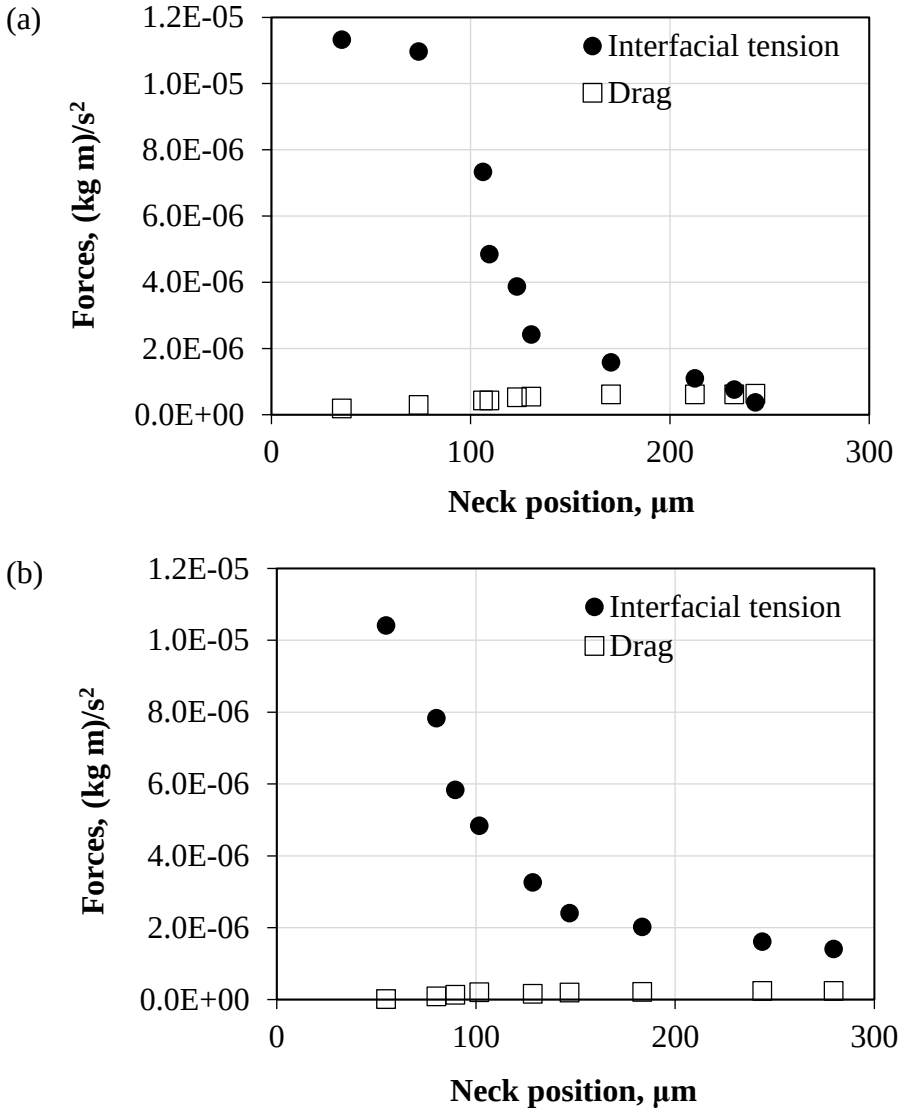

Figure 4.12: Evolution of forces during the plug formation of (a) Newtonian and (b) 2000 ppm solution. Q_D =0.02 cm^3/min and Q_C = 0.07 cm^3/min.

In the Newtonian case, the first two data points corresponding to the expansion stage (neck location 0 and 9 μm) have not been taken into account as the plug has not entered the main channel yet and there is no neck. As the plug grows into the channel and the neck thins, the interfacial tension force weakens mostly because of the decrease in the neck width, W_N. In addition to that, the inverse tip radius of the plug $\frac{1}{R_T}$ (see Figure 4.4) and the inverse neck radius $\frac{1}{R_N}$ (see Figure 4.6) also decrease during plug formation contributing to the reduction of F_σ. The increase in the $\frac{1}{R_N}$ at the pinch-off stage (last 2 points in Figure 4.6) seems not to affect the decrease of F_σ. At the same time, the velocity both in the continuous and dispersed phases increases (with $U_C > U_D$ at all times) leading to higher relative local velocity between the phases. As a result, the drag force gradually increases and overcomes the interfacial tension force at the neck position 232 μm for the Newtonian solution. At this position, the neck curvature changes indicating the beginning of the pinch-off stage and the end of the necking stage. In the 2000 ppm case (Figure 4.12b) the points that indicate the change in the neck curvature and the plug detachment are missing as the plug tip is out of the field of view of the cameras and therefore F_σ (Equation 4.4) and F_D (Equation 4.5) could not be calculated.

Using Equation 4.4 and Equations 4.5 at neck position 232 μm where the forces are almost equal, $F_D = F\sigma$, the width of the Newtonian plug tip is found equal to 287 μm (for Q_D =0.02 cm^3/min and Q_C = 0.07 cm^3/min). The width of the plug and the flowrate ratio can be used as inputs in the scaling law of Christopher et al. (2008), who based their model on the work of Garstecki et al. (2006), to find the dimensionless plug length:

$$\frac{L}{W_C} = \frac{W_T}{W_C} + \frac{\Lambda}{\frac{W_T}{W_C}} \cdot \frac{Q_D}{Q_C} = \frac{W_T}{W_C} + \frac{W_D}{W_T} \cdot \frac{Q_D}{Q_C} = 1.43 + 0.69 \cdot 0.28 = 1.62$$

where L is the plug length, W_C and W_D are the width of the continuous and dispersed phase channels respectively, Λ is $\frac{W_D}{W_C}$ and $\frac{Q_D}{Q_C}$ is the dispersed to continuous phase flowrate ratio. Here, $W_C = W_D = D$ = 200 μm. The dimensionless plug length found based on tip width and Garstecki's scaling law is ~ 21% higher than the dimensionless plug length, L/D = 1.34 (see Figure 5.3), that was measured experimentally in the main channel for the Newtonian case and for Q_D =0.02 cm^3/min and Q_C = 0.07 cm^3/min. To accurately predict the W_T, a more detailed model is needed to capture the pressure drop across the droplet correctly. This is not straightforward as the shape of the interface creates a curved boundary resulting in a 3D flow profile throughout the gap, which does not lend itself to a simple analytical solution (Glawdel

et al., 2012). In addition to that, the dimensionless plug length for the non-Newtonian cases could not be found at the T-junction as the plug tip was out of the field of view.

4.5 Overview and main conclusions

The formation of oil plugs in both Newtonian and non-Newtonian aqueous phases was studied in the T-junction microfluidic device. Xanthan gum polymer solutions at two different concentrations, 1000 ppm and 2000 ppm, were used as the aqueous phase, while glycerol was also added to match the refractive index of the organic phase. A two-colour Particle Image Velocimetry technique was used to obtain the flow fields in both phases and the characteristics of the forming plugs.

For all conditions studied (phase flowrates between 0.01-0.1 cm^3/min) two different flow patterns were found, namely plug and parallel flow. It was found that the addition of xanthan gum extended the area of plug flow to higher superficial phase velocities compared to the Newtonian case. It was also noticed that in the squeezing regime the plug formation could be divided in three discrete stages: expansion, necking, and pinch-off. In the expansion stage, the plug mainly expanded from the side channel of the T-junction into the main channel. The transition to the necking stage happened when the growth of the plug changed from the perpendicular to the main channel flow direction. The onset of the pinch-off stage happened when the neck curvature changed from convex to concave. The experimental results revealed that the plugs formed in the non-Newtonian solutions had larger tip (bullet-shaped profile) and neck curvatures and smaller neck widths compared to the Newtonian ones. Also, the addition of xanthan gum in the aqueous phase was found to shift the location of plug detachment further downstream from the inlet into the main channel leading to the formation of a dispersed phase filament. The velocity profiles in the Newtonian solution showed that during the expansion stage a weak recirculation pattern appeared at the tip of the forming plug, which gradually weakened as the plug moved into the main channel. This circulation was not obsereved in the 2000 ppm system which was attributed to higher viscosity of the continuous phase. As the plug propagated into the main channel and the neck decreased in size, the dispersed phase velocities increased in the neck region for all solutions. At the same time, the velocity in the continuous phase in front of the plug was always larger than the velocity at the back of the plug for both the Newtonian and the 2000 ppm solutions. Based on the velocity profiles and the geometric

characteristics of the forming plugs, the forces acting on them were estimated. It was found that drag forces overcame the surface tension ones in the beginning of the plug pinch-off stage.

5. Chapter: Plug flow in shear-thinning fluids

The hydrodynamic characteristics of the plug flow of the 0.0046 Pa s oil in the continuous non-Newtonian (1000 ppm and 2000 ppm) shear-thinning aqueous solutions were studied in the main channel, downstream from the T-junction inlet. Furthermore, measurements were carried out with the corresponding Newtonian aqueous solution (N, without xanthan gum) for reference and comparison. The effects of the continuous and dispersed phase flowrates and non-Newtonian viscosity on this two-phase flow were studied using the two-colour micro-PIV system.

5.1 Plug length

The effect of dispersed phase (silicone oil) flow rate, Q_D, on plug size is illustrated in Figure 5.1 when the Newtonian aqueous solution (N) is used as the continuous phase. The flow rate of the continuous phase is kept constant at Q_C = 0.07 cm^3/min whereas the channel walls have been added for clarity.

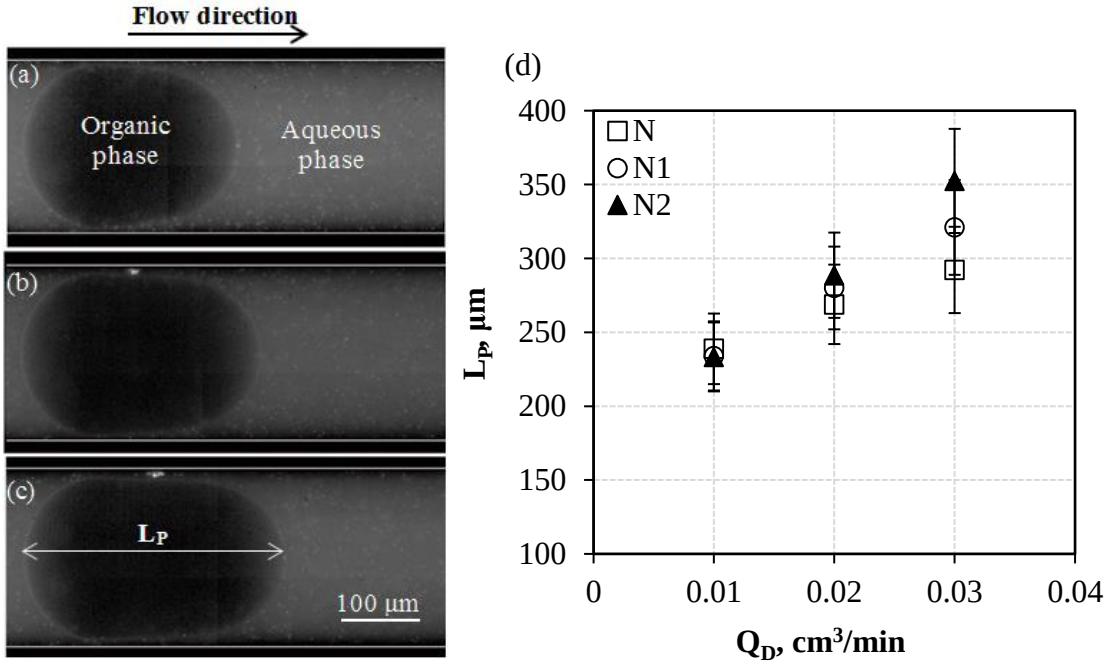

Figure 5.1: Effectof Q_D (cm^3/min) (a) 0.01 (b) 0.02 (c) 0.03 (for Q_C = 0.07 cm^3/min) on the Newtonian plug size (d) Effect of dispersed phase flowarte on plug length (for constant Q_C = 0.07 cm^3/min).

From the pictures captured using the two-colour PIV (Figure 5.1a, b, c) it can be seen that by increasing the dispersed phase flowrate the plug length increases. A similar trend is also found for both non-Newtonian 1000 ppm (N1) and 2000 ppm (N2) solutions. Plug lengths were averaged over 200 micro-PIV images with standard deviation for all cases equal to 3.0-15.5%. The results are plotted in Figure 5.1d where it can be seen that an increase in the xanthan gum concentration produces generally longer oil plugs i.e. $L_{P\,N} < L_{P\,N1} < L_{P\,N2}$, where L_P is the plug length. This difference increases as the dispersed phase flow rate increases.

An increase in the continuous phase flowrate on the other hand, decreases L_P for the non-Newtonian fluids as can be seen in Figure 5.2 for dispersed phase flowrate Q_D = 0.03 cm^3/min. An increase in Q_C from 0.06 cm^3/min to 0.08 cm^3/min reduces the plug length in the N1 and N2 systems by approximately 47 and 55 μm respectively (15% standard deviation). The trend is similar to this of Husny and Cooper-White (2006). Conversely, in the Newtonian system the continuous phase flowrate does not have a significant effect on plug size with maximum deviation of L_P equal to 17 μm (6% standard deviation). Furthermore, as the xanthan gum concetration increases, longer plugs are produced, for constant phase flowrates. The addition of xanthan gum in the aqueous phase increases the viscosity and the viscous shear forces exerted by the continuous phase to the plug as shown in Figure 4.3 (Section 4.2). As a result, the neck break-up location in the non-Newtonian solutions is shifted further downstream from the inlet forming longer filaments and eventually longer plugs compared to the Newtonian case.

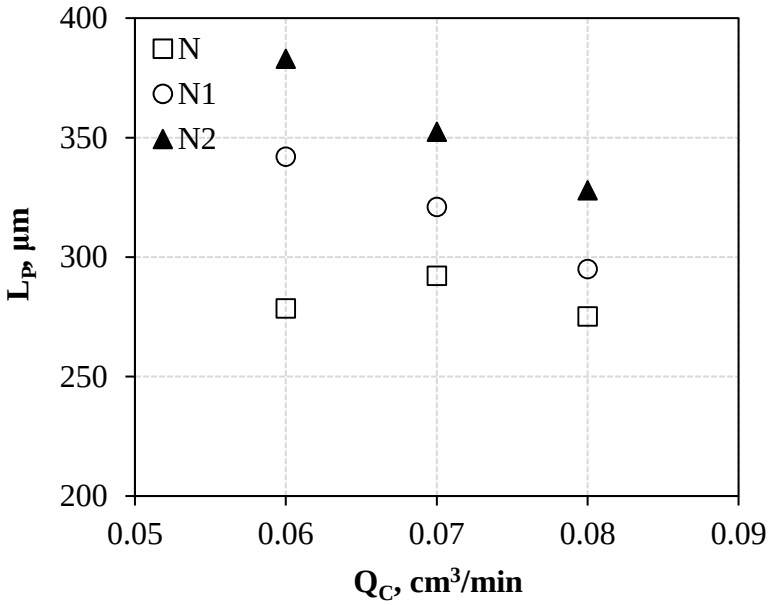

Figure 5.2: Effect of continuous phase flowarte on plug length L_P (for constant Q_D = 0.03 cm^3/min).

Chiarello et al. (2015) who studied the formation of organic droplets in a T-junction channel using different concentrations of xanthan gum (800 ppm, 1500 ppm and 2500 ppm xanthan gum) in water, investigated the shear-thinning effect on the droplet size. They fabricated PDMS T-junction channels with width w = 120 μm and height h = 90 μm and the flowrate ratio φ = Q_D/Q_C was varied from 0.1 to 0.8. They also compared a xanthan gum/water solution to a glycerol/water (Newtonian) one with similar viscosity (60% glycerol and 40% water solution) and found that the droplet lengths produced in the polymeric mixtures were longer than those obtained in the Newtonian one especially at high flow rate ratio (under constant continuous phase flowrate). In addition, for similar Ca numbers (Ca = $11 \cdot 10^{-3}$) and similar Newtonian continuous phase (60% glycerol and 40% water), the plug lengths in the work of Chiarello et al. (2015) are: 210 (Q_D/Q_C = 0.10), 252 (Q_D/Q_C = 0.30) and 300 (Q_D/Q_C = 0.50) μm and similar to the findings of this thesis (238 μm (Q_D/Q_C = 0.14), 268 μm (Q_D/Q_C = 0.28) and 292 μm (Q_D/Q_C = 0.42), Figure 5.1d). Fu et al. (2016) who studied oil drops in shear-thinning aqueous solutions with PAAm also found longer plugs in the non-Newtonian solutions compared to the Newtonian ones. The longer plug lengths however, may not necessarily mean that the plugs have larger volumes. From the PIV images collected it was found that the plug volumes actually decreased with increasing amount of polymer added in the aqueous phase; this is because the thickness of the film surrounding the plugs increased. Chiarello et al. (2017) have also reported this trend with the addition of xanthan gum.

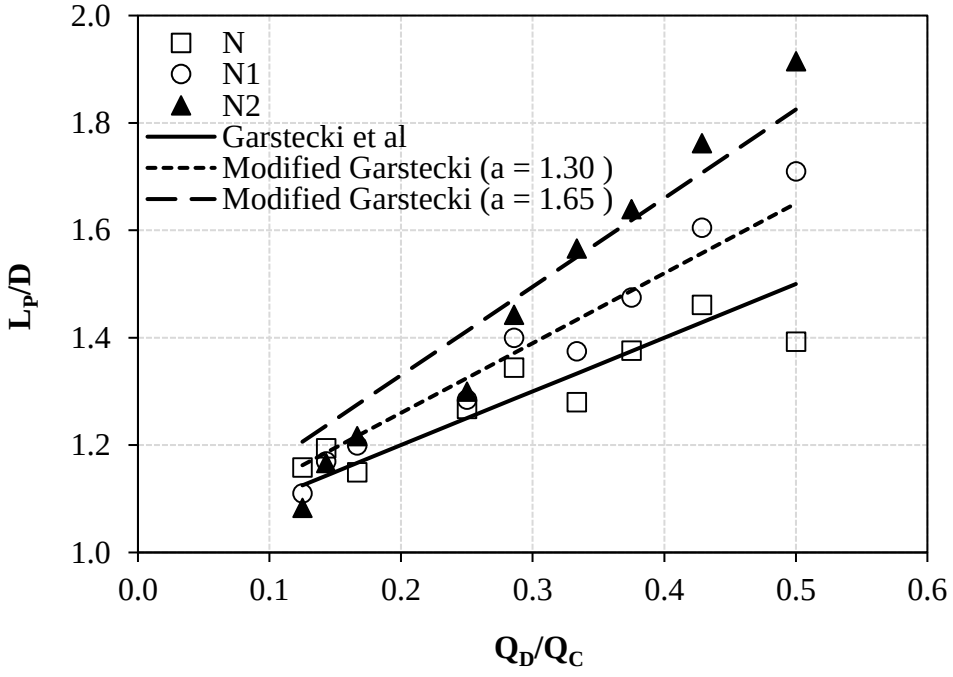

Figure 5.3: Effect of dispersed to continuous phase flowrate ratio on dimensionless plug length L_p/D.

The non-dimensional plug lengths are plotted in Figure 5.3 against the ratio of dispersed to continuous phase flowrates for all conditions studied. As can be seen the dimensionless plug length increases almost linearly with the flowrate ratio (Garstecki et al., 2006). Generally, plug lengths in the non-Newtonian systems are larger than in the Newtonian one and increase with the xanthan gum concentration. In addition, at high flowrate ratio the increase of plug length with the polymer concentration becomes more significant (see also Figure 5.1) i.e. for Q_D/Q_C = 0.5 the L_P of the 2000 ppm solution increases by 32% from the Newtonian case. The results are also compared with the scaling law for the squeezing regime proposed by Garstecki et al. (2006) as presented in Equation 2.3 $\left(\frac{L}{D} = \alpha + \beta \cdot \frac{Q_D}{Q_C}\right)$. For the Newtonian system, the model agrees well with the experimental data for α = 1 with standard deviation less than 8%. For the non-Newtonian systems the values of the parameter α that gave the best fit to the experimental data are 1.30 (4.5% maximum error) and 1.65 (10% maximum error) for the 1000 ppm and 2000 ppm xanthan gum solution respectively. It appears that the addition of polymer does not affect the linear trend and consequently the plug formation mechanism. However, the increase in the slope for different xanthan gum concentrations indicates a geometrical modification of plugs (see Section 4.3) as they form at the T-junction inlet. On top of that, the comparison between this work and the one of Garstecki et al. (2006), shows that by adding xanthan gum in the aqueous phase, the plug characteristics can be tuned and longer plugs can be produced at lower flowrate values.

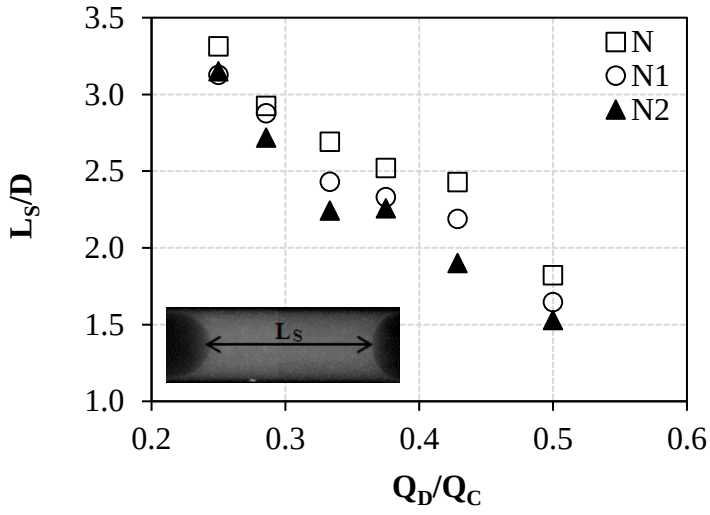

Figure 5.4: Effect of dispersed to continuous phase flowrate ratio on dimensionless slug length L_S/D. Inset: Slug length during plug flow.

The effect of flow rate ratio on the slug length is shown in Figure 5.4. As the dispersed phase flowrate increases the slug length reduces linearly by 45% in all the three aqueous solutions

(standard deviation for all cases equal to 6.5-13.0%). Furthermore, for constant phase flowrates, increasing the xanthan gum concetration results in slightly shorter slugs. It should be noted that for Q_D = 0.01 cm^3/min where the slug is long, a full-length slug image could not be captured with the current configuration of the PIV system and no slug length was measured.

5.2 Plug shape

Figure 5.5 presents the effect of the shear-thinning viscosity of the continuous phase on the curvature of the plug leading edge. The plug leading edge was obtained from the μPIV images and is defined as the area from the tip of the plug until the point where the surrounding film has reached a uniform thickness (Figure 5.5a). The front plug edge curvature increases (tip radius decreases) with increasing polymer concentration in the continuous aqueous phase and the plug acquires a bullet-shaped profile (see also Section 4.3.1).

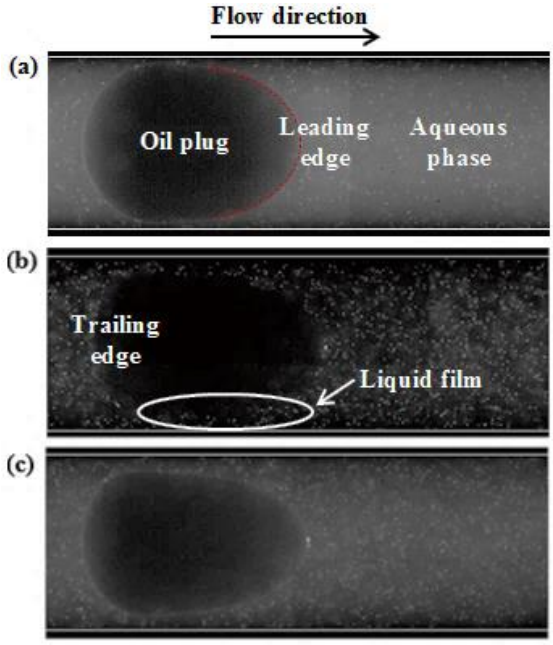

Figure 5.5: Effect of xanthan gum concentration on plug shape (a) Newtonian fluid, N (b) non-Newtonian fluid 1000 ppm, N1 (c) non-Newtonian fluid 2000 ppm, N2 (Q_C = 0.07 cm^3/min and Q_D = 0.01 cm^3/min).

In the 2000 ppm polymer concentration system, the decrease in the plug leading edge radius can be as high as 37% compared to the Newtonian case. The radius of the trailing plug edge also decreases with polymer concentration in the aqueous phase. However, this decrease is less

pronounced compared to the front edge and for the case shown in Figure 5.5 it is about 13%. The same behaviour was observed for all the flow rate combinations studied.

The bullet-shaped profile of the leading plug edge has been reported for Taylor bubbles at high Capillary numbers. In the present study, high Capillary numbers can be achieved by increasing the continuous phase viscosity or the dispersed phase velocity as the interfacial tension is the same for all the three aqueous solutions. The dependency of the plug front edge curvature, R_T, on the Capillary number for the different continuous phases studied is shown in Figure 5.6 for Q_C = 0.07 cm^3/min. The plug radius decreases as the Ca number increases with the polymer addition; this was also seen by Meyer et al. (2014). In the non-Newtonian solutions the viscocity is not homogeneous across the channel. The viscosity is higher in the middle of the channel where the shear rates are low (see also Figure 3.1). As a result, the increased viscous forces in this region overcome the surface tension forces which are not able to sustain the semispherical shape of the plug front, leading to the bullet-shaped profile.

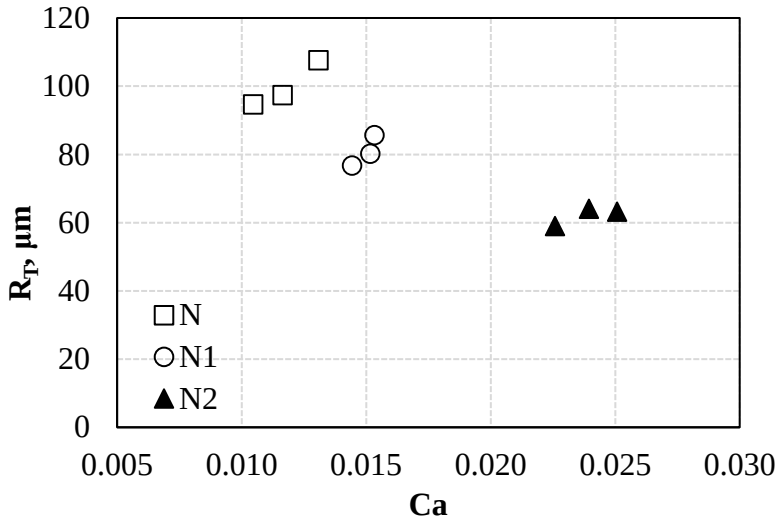

Figure 5.6: Effect of Ca number on plug front edge curvature for constant Q_C = 0.07 cm^3/min and Q_D equal to 0.01, 0.02 and 0.03 cm^3/min.

5.3 Film thickness

In all cases investigated, the plugs are separated from the channel wall by a thin film of the continuous phase as shown in Figure 5.5. The film thickness was measured from the images obtained with the micro-PIV system. As can be seen, the film thickness, δ, is not uniform over the entire length of the plug. According to Bretherton (1961) the plug profile can be divided into three different parts: leading edge, trailing edge and main part. The leading and trailing

edge caps join through a transition region with the main part of the plug with uniform film thickness (see also Figure 2.11). However, when the plugs are not sufficiently long, a uniform film thickness region may not establish.

Figure 5.7 shows the two main plug profiles that were observed depending on the plug length. In short plugs, the leading plug edge joins almost immediately the trailing edge and there is not a region of uniform film thickness (Figure 5.7a, b). As the plug length increases above $L_P \geq 352$ μm, a region of uniform film thickness can be seen (Figure 5.7c). This variation in film thickness can pose problems in its measurement. Eain et al. (2013) has chosen as measurement location the trailing part of the plug where the film thickness has its lowest value. Other investigators (Dore et al., 2012; Jovanovic et al., 2011) have used an average value of the film thickness along the plug, between the leading and trailing edges. This approach was also used here and an average film thickness was calculated. For low Capillary numbers Ca ~ 10^{-3} (Newtonian case), where the dimensionless film thickness is δ ~ 8 μm, the standard deviation in the film thickness measurements could be as high as 20%. At high Capillary numbers, which correspond to the non-Newtonian solutions, the standard deviation in the film thickness measurements is below 10% for all the cases studied.

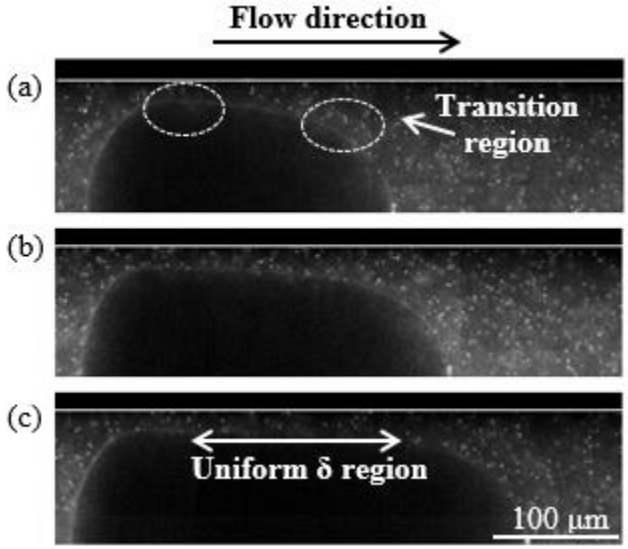

Figure 5.7: Effect of plug length on film thickness for N2 and Q_D (cm^3/min): (a) 0.01 (b) 0.02 (c) 0.03 (for constant Q_C = 0.07 cm^3/min).

The effect of the continuous phase flowrate and rheology on film thickness can be seen in Figure 5.8. With increasing amount of xanthan gum in the aqueous phase and increasing front plug edge curvature, the film thickness increases. At the Newtonian system, the liquid film corresponds to approximately 3% of the channel diameter whereas at the 2000 ppm xanthan

gum (N2) system the film thickness is almost 10% of the channel diameter. Additionally, for a constant continuous phase flowrate, Q_C = 0.07 cm^3/min, the film thickness increases with increasing dispersed phase flowrate. As reported in the literature, in Newtonian systems the film thickness is increased either by increasing the velocity or the viscosity of the continuous phase, which lead to increased Ca number (Tsaoulidis and Angeli, 2016). However, for these Newtonian cases the maximum increase of the film thickness is by a factor of 2 (even at higher Ca number i.e. 0.003 < Ca < 0.180) while for the shear-thinning fluids used here the increase is by a factor of 4 (0.007 < Ca < 0.027).

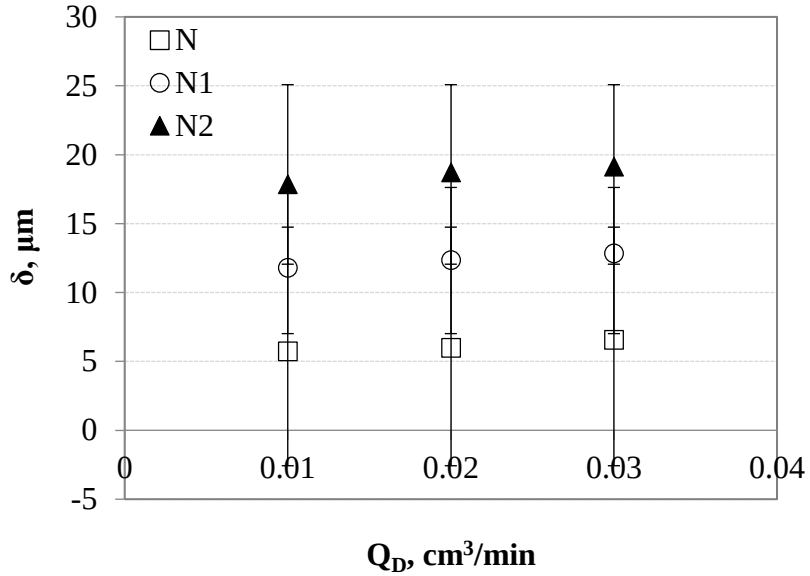

Figure 5.8: Effect of dispersed phase flow rate on film thickness for all aqueous solutions (constant Q_C = 0.07 cm^3/min).

The experimental non-dimensional film thickness results, δ/R_C, for all conditions studied, are plotted in Figure 5.9 against the Capillary number $Ca = \frac{\mu_C \cdot U_P}{\sigma}$ (Equation 3.1). From the different velocities that have been used in the literature for the calculation of the Capillary number (e.g. plug, continuous phase and mixture velocity) (Dessimoz et al., 2008; Tsaoulidis and Angeli, 2016) the plug velocity was chosen because it is related to the film thickness (Eain et al., 2013). The dimensionless film thickness was found to increase with increasing Capillary number. The results are also compared against the predictions of commonly used models given in

Table 2.4 (in Section 2.1.4). Many of the literature correlations for film thickness, shown in Figure 5.9, are developments of the theoretical analysis by Bretherton (1961) who found that the film thickness in gas-liquid bubble flow was proportional to $Ca^{2/3}$. The data for the

Newtonian system agreed well with the model by Aussillous and Quere (2000), with an average error of 7%, who modified Bretherton's correlation to fit the experimental data by Taylor (1961). At Ca < 0.015 the results also agreed well with the model by Bretherton (1961) with an average error of 9%. These models however, did not predict well the experimental results for the non-Newtonian systems (average error > 54%). Irandoust and Anderson (1989) proposed an empirical correlation for film thickness in gas-liquid Taylor flow, which predicted the present results in both Newtonian and non-Newtonian systems with an average error of 33%. The model by Dore et al. (2012) predicted reasonably well the experimental data for the non-Newtonian system (11% average error) but not for the Newtonian ones, with average error of about 56%. The model by Eain et al. (2013) which included the effects of inertial forces via the Weber number, did not predict the non-Newtonian data well with an average error of 90% whereas for the Newtonian mixtures the average error was 24%.

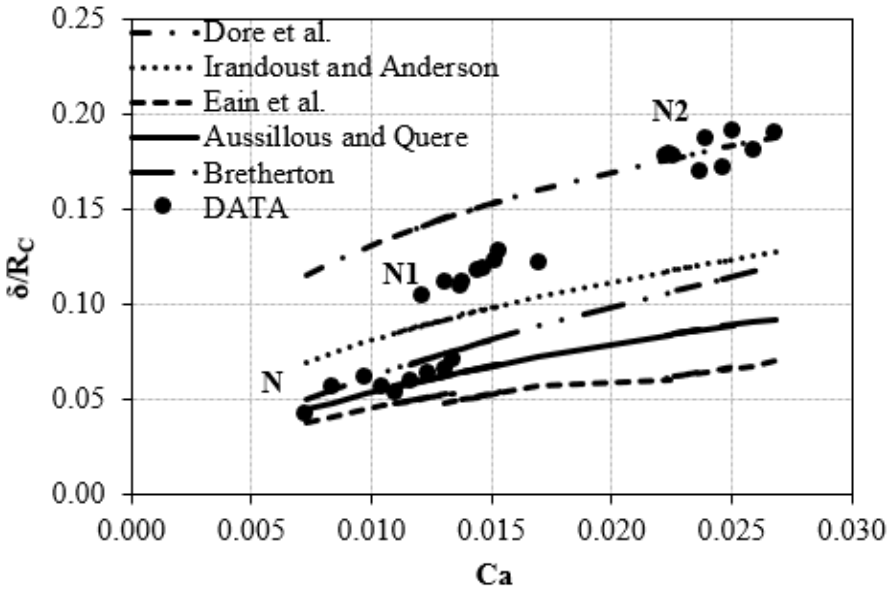

Figure 5.9: Non-dimensional film thickness plotted against Capillary number for all experimental conditions. Current results are compared to literature models from

Table 2.4.

5.4 Circulation patterns in the plugs and the slugs

Representative average velocity fields in both organic and aqeous phases, obtained with the two-colour μ-PIV system, are shown in Figure 5.10. The horizontal component of the velocity is dominant at the main flow direction along the x-axis. The velocity is maximum at the core

of both the plug and the slug and decreases towards the channel walls and the liquid/liquid interface. The horizontal velocity profiles at the middle of the plug and slug, (dotted rectangle in Figure 5.10a) for two extreme cases (Newtonian, N and 2000 ppm xanthan gum, N2) are compared in Figure 5.11a and b respectively for Q_C = 0.07 cm^3/min and Q_D = 0.03 cm^3/min. Within the plug, the velocities are slightly larger for the non-Newtonian system compared to the Newtonian one (Figure 5.11b). This is expected since the addition of the polymer resulted in a bullet-shaped plug and increased film thickness, which led to a higher plug velocity. As can be seen in Figure 5.11a the velocity profile in the slug changes shape with the addition of the polymer. For the Newtonian system, fully developed laminar flow is expected in the middle of the slug, and this is reflected in the parabolic profile. However, in the non-Newtonian system the profile is flat in the middle, which is characteristic of the laminar velocity profile of a power law fluid.

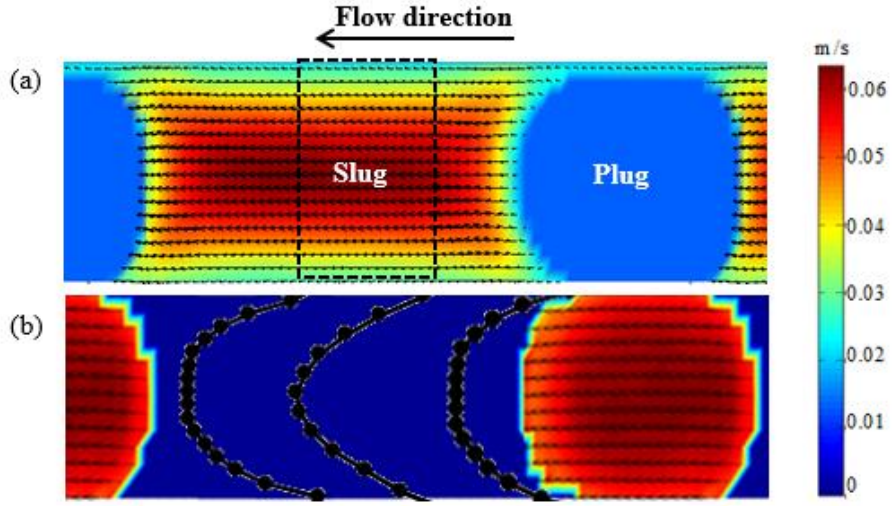

Figure 5.10: Averaged total velocity fields in (a) slug (b) plug for Newtonian fluid N and flowrates Q_C = 0.07 cm^3/min and Q_D = 0.03 cm^3/min. Dotted rectangle indicates the fully developed laminar flow area.

The non-homogeneous shear rate and viscosity profiles in the slug were also calculated based on the PIV velocity profiles and are presented in Figure 5.12 for the 2000 ppm non-Newtonian solution. As can be seen, the shear rate varies from 1000 s^{-1} (close to channel wall) to almost zero (in the middle area of the channel) resulting in an increase in the viscosity of the xanthan gum solutions by one order of magnitude, i.e. from 0.02 Pa s in the wall (1000 s^{-1}, μ_{Disp}/μ_{Cont} = 4.34) to 0.2 Pa s in the middle (0-3 s^{-1}, μ_{Disp}/μ_{Cont} = 43.47). These values correspond to the shear-thinning region of the solution (see Figure 3.1). Figure 5.12 clearly shows that the hydrodynamic characteristics of the plugs formed in shear-thinning xanthan solutions are a result of both shear-thinning behaviour and increased viscosity.

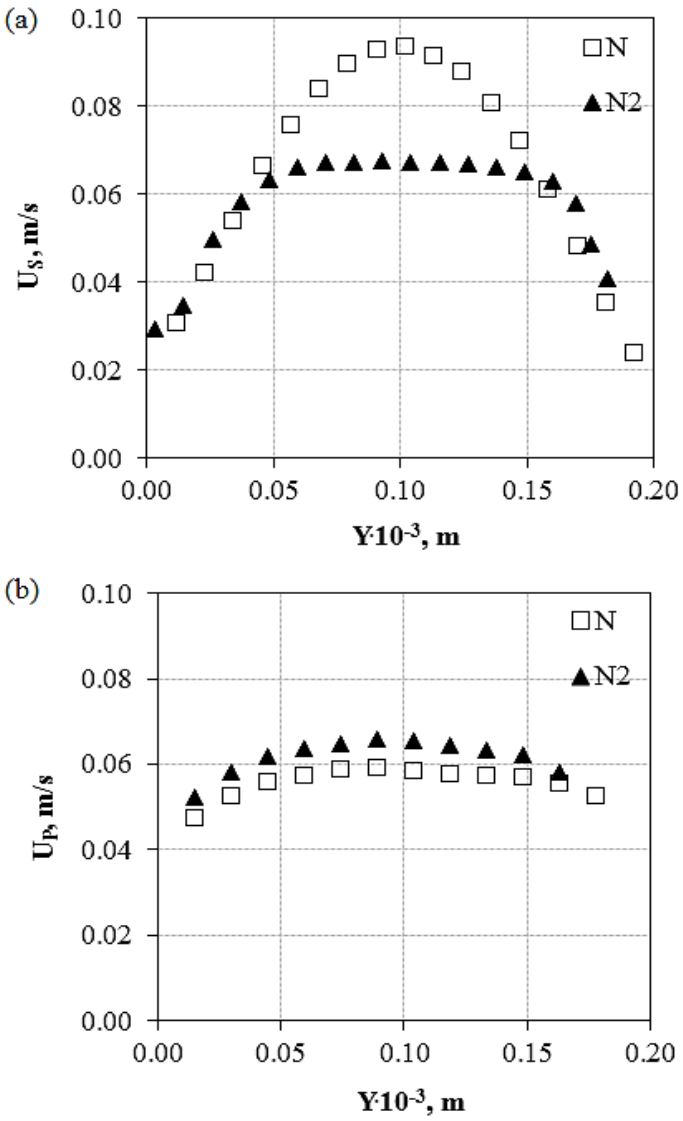

Figure 5.11:Average velocity profiles of the horizontal component of the velocity in the middle of (a) the slug and (b) the plug for different concentrations of xanthan gum (Q_C = 0.07 cm^3/min and Q_D = 0.03 cm^3/min).

The change in the velocity profiles, particularly in the slug, when polymer is added is expected to affect the circulation patterns. The recirculation patterns in the slug were calculated by subtracting the slug velocity from the averaged local velocity field and are shown in Figure 5.13 for continuous flow rate Q_C = 0.07 cm^3/min and dispersed flow rate Q_D = 0.03 cm^3/min. As shown in Figure 5.13a, for the Newtonian aqueous phase a clear recirculation pattern forms which consists of two distinct vortices, counter rotating and symmetrical about the channel axis. The recirculation pattern is also symmetric with respect to the centreline of the slug and extends along the whole slug length. Two stagnation zones are visible and the backflow of the particles is pronounced. When the 2000 ppm xanthan gum solution is used as continuous phase,

the two stagnation zones move towards the channel wall, while they remain symmetric about the channel axis (Figure 5.13b) resulting in a less intense recirculation pattern.

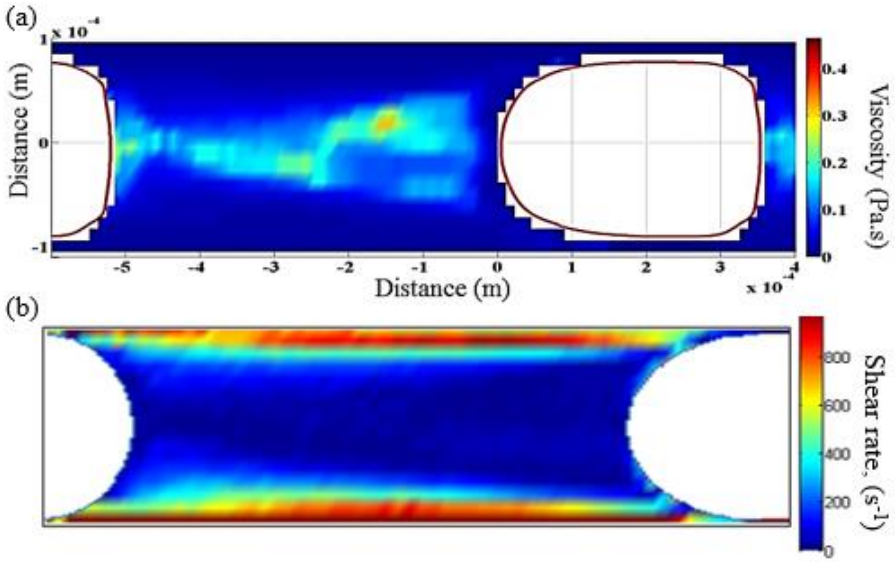

Figure 5.12: a) Viscosity profile (b) Shear rate profile in the aqueous non-Newtonian 2000 ppm (N2) slug (Q_C = 0.07 cm^3/min and Q_D = 0.03 cm^3/min).

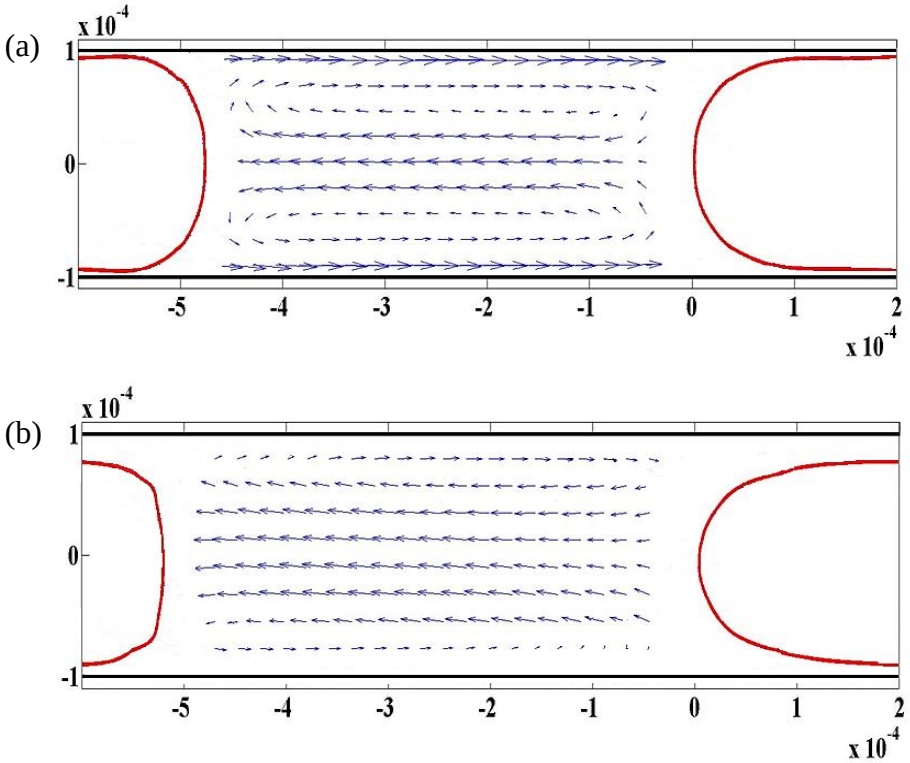

Figure 5.13: Effect of xanthan gum concentration on circulation patterns in aqueous slugs for (a) Newtonian fluid, N (b) Non-Newtonian 2000 ppm fluid, N2 (Q_C = 0.07 cm^3/min and Q_D = 0.03 cm^3/min).

The circulation within the slugs can be quantified with the dimensionless circulation time, which can be calculated from the current velocity profiles obtained from PIV on a plane in the middle of the slug as follows (Equation 2.10):

$$\tau_{cir} = \frac{L_S y_0}{\int_0^{y_0} u(x,y) d_y} \frac{U_S}{L_S} = \frac{U_S y_0}{\Delta y \sum_{i=1}^{i=N} v_i} \qquad \text{(Equation 5.1)}$$

where y_o is the location of the stagnation point projected onto the observation plane, U_S is the slug velocity. The dimensionless circulation time from Equation 5.1 is plotted against the slug length in Figure 5.14. As can be seen the circulation time is almost uniform in the main part of the slug body (which corresponds to the maximum velocity of the slug, see Figure 5.10) indicating that the circulation patterns are regular and increases close to the front and back interfaces.

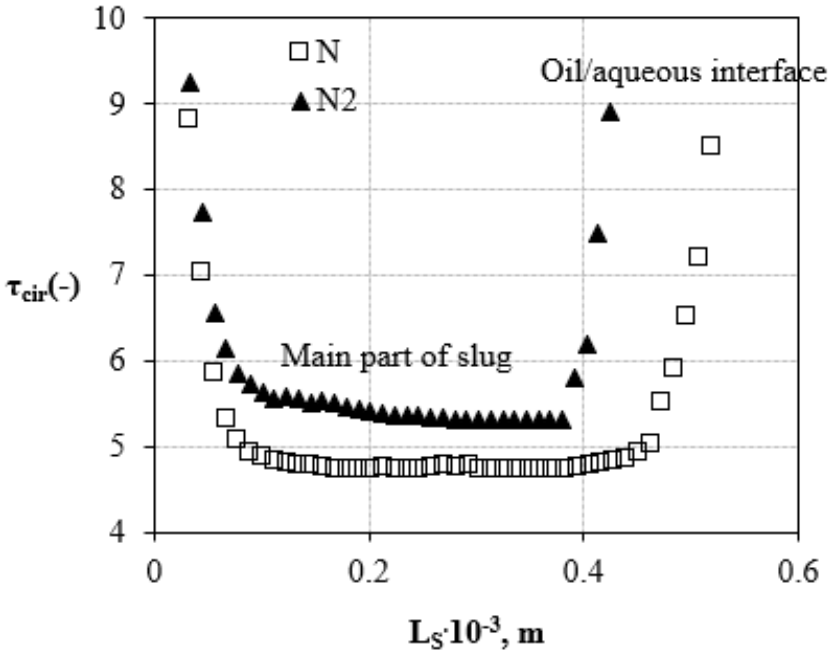

Figure 5.14: Effect of xanthan gum concentration on the dimensionless circulation time in the slug for flowrates Q_C = 0.07 cm^3/min and Q_D = 0.03 cm^3/min.

Similar findings were found by Dore et al. (2012) who studied circulation patterns inside aqueous plugs flowing in ionic continuous phase liquids in a similar T-junction channel to the one used in the present study. When the xanthan gum solution is used, the circulation time increases slightly under the same flowrate conditions. The average dimensionless circulation time corresponding to the plateau of the curve is equal to 4.76 and 5.44 for the Newtonian and non-Newtonian systems respectively. Similar trends were found for all the flowrates studied as can be seen in Table 5.1. As was mentioned before, when Q_D = 0.01 cm^3/min, a full-length slug

image could not be captured with the current PIV system and no circulation patterns could be calculated for these cases.

Table 5.1: Dimensionless circulation times in the continuous aqueous slug phase.

Experimental conditions		**Dimensionless circulation time**		
Q_C, cm^3/min	**Q_D, cm^3/min**	N	N1	N2
0.06	0.01	-	-	-
	0.02	2.95	3.83	4.35
	0.03	3.28	4.38	4.57
0.07	0.01	-	-	-
	0.02	4.01	4.41	4.95
	0.03	4.76	5.02	5.44
0.08	0.01	-	-	-
	0.02	5.17	5.75	6.31
	0.03	6.49	6.91	7.23

5.5 Overview and main conclusions

The plug flow of a non-Newtonian and a Newtonian liquid in the T-junction microchannel were investigated using the two-colour micro-PIV system. Two glycerol aqueous solutions containing different concentrations of a shear-thinning polymer, xanthan gum (1000 and 2000 ppm) were used as the non-Newtonian phase while silicone oil was the Newtonian one forming the dispersed plugs under all conditions.

It was found that plug lengths increased when polymer was added, while in all cases their size increased when the dispersed to continuous phase flowrate ratio increased. The front plug edge curvature increased with polymer concentration and the plug acquired a bullet-shaped profile. The thickness of the aqueous film between the plug and the channel wall increased with increasing concentration of the polymer in the continuous phase; it also increased with the dispersed phase velocity. Using a modified Capillary number to account for the non-Newtonian continuous phase viscosity, the suggested models were not able to predict both Newtonian and non-Newtonian film thickness data satisfactory. Good agreement was found between the non-Newtonian data and the film thickness models by Irandoust and Anderson (1989) and Dore et al. (2012) for $0.012 < Ca < 0.027$.

The velocity profiles obrtained from the PIV measurements showed that the addition of xanthan gum resulted in higher plug velocity. Within the non-Newtonian slug, the velocity profiles were found to be flat in the middle of the channel as expected for a power law fluid.

Higher viscosities were also found in this region compared to the region close to the channel wall. The addition of the polymer also changed the circulation patterns in the aqueous continuous phase. Compared to the Newtonian cases, in the non-Newtonian slugs the stagnation points moved towards the channel wall while the dimensionless circulation times increased, indicating less intense mixing.

6. Chapter: Droplet formation in a flow-focusing microchannel in the presence of surfactants

The formation of an aqueous droplet in an organic continuous phase was studied experimentally inside a flow-focusing microchannel in the presence of surfactants. The drop formation process and the velocity profiles in both phases in the squeezing and dripping regimes were studied in detail using the two-colour Particle Image Velocimetry technique. A mechanistic model was also developed, based on the hydrodynamic data, to describe the evolution of the forces acting at the drop at the various formation stages.

6.1 Flow pattern map

A low viscosity silicone oil (0.0046 Pa s) was used as the continuous phase and a mixture of 48% w/w water and 52% w/w glycerol was the dispersed phase. Two ionic surfactants, C_{12}TAB (50 mM) and C_{16}TAB (5 mM) were added in the aqueous phase, at concentrations above the CMC values (see also Section 3.1.2). The flow experiments were conducted in a glass flow-focusing device with cross-junction equal to 190 μm x 195 μm (depth x width) and channels equal to 190 μm x 390 μm (Dolomite® microfluidics). For each set of runs, the aqueous phase flow rate was kept constant and the organic phase flowrate was increased stepwise. The aqueous phase flow rates ranged from 0.01 to 0.1 cm^3/min, whereas the organic phase flow rates varied from 0.003 to 0.1 cm^3/min (for more details Section 3.2.2). Under these experimental conditions, different flow regimes namely squeezing, dripping, jetting and threading were observed in the cross-junction device. Figure 6.1 presents the flow pattern map for the surfactant-free solution based on the volumetric flow rate of each phase, together with representative images of the corresponding patterns. The flow pattern map is in good agreement with the results obtained by Kovalchuk et al. (2018) in a similar system, which confirms that the added tracers and dye do not affect the flows. In the literature, Ca numbers are often used to represent the droplet formation regimes. In the current study the Ca numbers of the continuous $Ca_C = \frac{\mu_C \cdot Q_C}{\sigma \cdot A}$ and dispersed phase $Ca_D = \frac{\mu_D \cdot Q_D}{\sigma \cdot A}$ vary only with the flowrates of fluids and the interfacial tension (μ_C, Q_C and μ_D, Q_D are the viscosities and flowrates of the continuous and dispersed phase respectively and A is the cross-sectional area of the channel). The dynamic interfacial tension values are not known, while, as will be discussed below the

dynamic phenomena only affect the very first stages of drop formation while at the later stages equilibrium values establish. If equilibrium interfacial tension values are used then Ca number for each surfactant solution depends only on the phase flowrates and these are used in Figure 6.1. By using this representation, the differences between the various systems are also shown more clearly.

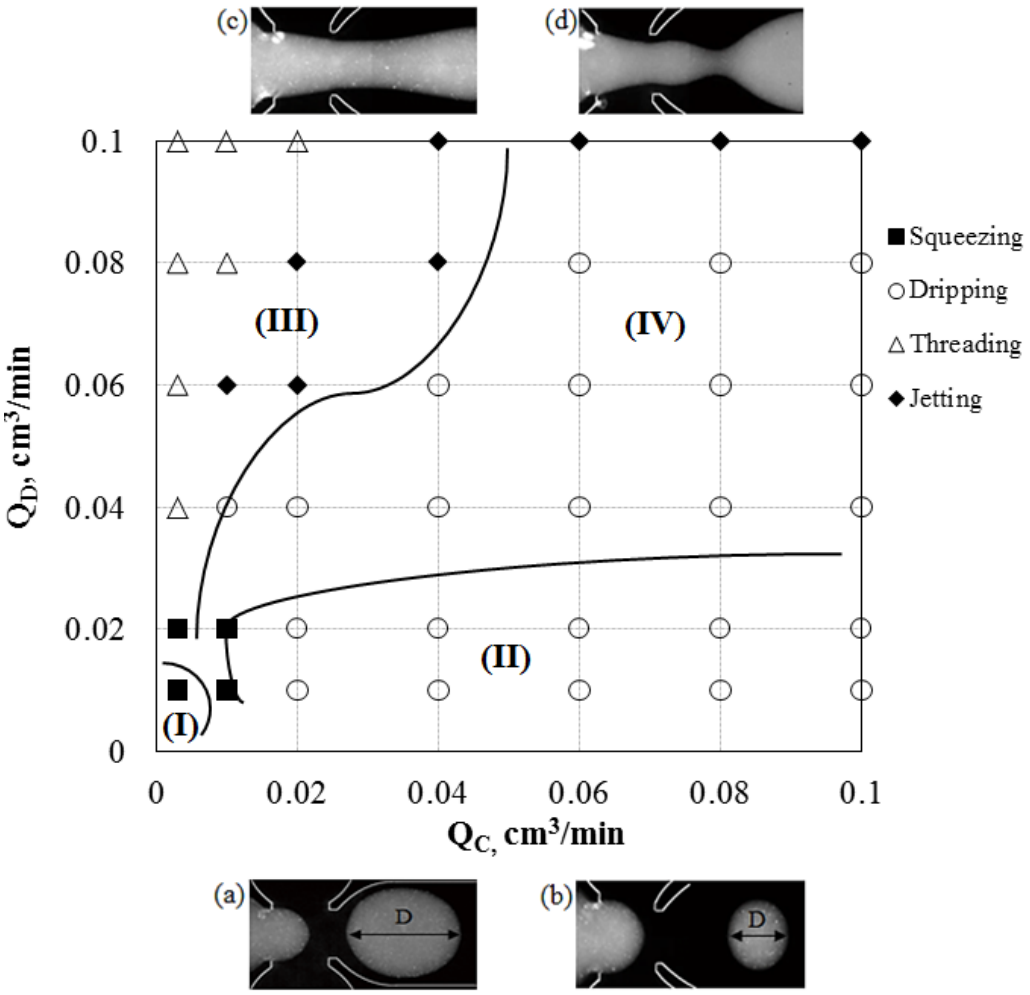

Figure 6.1:Flow pattern map of the surfactant-free solution and the C_{12}TAB solution and the silicone oil. The lines show the flow regime boundaries when the C_{12}TAB solution is used: (I) Squeezing regime (II) Dripping regime (III) Threading regime and (IV) Jetting regime. The representative flow patterns are: (a) plug flow (squeezing regime) (b) drop flow (dripping regime) (c) thread flow (threading regime) (d) jet flow (jetting regime). D is the droplet size immediately after the break-up inside the cross-junction inlet.

The squeezing regime (■), occurred at low flow rates 0.01 cm^3/min < Q_D < 0.02 cm^3/min and 0.003 cm^3/min < Q_C < 0.01 cm^3/min. In this regime, the breakup of the plug (Figure 6.1a)

is dominated by the excessive pressure that builds up in the continuous phase during the plug formation. As the plug is forming, it obstructs the cross-junction and restricts the flow of the continuous phase to a thin film on the channel walls. As a result, the pressure inside the continuous phase increases and 'squeezes' the plug neck (Garstecki et al., 2006). The length of the plugs was found to be greater than the main channel width ($L_P > 390$ μm), while a thin film of the continuous phase separated the plugs from the channel wall.

As the continuous phase flowrate increased, under constant Q_D, the dripping regime (○) dominates inside the microchannel. In the dripping flow pattern (Figure 6.1b), the drop formation process is controlled by the balance of viscous shear and interfacial forces (Wang et al., 2009). The forming drops do not obstruct completely the flow of the incoming continuous phase and their lengths are smaller ($L < 390$ μm) than the main channel width. At low continuous phase flowrates (0.003 cm^3/min$< Q_C < 0.01$ cm^3/min), as the dispersed phase flowrate increases, there is a transition from the squeezing to the threading (△) regime. In the threading regime, a stable thread of the dispersed phase (Figure 6.1c) is produced in the flow-focusing inlet. The thread width was found to increase with increasing dispersed phase flow rate (for constant Q_C). An increase of the continuous phase flowrate results in a transition from the threading to the jetting regime (♦). In this regime, the dispersed phase is mainly driven by the shear force from the continuous phase flow that pulls it downstream and the jet becomes destabilized (Figure 6.1d). Utada et al. (2007) who studied the transition from the dripping to the jetting regime in co-flowing liquids, noticed that at large dispersed phase flowrates, the inertia force of the dispersed phase becomes comparable and acts cooperatively with the force from the continuous phase, shifting the pinch-off point of the drop further downstream into the main channel. Kovalchuk et al. (2018) found a similar shift of the pinch-off point with increasing dispersed to continuous phase flowrate ratio and noted that the length of the jet also depended on the interfacial tension i.e. the jet length increases with decreasing interfacial tension.

When the 50 mM C_{12}TAB solution was used, the boundaries shifted as shown in Figure 6.1 with lines. In particular, the squeezing regime and consequently plug flow was observed only in area (I) limited to low flow rates of both phases. The dripping regime was also reduced in the map in area (II) and drops were produced at low dispersed phase flowrates only (0.01 cm^3/min $< Q_D < 0.02$ cm^3/min). However, the areas occupied by the threading and jetting regimes in the map increased. The thread flow pattern occurred for an extended range of continuous phase flowrates, 0.003 cm^3/min $< Q_C < 0.05$ cm^3/min and for most of the dispersed phase flowrates (map area (III)). The jetting regime covered a large area in the map (area (IV)).

The boundaries between regimes for the 5 mM C_{16}TAB solution, which is less concentrated than the C_{12}TAB, were in between those of the surfactant-free and of the C_{12}TAB solutions. The shift in the boundaries between the regimes reveals the effect of the surfactant concentration on the drop formation process.

6.2 Droplet formation process

Droplet devices usually operate in the squeezing and dripping regimes where monodisperse droplets are generated (Xu et al., 2008). The mechanism of droplet generation in the squeezing and dripping regimes is further studied with the two-colour PIV system in the channel cross-junction.

Figure 6.2 shows a typical plug formation process in the squeezing regime, which is based on the pressure-driven mechanism proposed by Garstecki et al. (2006). The plug formation process in the flow-focusing inlet is divided into 3 stages: expansion (Figure 6.2a and b), necking (Figure 6.2c and d) and pinch-off (Figure 6.2e) (similar to Section 4.2). The images have been obtained with the two-colour PIV system and the channel walls have been added for clarity. At the first expansion stage, the dispersed phase is expanding into the main channel. Immediately after the pinch-off of the previous plug, the dispersed phase pulls back slightly into the dispersed phase channel inlet due to surface tension before it moves forward again into the main channel. At this initial stage, the plug grows mainly in the radial direction and slightly in the axial direction in the junction (Figure 6.2a). Under constant dispersed phase flowrate, the interface starts to expand in the axial direction towards the main channel. The plug reaches the edge of the main channel but it is still separated from the wall by a thin film of the continuous phase (Figure 6.2b). At this stage, the plug blocks the side inlet channels of the continuous phase, and the pressure there increases. The increased pressure overcomes the interfacial tension force and causes a change in the interface curvature and the thinning of the neck (Figure 6.2c). As neck is defined the part of the fluid that connects the dispersed phase with the forming plug. The change in curvature signifies the beginning of the necking stage (Figure 6.2c – d) where the neck width decreases as the dispersed phase propagates into the main channel. During the necking stage, the flow of the continuous phase reduces the neck width in the radial direction and pushes the plug in the axial direction. The transition between the necking and the pinch-off stage was found to take place at neck widths of about 60-70 μm (depending on the continuous phase flowrate). At these neck widths a flow reversal was

observed at the lower part of the plug (as was revealed by the PIV results) which was used as a criterion of the transition. In addition, at this neck width the velocities near the top part of the plug increase compared to those at the expansion and necking stages. After the break-up, the new plug is pushed downstream in the main channel by the continuous phase and the formation process starts again.

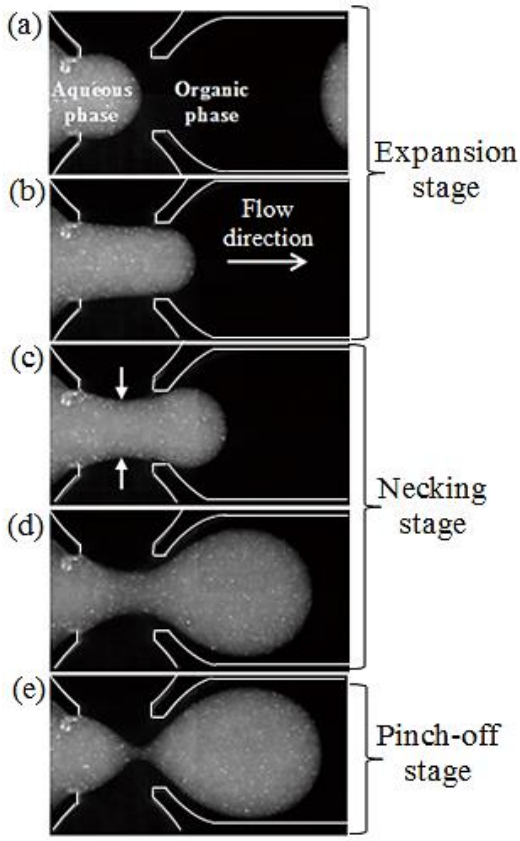

Figure 6.2 Typical plug formation in the flow-focusing geometry: (a) - (b) expansion stage, (c) – (d) necking stage, (e) pinch-off stage (for $Q_D = Q_C = 0.01$ cm^3/min).

The same three stages of formation (expansion, necking, pinch-off stage) were also identified for the dripping regime. During the expansion stage, the interfacial tension force that acts on the forming drop initially dominates and controls the expansion rate. As the droplet grows into the main channel, the shear stress inside the continuous phase increases and exceeds the interfacial tension force, thinning the neck (necking stage). In addition, the pressure inside the continuous phase increases, because its flow is restricted by the droplet. The pressure that builds up in the continuous phase is less in the dripping than in the squeezing regime as the growing droplet has smaller size and blocks less the area of the side channels (Figure 6.2a and b). The neck of the dispersed phase eventually breaks (pinch-off stage) and a new droplet is formed.

6.3 Droplet characteristics: neck width and front radius of a forming drop

The thinning rate of the neck is mainly dependent on the continuous phase flowrate (Fu et al., 2009). The neck width was measured at both the expansion and the necking stages, to examine which formation stage determines the droplet size. Figure 6.3 shows the effect of the continuous phase flowrate (Q_C = 0.003 – 0.1 cm^3/min) on the neck width, W_N, at the expansion stage just before the next, necking stage (Figure 6.3, Inset). For a constant dispersed phase flowrate (Q_D = 0.01 cm^3/min) and low continuous phase flowrate (Q_C = 0.003 cm^3/min) the surfactant-laden solutions give similar neck width. However, with increasing Q_C, the differences in the width between the surfactant-laden solutions are becoming more pronounced. This is attributed to the differences in absorption kinetics of the two surfactants during drop formation (Baret et al., 2009; Jin et al., 2006). C_{16}TAB appears to be reaching equilibrium at a lower rate compared to C_{12}TAB. When the continuous phase flowrates are high (Q_C > 0.02 cm^3/min) the expansion stage is very short (in the time scale of 0.004 s – 0.02 s, depending on the continuous phase flowrate, as found by the measurements) and the concentration of C_{16}TAB does not manage to reach equilibrium at the interface.

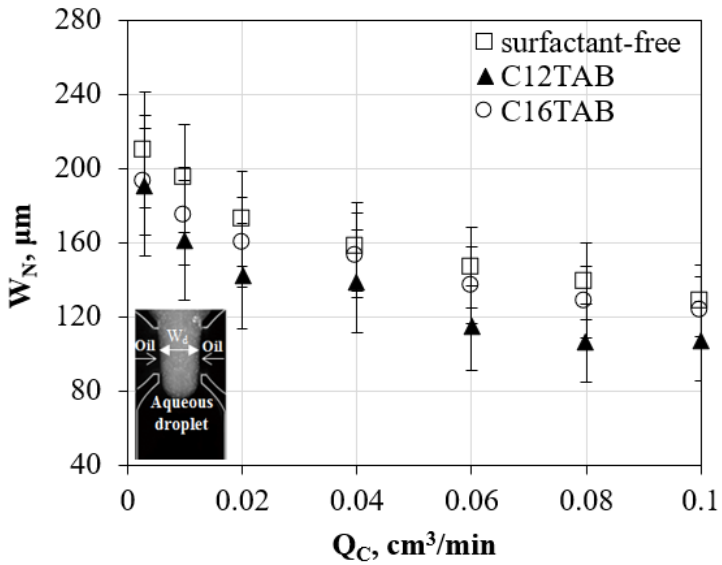

Figure 6.3: Effect of the continuous phase flowrate on the neck width at the end of expansion stage. Q_D = 0.01 cm^3/min. Inset: Neck width at the end of expansion stage.

The results (neck width) then are similar to the surfactant free system (Figure 6.3). This is not the case for C_{12}TAB, which absorbs faster and has time to reach equilibrium. In contrast, at

low flowrates ($Q_C \leq 0.02$ cm^3/min), the expansion stage takes longer (in the time scales of 0.05 – 0.09 s) and the concentration of C_{16}TAB at the interface reaches a value closer to the equilibrium one. The results on neck width are in this case similar to C_{12}TAB (Figure 6.3). The same trend was also observed for $Q_D = 0.02$ cm^3/min.

Different trends were observed in the necking stage, as can be seen in Figure 6.4, where the neck width is plotted against the continuous phase flowrate. The data represent the minimum neck width that can be measured at the end of the necking stage. The necking stage takes longer (time scales of necking stage: 0.13 s - 0.58 s based on the continuous phase flowrate) and even C_{16}TAB has time to reach the equilibrium concentration at the interface. The equilibrium interfacial tension of C_{16}TAB is similar to C_{12}TAB at the concentrations used, and as a result, the neck widths from the two surfactants are similar at the necking stage (Figure 6.4).

The final drop sizes obtained for all fluid systems are shown in Figure 6.5 for constant $Q_D = 0.01$ cm^3/min. As can be seen, the two surfactant systems give similar final drop sizes (maximum deviation 8%), which are smaller than those obtained in the pure system by ~ 100 μm. The data shown in Figure 6.5 correspond to the axial drop diameter, D_D, measured immediately after the droplet formation at the cross-junction inlet (see Inset, Figure 6.5).

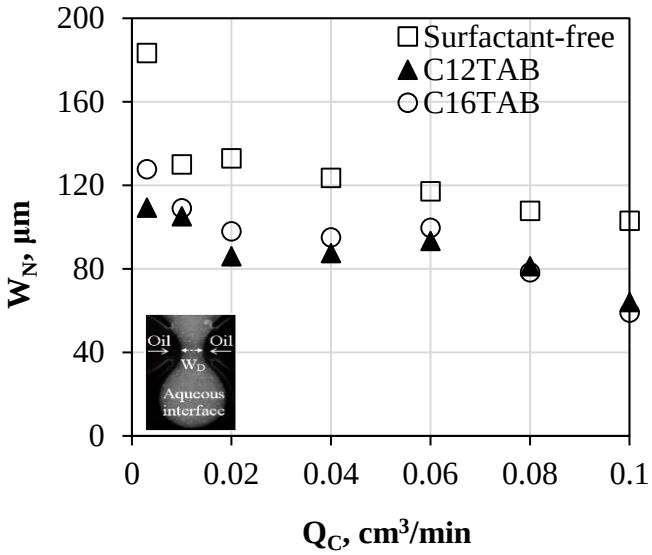

Figure 6.4: Effect of the continuous phase flowrate on the minimum neck width for all the aqueous solutions used at the necking stage. $Q_D = 0.01$ cm^3/min. Inset: Neck width at the necking stage.

Figure 6.4 and Figure 6.5 demonstrate that the necking stage affects the final drop size more than the expansion stage. The dependence of the final droplet size on the necking stage has also been reported by Chen et al. (2015) and by Glawdel et al. (2012a). From Figure 6.5 it can be

seen that as Q_C increases the final drop sizes decrease for all three solutions in agreement with the findings by Wong et al. (2017) and Fu et al. (2016). With increasing continuous phase flowrate, both the pressure on the side inlet continuous phase channels and the shearing effects along the interface increase and favour the thinning of the neck. As a result, the drop formation time decreases and smaller droplets are produced. At low continuous phase flowrates (0.003 cm^3/min to 0.01 cm^3/min) the droplet diameter decreases linearly with Q_C. At high continuous phase flowrates (above 0.02 cm^3/min) though, the relation between the droplet diameter and the Q_C is not linear any more indicating that the formation mechanism changed from the squeezing to the dripping regime.

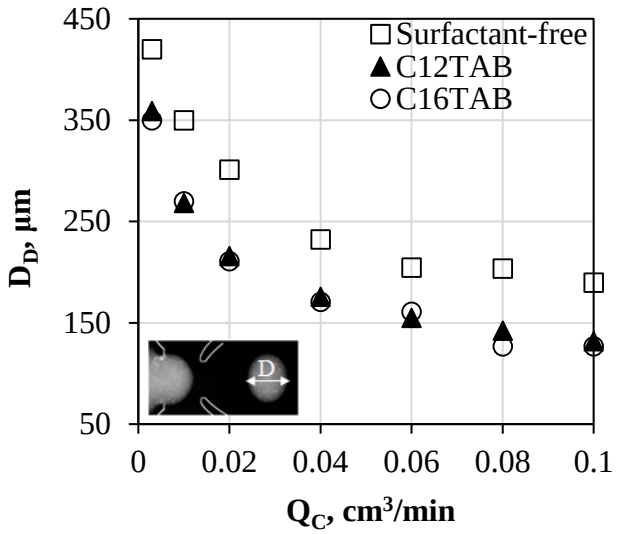

Figure 6.5: Final droplet axial diameter plotted against the continuous phase flowrate for all the aqueous solutionsused. Q_D = 0.01 cm^3/min. Inset: Axial droplet diameter.

The changes in the neck width during the expansion and necking stages are presented in Figure 6.6 for the surfactant-free and the C_{12}TAB solution for all the continuous phase flow rates tested and for different positions of the drop tip in the channel from the end of the cross-junction. The last neck width point shown for each flow rate corresponds to the pinch-off stage. Generally, the neck width decreases with time and with increasing continuous phase flow rate. The decrease of the neck width can be divided in two linear regimes, as shown with the dashed lines (I) and (II) for Q_C = 0.02 cm^3/min in Figure 6.6a. These two lines represent the thinning rate of the neck, while the change in slope corresponds to the transition from the expansion to the necking stage, where the neck curvature also changes. Similar observations on the different neck width regimes have been made by Glawdel et al. (2012a) and Garstecki et al. (2005).

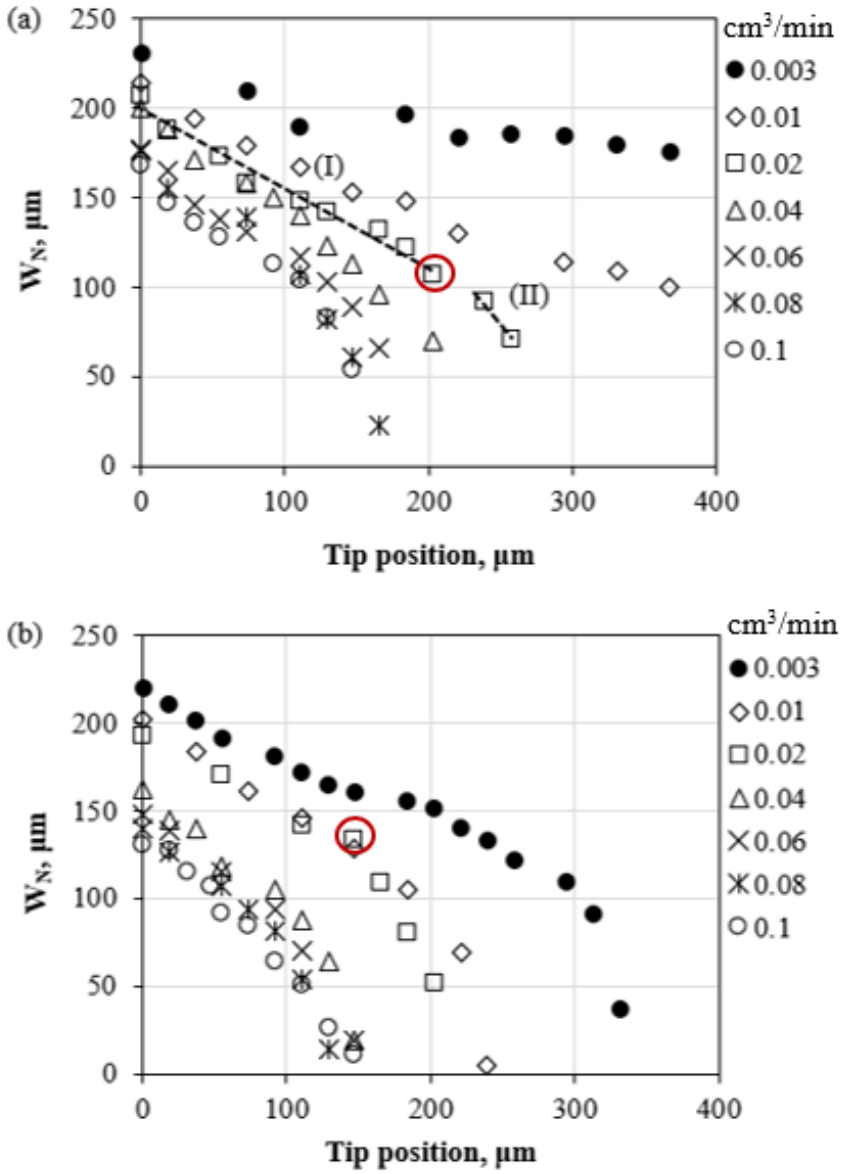

Figure 6.6: (a) Surfactant-free and (b) C_{12}TAB neck width as a function of the tip position for all the continuous phase flowrates studied. Q_D = 0.01 cm^3/min. The dashed lines (I) and (II) have been fitted to the data for Q_C = 0.02 cm^3/min.

The critical width at the transition between the two regimes is found to be below 100 µm (< channel depth / 2) for most of the cases studied, apart from the lowest continuous phase flow rate, Q_C = 0.003 cm^3/min, where the necking stage starts after 170 µm and 150 µm neck width for the surfactant-free and the C_{12}TAB solutions respectively. As the continuous phase flow rate increases, the change in slope from the expansion to the necking stage starts earlier in the channel for the C_{12}TAB solution (Figure 6.6b) compared to the surfactant-free solution i.e. the necking stage starts at ~ 150 µm tip position for the C_{12}TAB case and at ~ 200 µm tip position for the surfactant-free solution which is further down the channel (red circle in Figure 6.6). The

neck width data for C_{16}TAB fall in between those of the surfactant-free and the C_{12}TAB solutions.

The interfacial tension is found to affect the curvature of the droplet leading edge which is mainly controlled by the Laplace pressure (Glawdel and Ren, 2012). The leading edge radius was obtained from the μPIV images and is defined as the radius R_T of a circle fitted to the forming drop tip (Figure 6.7a, Inset). The curvature of the tip increases (radius decreases) with increasing continuous phase flowrate both at the expansion stage (Figure 6.7a) and at the necking stage (Figure 6.7b). Similar to Figure 6.3 and Figure 6.4 for the neck width, the front radius of the C_{16}TAB droplet is close to the pure system one for the expansion stage (Figure 6.7a, especially at high continuous phase flowrates) and to the C_{12}TAB for the necking stage (Figure 6.7b). In general, for the same continuous phase flow rates, the tip radius of the surfactant-laden solutions is smaller than that of the surfactant-free system, because of the lower surface tension. During droplet formation, the tip radius increases as the droplet grows into the main channel.

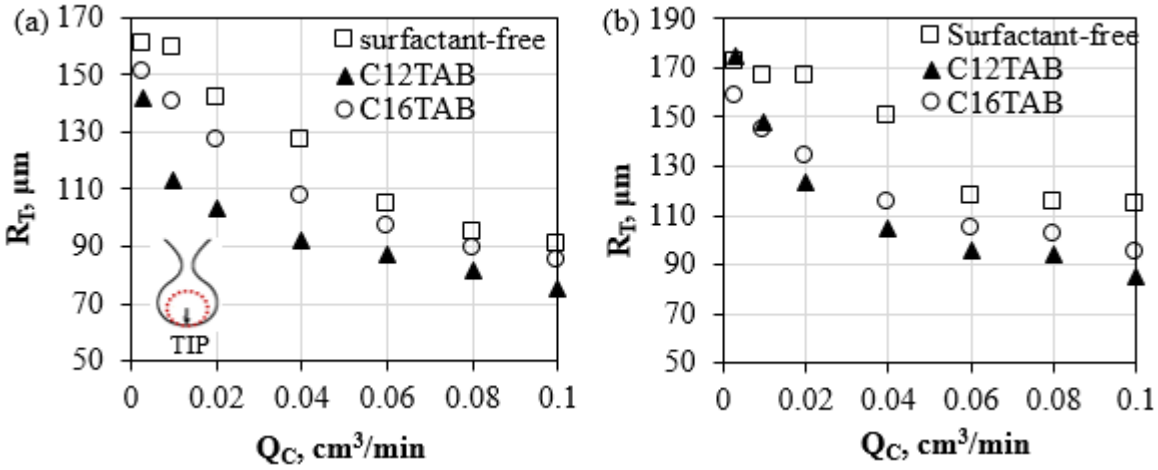

Figure 6.7: Effect of the continuous phase flowrate on the front radius of the forming drop at the (a) end of the expansion and (b) end of the necking stage. Q_D = 0.01 cm^3/min. Inset: Front radius of the droplet.

6.4 Force balance and velocity fields during drop formation

6.4.1 Force balance during drop formation

The droplet formation in the flow-focusing device is considered to be dominated by the balance between the interfacial tension force that acts against the detachment of the droplet and the drag force by the continuous phase, which pulls the droplet downstream. The formation of the neck starts once the drag force becomes sufficiently large and exceeds the interfacial tension force. Figure 6.8 illustrates the forces that act on the droplet in the flow direction (y-direction) at the necking stage.

The shear stress and the pressure gradient arising in the continuous phase as the droplet grows into the main channel, lead to a drag force, F_D that promotes the drop detachment. The drag force applied by the continuous phase on the droplet acts in the positive y-direction and is defined based on Equation 4.6 (Husny and Cooper-White, 2006) using the diameter of the drop as the characteristic parameter:

$$F_D = 4 \cdot \mu_C \cdot \frac{(2m+3)}{(m+1)} \cdot \frac{1}{D_D} \cdot (U_C - U_D) \cdot \frac{\pi D_D^2}{4} = \pi \cdot \mu_C \cdot \frac{(2m+3)}{(m+1)} \cdot D_D \cdot (U_C - U_D) \quad \text{(Equation 6.1)}$$

where μ_C is the continuous phase viscosity, m is the viscosity ratio between the two phases $m = \mu_C/\mu_D$, D_D is the droplet diameter, U_C is the averaged continuous phase velocity measured in front of the tip and U_D is the averaged dispersed phase velocity measured at the drop tip.

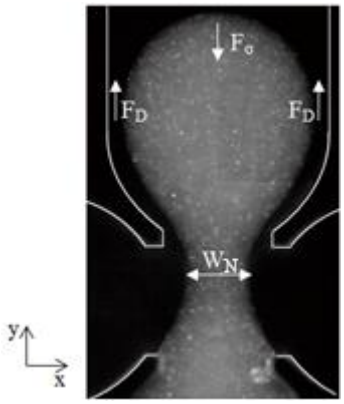

Figure 6.8: Schematic indicating the drag force (F_D) and the interfacial tension force ($F\sigma$) during the necking stage.

The interfacial tension force acts in the negative direction of the flow opposing the drop detachment. The interfacial tension force acting on the droplet is found from the Laplace pressure difference on the drop surface and is given by (similar to Equation 4.4):

$$F_\sigma = -\sigma \cdot \left(\frac{1}{R_T} + \frac{2}{h}\right) \cdot \left(\pi \cdot \frac{W_N^2}{4}\right) \qquad \text{(Equation 6.2)}$$

where σ is the interfacial tension, R_T is the leading edge radius of the drop, h is the height of the channel and W_N is the neck width (Figure 6.8). For the surfactant-free system, the interfacial tension σ is constant and equal to 29 mN/m. The interfacial tension of the C_{12}TAB solution will be assumed to be constant and equal to the equilibrium value, σ = 10 mN/m, for all the formation stages. This assumption is based on the fact that the dynamic surface tension of C_{12}TAB surfactant reaches the equilibrium value very fast. The use of the equilibrium value is further justified given the approximate nature of the model which considers forces acting on the whole drop following similar approaches in the literature (Christopher et al., 2008; Glawdel et al., 2012b; Husny and Cooper-White, 2006), as well as the lack of knowledge of dynamic interfacial tension.

These forces will be further used to explain the droplet formation in the dripping regime along with the velocities obtained with the PIV.

6.4.2 Velocity fields inside and outside a forming drop in the dripping regime

The images and the velocity fields obtained from the two-colour PIV measurements can reveal how the surfactants alter the drop formation process and the flow fields inside and outside the droplet. Figure 6.9 and Figure 6.10 show the averaged total velocity fields at 4 different tip positions during the drop formation process of the surfactant-free and the surfactant-laden 50 mM C_{12}TAB solutions respectively for the same continuous and dispersed phase flowrates.

In the surfactant-free solution a circulation pattern can be observed inside the forming drop while on the sides the dispersed phase velocity has large values (Figure 6.9a). The recirculation happens because after the droplet detachment, the dispersed phase pulls back slightly into its inlet channel before it moves forward again into the flow-focusing channel. During this recirculation, the aqueous solution is mainly transported to the tip via the sides of the droplet as the middle part moves at low velocity while at the same time the continuous phase obstructs

the growth of the droplet. As a result, the droplet was fount to grow mainly in the radial direction during the expansion stage (Figure 6.9a). Under constant dispersed phase flowrate, the droplet enters into the main channel, the circulation area moves gradually forward and weakens while the velocities increase. At the same time, the plug obstructs the flow of the continuous phase that has to travel through a smaller cross-sectional area next to the wall (Figure 6.9b) These observations also agree with the results by Timgren et al. (2008) who studied the velocity fields inside and outside of a forming oil drop in a cross-flow rectangular channel using PIV.

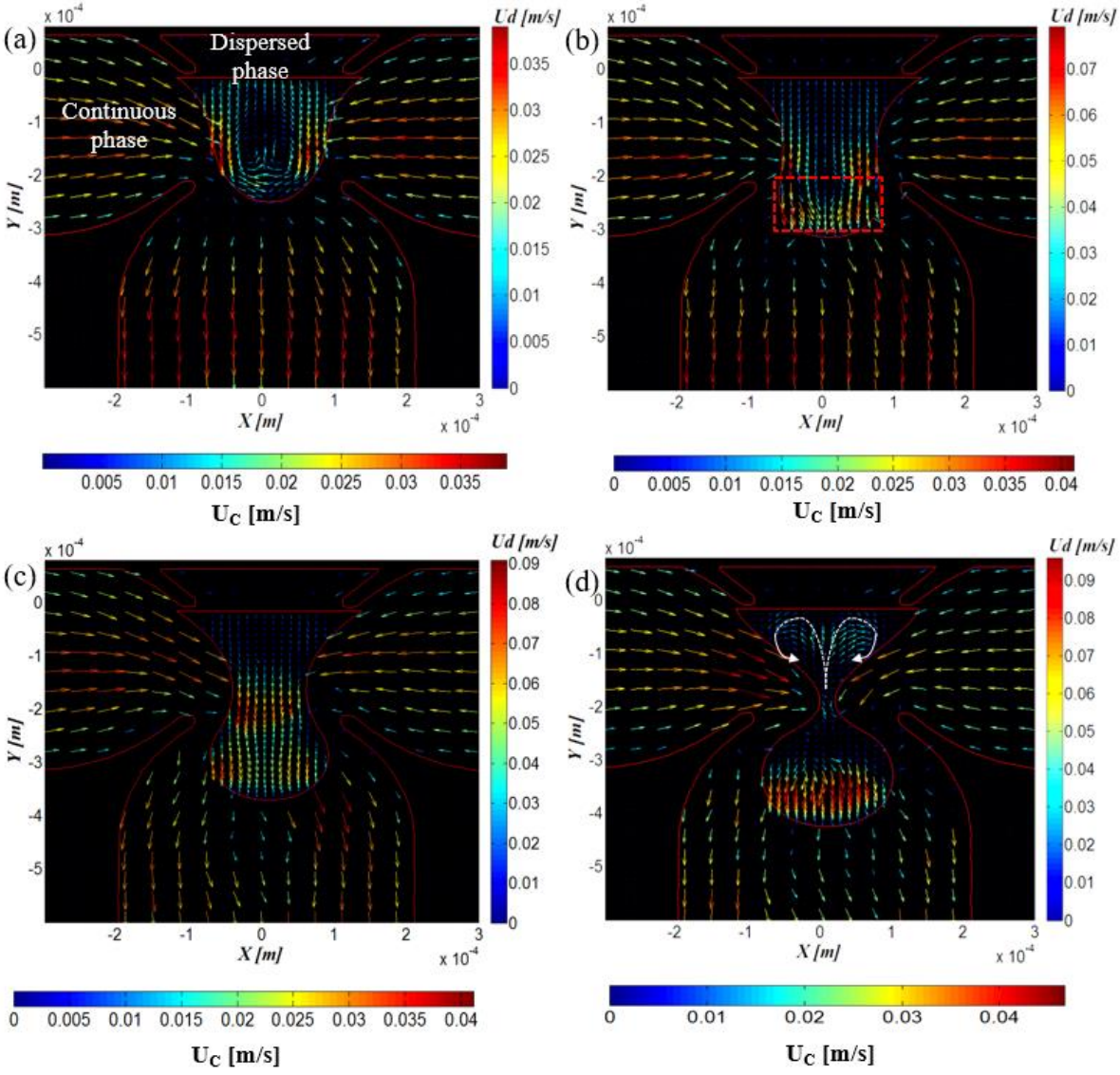

Figure 6.9: Averaged total velocity fields inside and outside the forming surfactant-free droplet. Q_D = 0.01 cm^3/min and Q_C = 0.08 cm^3/min. Droplet diameter is equal to 203 μm. Images (a), (b), (c) and (d) correspond to tip positions 0, 74, 129 and 166 μm respectively. Inset: Dotted rectangle indicates the region used to average the velocity profiles at the top of the droplet.

As a result, the velocity and the pressure inside the continuous phase, at the cross-junction area, increase leading to the change in the neck curvature and to the necking stage (Figure 6.9c). During the pinch–off stage (Figure 6.9d) the velocity acquires large values at the top part of the droplet. As the neck width reduces at a fast rate, a flow inversion at the neck can be observed leading to a weak recirculation at the base of the droplet. It appears that the neck is stretched over two opposite directions (in the main channel by the continuous phase and towards the inlet by the flow reversal in the dispersed phase) that lead eventually to the neck break up. Once the drop has detached, the dispersed phase pulls back into its inlet channel under the action of surface tension.

During the formation of the C_{12}TAB droplet (Figure 6.10), a recirculation pattern cannot be observed during the expansion stage (Figure 6.10a). As the droplet moves into the main channel, the velocity is more uniform and acquires larger values at the top part of the droplet ($V_T \sim 0.076$ m/s) (Figure 6.10b) compared to the surfactant-free case ($V_T \sim 0.065$ m/s) in Figure 6.9b. The differences of the C_{12}TAB system compared to the pure one can be attributed to the accumulation of surfactant to the tip of the droplet. The non-uniform distribution of surfactant inside the droplet (high concentration at the tip and low concentration at the sides of the droplet) creates areas with high (at the low surfactant concentration areas) and low (at the high surfactant concentration areas) surface tension values. As a result, surface tension gradients arise pulling the fluid inside the droplet towards the dispersed phase channel. This motion prevents the recirculation inside the drop. In addition the local accumulation of the surfactant would increase the rigidity of the interface and reduce any velocity gradients inside the drop. Riaud et al. (2018) who studied both numerically and experimentally the dynamics of surfactants during drop formation in a T-junction, found similar results at the expansion stage. The authors suggested that the accumulation of surfactants at the tip of the drop prevents recirculation inside the dispersed phase, makes the interface more rigid and leads to a more uniform velocity field compared to the surfactant-free case.

Figure 6.11 presents this difference in the averaged axial velocity profiles at the top part of the droplet (see dotted rectangle, Figure 6.9) between the surfactant-free and C_{12}TAB systems based on Figure 6.9a and b, Figure 6.10a and b respectively. As can be seen in Figure 6.11, during the first tip position (Figure 6.9a and Figure 6.10a) the highest velocity values are at the side of the droplet whereas the lowest values are in the middle, which show that the fluid is mainly transported through the sides of the dispersed phase. As the C_{12}TAB drop enters into the main channel (Figure 6.9b and Figure 6.10b), high velocities appear in the top part of the

droplet whereas in the surfactant-free system the highest velocities can still be seen at the sides of the droplet (Figure 6.11).

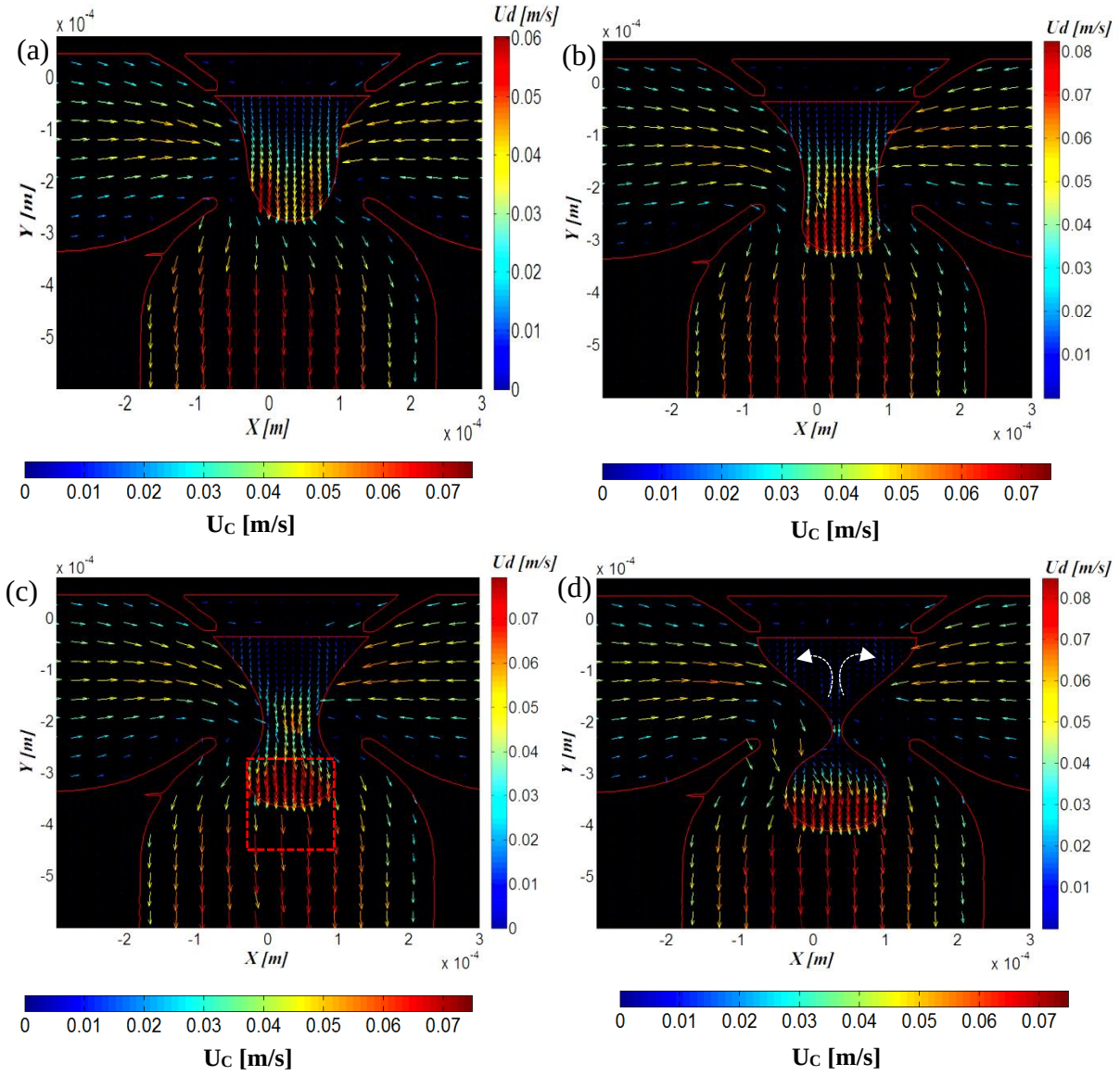

Figure 6.10: Averaged total velocity fields inside and outside the forming C_{12}TAB droplet. Q_D = 0.01 cm^3/min and Q_C = 0.08 cm^3/min. Droplet diameter is equal to 142 μm. Images (a), (b), (c) and (d) correspond to tip positions 0, 55, 92 and 129 μm respectively. Inset: Dotted rectangle indicates the region where the velocity difference between the two phases was calculated.

During the necking and pinch-off stage, the highest velocities are in the middle of the C_{12}TAB droplet (Figure 6.10c and d). This is different from the work by Carrier et al. (2015) who showed that during the growth of the droplet into the channel a weak recirculation pattern forms inside the newly forming droplet (aqueous SDS solution). They found the same recirculation pattern at the necking stage where the dispersed fluid is still transported to the tip

via the sides of the droplet. As can been seen in Figure 6.9, in the surfactant-free system high velocities can be still found at the sides of the droplet at the necking stage and only at the pinch-off stage the highest velocities appear along the tip.

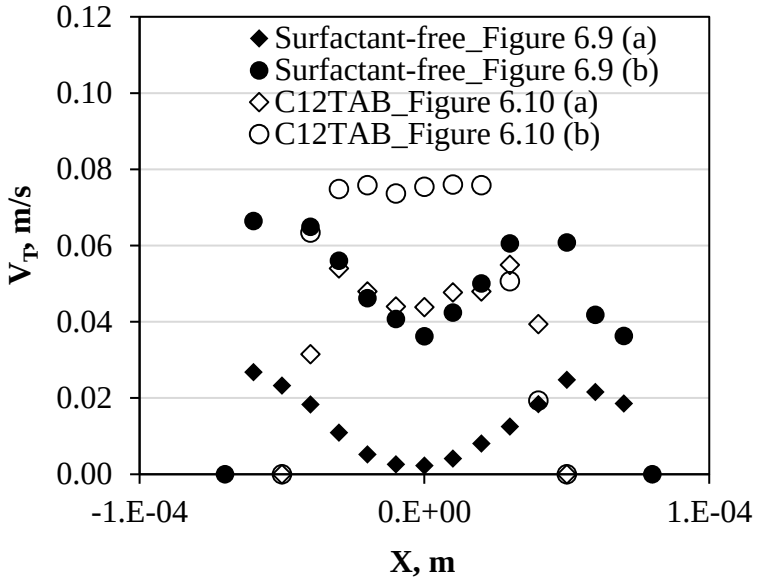

Figure 6.11: Averaged axial velocity profiles at the top part of the droplet for the surfactant-free and the C_{12}TAB solutions.

The necking stage of the C_{12}TAB droplet (Figure 6.10c) can be identified by an increase in the aqueous phase velocity in the neck region. The velocity vectors in the organic phase in Figure 6.10c are almost perpendicular to the aqueous/oil interface at the cross-junction inlet (similar to the surfactant-free case) leading to the thinning of the neck. At this stage, the local velocity difference at the top of the droplet between the two phases (see Inset, Figure 6.10c) is larger (U_D = 0.045 m/s; U_C = 0.022 m/s) than in the surfactant-free solution (U_D = 0.071 m/s; U_C = 0.056 m/s) (Figure 6.9c). During the pinch–off stage (Figure 6.10d) a less intense recirculation pattern, compared to the one in the surfactant-free case, can be observed at the base of the droplet. Carrier et al. (2015) who studied the formation of SDS droplets in a flow-focusing channel also reported a flow inversion and weak recirculation at the base of the dispersed phase during the pinch off stage.

The evolution of the forces at the different steps of the drop formation can be seen in Figure 6.12a and b for the surfactant-free and the C_{12}TAB solutions respectively. The forces were calculated based on Equation 6.1 and Equation 6.2 using the data obtained from the experiments. The inertia force of the dispersed phase was found to be of the order of magnitude of $10^{-10}\,\frac{\mathrm{kg\cdot m}}{\mathrm{s^2}}$ and was not taken into account. As the droplet grows into the main channel, the difference in the local velocities between the continuous and the dispersed phase increase

(Figure 6.9 and Figure 6.10).This leads to an increase in the shear imposed by the continuous phase. At the same time, the pressure gradient in the continuous phase increases as the droplet size increases and blocks the flow-focusing inlet.

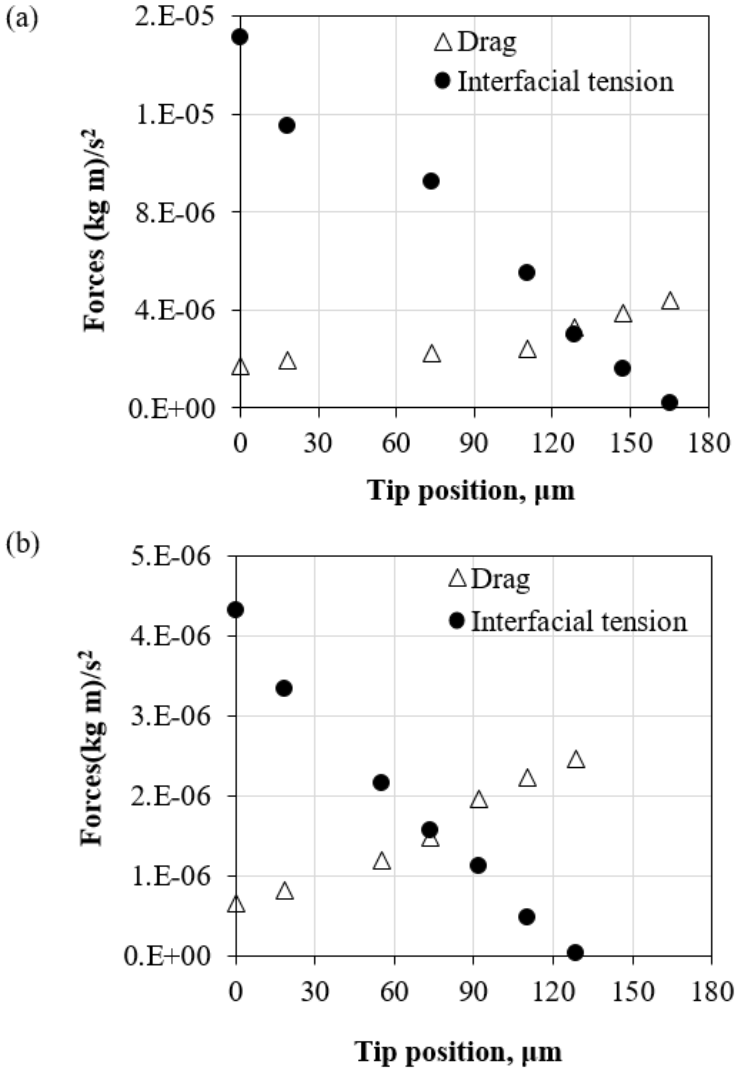

Figure 6.12: Forces during the formation of (a) surfactant-free and (b) C_{12}TAB surfactant-laden droplets. Q_D = 0.01 cm^3/min and Q_C = 0.08 cm^3/min.

As a result, the drag force gradually increases and overcomes the interfacial tension force at different tip positions (Figure 6.12a and b); this is the point where the rate of the neck thinning changes and the transition from the expansion to the necking stage starts (see also Figure 6.6 for the experimental condition Q_D = 0.01 cm^3/min and Q_C = 0.08 cm^3/min). The last points of the drag and interfacial tension forces that appear in Figure 6.12a and b correspond to pinch-off.

The axial velocity at the neck averaged over 40 PIV images is plotted in Figure 6.13 at different drop tip positions for both fluid systems. As can be seen, the velocity increases up to

the necking stage where it starts to decrease again until rupture occurs. In agreement with Figure 6.9 and Figure 6.10 the average velocity is higher for the surfactant-laden system where there is no recirculation.

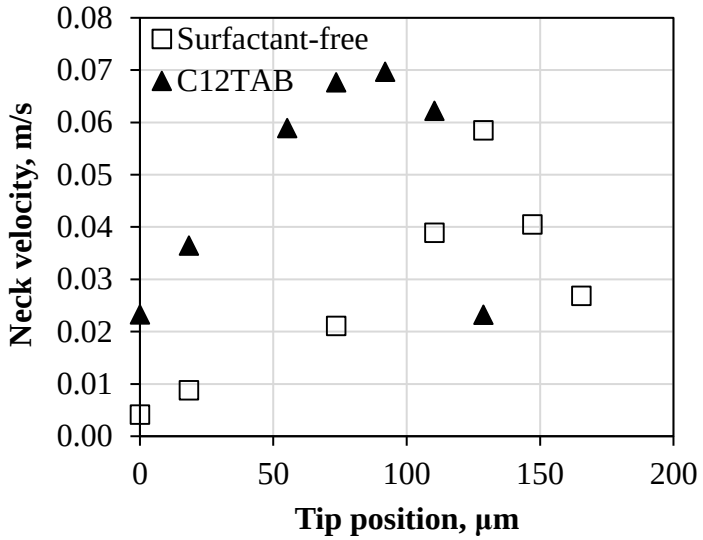

Figure 6.13: Averaged velocity at the neck obtained from PIV (Q_D = 0.01 cm^3/min and Q_C = 0.08 cm^3/min).

6.5 Overview and main conclusions

The flow patterns and drop formation process were studied in a flow focusing microfluidic device using silicon oil as the continuous phase and water/glycerol aqueous solutions that contained different concentrations of surfactants as the dispersed phase. The two-colour Particle Image Velocimetry technique was used to obtain the flow fields in both phases and the characteristics of the forming drops.

It was found that the addition of surfactants reduced the areas of the squeezing and dripping regimes in a flow pattern map with the flowrates of the two phases as coordinates, whereas it extended the areas occupied by the threading and jetting regimes. The droplet formation process in the squeezing and dripping regimes was divided in three distinct periods, namely expansion, necking and pinch-off. The neck width reached at the end of the expansion and the necking stages was found to be depended on the continuous phase flowrates and on the type of surfactant. It was proposed that the dynamic interfacial tension of the different surfactant solutions, rather than the equilibrium one, explained the differences between the two surfactant systems. The rate of reduction of the neck width increased from the expansion to the necking stage. In general, the drops produced in the surfactant-laden solutions were smaller with higher

tip curvature than in the surfactant free one. The velocity profiles in the dripping regime showed that during the expansion period, an internal circualtion appeared at the center of the forming drop which gradually weakened as the droplet moved into the main channel. This circulation was less prominent in the surfactant-laden system which was attributed to the accumulation of surfactants at the drop tip. As the drop propagated in the main channel and the neck decreased in size, the velocities increased in the neck region. During pinch–off, a flow inversion at the thinnest part of the neck was observed which caused the dispersed phase to pull back into the inlet channel after the drop had detached. In general, the averaged velocity fields revealed that the addition of surfactants increased the local velocities difference between the two phases compared to the surfactant-free case, for the same phase flowrates. Based on the geometric characteristics of the forming drop and the velocity fields obtained with PIV, the forces acting on the drop were estimated. It was found that drag forces overcome the surface tension ones between the expansion and the necking drop formation stages.

7. Chapter: Conclusions and future developments

An overview of the main findings of this work along with their impact are discussed next. The conclusions from each chapter are presented and recommendations for future studies are suggested.

7.1 Main findings of the thesis

This thesis investigated the hydrodynamic characteristics of liquid-liquid flows in small channels using an innovative optical technique, namely two-colour Particle Image Velocimetry. In particular, flows with non-Newtonian fluids and in the presence of surfactants were studied.

The main literature was summarized illustrating the need for detailed observations and measurements during liquid-liquid flows of complex fluids in small channels. The flow patterns that can occur in small channels were presented along with the physical mechanisms that control the plug (or droplet) formation and flow. The theoretical background of drop formation in different channel geometries (T-junction, flow-focusing) was also given to enhance understanding of droplet formation and manipulation. Finally, the basic principles behind the Particle Image Velocimetry technique were explained.

In addition, a detailed description of the liquids and the experimental setup used in the thesis were provided. The properties of the complex fluids (xanthan gum and surfactant-laden solutions) were given together with the characterization methods used for the solutions. The characteristics of the two different channel geometries i.e. T-junction and flow-focusing, that were utilized for the flow experiments were also presented along with a thorough description of the two-colour micro-PIV technique. Finally, the methodologies used to analyse the PIV images and to acquire the local velocities of both phases were presented.

The plug formation of non-Newtonian (1000 ppm and 2000 ppm solutions) and Newtonian (low viscosity silicone oil) liquids in the squeezing regime inside a T-junction inlet of a microchannel was investigated. The effects of flowrate and shear-thinning viscosity on the hydrodynamic characteristics and the velocity profiles of both phases were studied using the PIV technique. For the flowrates examined, two flow regimes were identified, namely plug and parallel flow. However, the addition of polymer was found to extend the area of plug flow to higher superficial phase velocities compared to the Newtonian case indicating that with xanthan

gum the rheology can be tuned according to the needs of an application and the characteristics of the flow can change even at low flowrates . During the plug formation, three distinct drop formation stages were identified, namely expansion, necking and pinch-off. The experimental results also revealed that the increase in xanthan gum concentration shifted the neck break-up location further downstream inside the channel and resulted in smaller neck widths, bullet-shaped plugs, and higher continuous phase velocities. From the shear rates measured, the viscosity profiles were calculated, which showed an increase in the non-Newtonian viscosity from 0.01 Pa s (close to the channel wall) to 0.15 Pa s (in the middle of the channel), confirming that the polymer solutions were in the shear-thinning region. The forces acting on the forming plugs were estimated and showed that during plug formation, the drag force gradually increased and overcame the interfacial tension force at the end of the necking stage and beginning of the pinch-off stage. The experimental results revealed that the onset of the pinch-off stage happened when the neck curvature changed from convex to concave.

In addition, the hydrodynamic characteristics of the plug flow of the non-Newtonian shear-thinning aqueous solutions in the oil phase were studied in the main channel, further from the T-junction inlet. The increase in xanthan gum concentration produced longer, bullet-shaped plugs and increased the thickness of the film surrounding them. The longer plug lengths however, may not necessarily mean that the plugs have larger volumes. From the PIV images collected it was found that the plug volumes actually decreased with increasing amount of polymer added in the aqueous phase; this is because the thickness of the film surrounding the plugs increased. The film thickness for the shear-thinning solutions was found to be higher by a factor 4 (for $0.007 < Ca < 0.027$) compared to the Newtonian data in the literature that report a maximum increase of the film thickness by a factor of 2 (even at higher Ca number i.e. $0.003 < Ca < 0.180$). Finally, the circulation times in the aqueous phase were found to increase with the concentration of xanthan gum.

Different surfactant absorption kinetics were also investigated during the formation of an aqueous droplet in an organic continuous phase inside a flow-focusing microchannel. Four flow regimes were identified, namely squeezing, dripping, jetting and threading, whose boundaries changed when the surfactants were present. The drop formation process and the velocity profiles in both phases in the squeezing and dripping regimes were studied in more detail using the micro-PIV technique. For all solutions studied, three distinct drop formation stages were identified, expansion, necking and pinch-off. The surfactant-laden solutions produced smaller drops with larger tip curvature than the surfactant free system. The mechanistic model that was developed to describe the evolution of the forces acting on the

droplet showed that the drag force overcame the interfacial tension force at the transition between the expansion and necking stages. During this transition, the curvature of the neck changed while the thinning rate of the neck was increased.

7.1 Future developments

To design and fully characterize liquid-liquid interfaces in micro-scale with complex fluids, thorough investigations in many areas are still required.

- **Improvements and further development of the PIV technique and Matlab codes**

To visualize the flow profile of each phase while using the two-colour μ-PIV technique, tracer particles with different fluorescent characteristics are mixed into each phase separately. The selection of the right kind of particles for a given application is a demanding procedure especially for the organic phase for which there are few commercial particles. In the current work, two different particles were used: (1) polystyrene microspheres particles that were diluted after a drying process in the organic phase and (2) silica particles that were in a powder form and were suspended directly in the oil phase. Although the silica particles were found to work better with the oil during the experiment (regarding the degree of agglomeration) compared to the polystyrene ones, after 1 day of settling down they started creating large clusters. The ultrasound bath had to be used again to reduce or break these clusters increasing, as a result, the experimental time. To optimize this procedure, several hydrophobic particles made from different materials should be further tested.

The tools used for the PIV imaging processing are routines processed in Matlab. The structure of these routines and the code lines has a great impact on the quality of the outcome and the processing time. Although the current codes produce adequately results, regarding the quality, further improvements can be made. For example, minimization of the code length would decrease the running time and optimize the process.

- **Time-resolved experiments on droplet formation process**

One of the challenges of the current micro-PIV system, is the low acquisition frequency (7 Hz). This is because the fluorescent tracers diluted in the organic phase have low intensity and consequently the use of sensitive low speed camera (low frequency) is necessary. As a result, the drop (or plug) formation process could not be resolved in time. Instead, image pairs were acquired at different drop (or plug) positions inside the channel and were placed in order based

on hydrodynamic characteristics like droplet tip and droplet neck location using Matlab codes developed in-house. However, the drop (or plug) formation and meniscus breakage at the inlet of a channel are fast and require high-speed visualization systems (over 1 kHz). Using a high-speed μPIV technique, the evolution of a forming interface can be captured in time while the absorption of surfactants by the interface and the effects of the polymers on the formation process can be investigated in more detail.

- **Rheology and dynamic interfacial tension study**

A more detailed rheology study (e.g. effects of elasticity on neck thinning) and experiments with different xanthan gum concentrations are needed to explain further the flow behaviour of non-Newtonian fluids and how they affect the flow properties and the formation of two-phase flow system. In addition, a thorough investigation of the droplet formation process under different concentrations of surfactants is essential to understand the effects of interfacial tension and the dynamics of surfactant absorption. The importance of dynamic interfacial tension on drop formation have been discussed previously (Glawdel and Ren, 2012; Kovalchuk et al., 2018; Riaud et al., 2018). In particular, it was shown that microfluidics is a promising tool for measurement of dynamic interfacial tension on short time scales up to sub-millisecond range (Arratia et al., 2008; Steegmans et al., 2010; Wang et al., 2009). Furthermore, the lack of systematic study on the effect of surfactants (CMC value) on flow regimes indicates that more investigations are needed towards that direction.

- **Hydrodynamics of plug flow: film thickness**

Future investigations should focus on film thickness measurements during liquid-liquid plug flow in small channels. Our experimental data showed that the thickness of the continuous phase film between the plug and the channel wall increased with increasing concentration of the polymer in the continuous phase and with increasing dispersed phase velocity. Using a modified Capillary number to account for the non-Newtonian continuous phase viscosity, the existing models from the literature were not able to predict both Newtonian and non-Newtonian film thickness data satisfactory. As most of the predictive models refer to gas-liquid flows or liquid-liquid flows with relatively low visocity fluids more investigations are needed with complex fluids.

- **Predictive tools**

The development of a unified theory for the prediction of flow patterns that would be independent of the fluid and microchannel characteristics should be further investigated. The relative forces acting on the two phases could be identified and used to correlate the flow regimes. The absence of this kind of theory is due to (a) the wide variation that the physical properties of the two liquids can have and (b) the similar experimental conditions that have been used in studies so far. Future investigations should also focus on linking the plug (drop) formation characteristics with the plug (drop) propagation to produce theoretical models for liquid-liquid flows when complex fluids are involved.

8. References

Adrian, R., Westerweel, J., 2011. Particle Image Velocimetry. Cambridge University Press, New York.

Angeli, P., Gavriilidis, A., 2008. Hydrodynamics of Taylor flow in small channels: a review. Proc Inst Mech Eng C J Mec 222, 737–751.

Anna, S., 2016. Droplets and Bubbles in Microfluidic Devices. Annu. Rev. Fluid Mech 48, 285–309.

Anna, S., Bontoux, N., Stone, H., 2003. Formation of dispersions using flow focusing in microchannels. Applied physics letters 82, 364-366.

Arratia, P., Gollub, J., Durian, D., 2008. Polymeric filament thinning and breakup in microchannels. PHYSICAL REVIEW E 77, 1-6.

Astarita, G., Marrucci, G., 1974. Principles of non-Newtonian fluid mechanics. McGraw-Hill.

Aussillous, P., Quere, D., 2000. Quick deposition of a fluid on the wall of a tube. Phys. Fluids 12, 2367–2371.

Baret, J., Kleinschmidt, F., Harrak, A., Griffiths, A.D., 2009. Kinetic Aspects of Emulsion Stabilization by Surfactants: A Microfluidic Analysis. Langmuir 25, 6088–6093.

Berry, J., Neeson, M., Dagastine, R., Chan, D., Tabor, R., 2015. Measurement of surface and interfacial tension using pendant drop tensiometry. Journal of Colloid and Interface Science 454, 226-237.

Boogar, R., Gheshlaghi, R., Mahdavi, M., 2013. The effects of viscosity, surface tension and flow rate on gasoil – water flow pattern in microchannels. Korean J. Chem. Eng 30, 45-49.

Bretherton, F., 1961. The motion of long bubbles in tubes. Journal of Fluid Mechanics 10, 166–188.

Broder, D., Sommerfeld, M., 2002. An Advanced LIF-PLV System for Analysing the Hydrodynamics in a Laboratory Bubble Column at Higher Void Fractions. Experiments in Fluids 33, 826-837.

Carrier, O., Ergin, G., H Li, Watz, B., Funfschilling, D., 2015. Time-resolved mixing and flow-field measurements during droplet formation in a flow-focusing junction. J. Micromech. Microeng. 25.

Chen, X., Glawdel, T., Cui, N., Ren, C.L., 2015. Model of droplet generation in flow focusing generators operating in the squeezing regime. Microfluid Nanofluid 18, 1341–1353.

Chen, X., Ren, C., 2017. Experimental study on droplet generation in flow focusing devices considering a stratified flow with viscosity contrast. Chemical Engineering Science 163, 1-10.
Chiarello, E., Derzsi, L., Pierno, M., Mistura, G., Piccin, E., 2015. Generation of Oil Droplets in a Non-Newtonian Liquid Using a Microfluidic T-Junction. Micromachines 6, 1825-1835.
Chiarello, E., Gupta, A., Mistura, G., Sbragaglia, M., Pierno, M., 2017. Droplet breakup driven by shear thinning solutions in a microfluidic T-Junction. PHYSICAL REVIEW FLUIDS 2.
Chinaud, M., Roumpea, E., Angeli, P., 2015. Studies of plug formation in microchannel liquid–liquid flows using advanced particle image velocimetry techniques. Experimental Thermal and Fluid Science 69, 99–110.
Christopher, G., Anna, S., 2007. Microfluidic methods for generating continuous droplet streams. Journal of Physics D: Applied Physics 40, 319-336.
Christopher, G., Noharuddin, N., Taylor, J., Anna, S., 2008. Experimental observations of the squeezing-to-dripping transition in T-shaped microfluidic junctions. PHYSICAL REVIEW E 78, 036317.
Cubaud, T., Mason, T.G., 2008. Capillary threads and viscous droplets in square microchannels. Physics of Fluids 20, 053302.
Deshmukh, S., Joshi, J., Koganti, S., 2008. Flow Visualization and Three-Dimensional CFD Simulation of the Annular Region of an Annular Centrifugal Extractor. Industrial & Engineering Chemistry Research 47, 3677–3686.
Dessimoz, A., Cavin, L., Renken, A., Kiwi-Minsker, L., 2008. Liquid-liquid two-phase flow patterns and mass transfer characteristics in rectangular glass microreactors. Chemical Engineering Science 63, 4035-4044.
Dore, V., Tsaoulidis, D., Angeli, P., 2012. Mixing patterns in water plugs during water/ionic liquid segmented flow in microchannels. Chem Eng Sci 80, 334-341.
Dummann, G., Quittmann, U., Groschel, L., Agar, D., Worz, O., Morgenschweis, K., 2003. The capillary-microreactor: a new reactor concept for the intensification of heat and mass transfer in liquid-liquid reactions. Catalysis Today 79-80, 433-439.
Eain, M., Egan, V., Punch, J., 2013. Film thickness measurements in liquid-liquid slug flow regimes. International Journal of Heat and Fluid Flow 44, 515-523.
Foroughi, H., Kawaji, M., 2011. Viscous oil–water flows in a microchannel initially saturated with oil: Flow patterns and pressure drop characteristics. International Journal of Multiphase Flow 37, 1147-1155.
Fu, T., Ma, Y., Funfschilling, D., Li, H., 2009. Bubble formation and breakup mechanism in a microfluidic flow-focusing device. Chemical Engineering Science 64, 2392 -- 2400.

Fu, T., Ma, Y., Funfschilling, D., Li, H., 2011. Bubble formation in non-Newtonian fluids in a microfluidic T-junction. Chemical Engineering and Processing 50, 438–442.

Fu, T., Ma, Y., Li, H., 2016. Breakup dynamics of slender droplet formation in shear-thinning fluids in flow-focusing devices. Chemical Engineering Science 144, 75–86.

Fu, T., Wei, L., Zhu, C., Ma, Y., 2015. Flow patterns of liquid–liquid two-phase flow in non-Newtonian fluids in rectangular microchannels. Chemical Engineering and Processing 91, 114–120.

Funfschilling, D., Debas, H., Li, H.Z., Mason, T.G., 2009. Flow-field dynamics during droplet formation by dripping in hydrodynamic-focusing microfluidics. PHYSICAL REVIEW E 80, 015301.

Ganguli, A., Sathe, M., Pandit, A., Joshi, J., Vijayanb, P., 2010. Hydrodynamics and heat transfer characteristics of passive decay heat removal systems: CFD simulations and experimental measurements. Chemical Engineering Science 65, 3457-3473.

Garstecki, P., Fuerstman, M., Stone, H., Whitesides, G., 2006. Formation of droplets and bubbles in a microfluidic T-junction—scaling and mechanism of break-up. Lab on a Chip 6, 437–446.

Garstecki, P., Stone, H., Whitesides, G., 2005. Mechanism for Flow-Rate Controlled Breakup in Confined Geometries: A Route to Monodisperse Emulsions. PHYSICAL REVIEW LETTERS 94, 164501.

Ghannam, M., Abu-Jdayil, B., Esmail, N., 2014. Experimental Investigation of Crude Oil-Xanthan Emulsions Flow Behavior. Journal of Petroleum Science Research 3, 1-15.

Glawdel, T., Elbuken, C., Ren, C.L., 2012a. Droplet formation in microfluidic T-junction generators operating in the transitional regime. I. Experimental observations. PHYSICAL REVIEW E 85, 016322.

Glawdel, T., Elbuken, C., Ren, C.L., 2012b. Droplet formation in microfluidic T-junction generators operating in the transitional regime. II. Modeling. PHYSICAL REVIEW E 85, 016323.

Glawdel, T., Ren, C.L., 2012. Droplet formation in microfluidic T-junction generators operating in the transitional regime. III. Dynamic surfactant effects. PHYSICAL REVIEW E 86, 026308.

Gupta, A., Kumar, R., 2010. Effect of geometry on droplet formation in the squeezing regime in a microfluidic T-junction. Microfluid Nanofluid 8, 799–812.

Gupta, A., Matharoo, H., Makkar, D., Kumar, R., 2014. Droplet formation via squeezing mechanism in a microfluidic flow-focusing device. Computers & Fluids 100, 218-226.

Harris, J., 1977. Rheology and non-Newtonian flow. Longam Inc, New York.

Husny, J., Cooper-White, J., 2006. The effect of elasticity on drop creation in T-shaped microchannels. J. Non-Newtonian Fluid Mech 137, 121–136.

Irandoust, S., Anderson, B., 1989. Liquid film in Taylor flow through a capillary. Ind. Eng. Chem 28, 1684–1688.

Jin, F., Gupta, N.R., Stebe, K.J., 2006. The detachment of a viscous drop in a viscous solution in the presence of a soluble surfactant. PHYSICS OF FLUIDS 18, 022103.

Jovanovic, J., Zhou, W., Rebrov, E., Nijhuis, T., Hessel, V., Schouten, J., 2011. Liquid-liquid slug flow: hydrodynamics and pressure drop. Chem Eng Sci 66, 42–54.

Kandlikar, S., Grande, W., 2002. Evolution of microchannel flow passages – Thermohydraulic performance and fabrication technology, ASME International Mechanical Engineering Congress & Exposition, Louisiana.

Kashid, M., Agar, D., 2007. Hydrodynamics of liquid–liquid slug flow capillary microreactor: flow regimes, slug size and pressure drop. Chemical Engineering Journal 131, 1-13.

Kashid, M., Gerlach, I., Goetz, S., Franzke, J., Acker, J., Platte, F., Agar, D., Turek, S., 2005. Internal Circulation within the Liquid Slugs of a Liquid-Liquid Slug-Flow Capillary Microreactor. Ind Eng Chem 44, 5003-5010.

Kashid, M., Renken, A., Kiwi-Minsker, L., 2011. Gas–liquid and liquid–liquid mass transfer in microstructured reactors. Chemical Engineering Science 66, 3876-3897.

Kim, S., Wang, T., Zhang, L., Jiang, Y., Li, Z. 2019. Micro-particle image velocimetry visualization study of thermal Buoyant-Marangoni flow in microtubes. International Journal of Heat and Mass Transfer, 137, 765 – 774.

King, C., Walsh, E., Grimes, R., 2007. PIV measurements of flow within plugs in a microchannel. Microfluidics and Nanofluidics 3, 463-472.

Kovalchuk, N., Nowak, E., Simmons, M.J., 2016. Effect of Soluble Surfactants on the Kinetics of Thinning of Liquid Bridges during Drops Formation and on Size of Satellite Droplets. Langmuir 32, 5069−5077.

Kovalchuk, N.M., Roumpea, E., Nowak, E., Chinaud, M., Angeli, P., Simmons, M.J., 2018. Effect of surfactant on emulsification in microchannels. Chemical Engineering Science 176, 139–152.

Lee, W., Walker, L., Anna, S., 2009. Role of geometry and fluid properties in droplet and thread formation processes in planar flow focusing. PHYSICS OF FLUIDS 21, 032103.

Li, L., Yan, Z., Jin, M., You, X., Xie, S., Liu, Z., Berg, A., Eijkel, J., Shui, L. 2019. In-Channel Responsive Surface Wettability for Reversible and Multiform Emulsion Droplet Preparation and Applications. ACS Appl. Mater. Interfaces, 11, 16934-16943.

Li, X., Li, F., Yang, J., Kinoshita, H., Oishi, M., Oshima, M., 2012. Study on the mechanism of droplet formation in T-junction microchannel. Chemical Engineering Science 69, 340–351.

Lindner, A., Bonn, D., Meunier, J., 2000. Viscous fingering in a shear-thinning fluid. Phys Fluids 12, 256-261.

Liu, H., Zhang, Y., 2011. Droplet formation in microfluidic cross-junctions. PHYSICS OF FLUIDS 23, 082101.

Madani, M., Zargar, G., Takassi, A., Daryasafar, A., Wood, D., Zhang, Z., 2019. Fundamental investigation of an environmentally-friendly surfactant agent for chemical enhanced oil recovery. Fuel, 238, 186 – 197.

Mehendale, S., Jacobi, A., Shah, R., 2000. Fluid Flow and Heat Transfer at Micro- and Meso-Scales with Applications to Heat Exchanger Design. Applied Mechanics Review 53, 175-193.

Meyer, C., Hoffmann, M., Schluter, M., 2014. Micro-PIV analysis of gas-liquid Taylor flow in a vertical oriented square shaped fluidic channel. International Journal of Multiphase Flow 67, 140-148.

Muijlwijk, K., Berton-Carabin, C., Schroën, K., 2015. How microfluidic methods can lead to better emulsion products. Lipid Technology 27, 234-236.

Nooranidoost, M., Izbassarov, D., Muradoglu, M., 2016. Droplet formation in a flow focusing configuration: Effects of viscoelasticity. PHYSICS OF FLUIDS 28, 123102.

Oishi, M., Kinoshita, H., Fujii, T., Oshima, M., 2011. Simultaneous measurement of internal and surrounding flows of a moving droplet using multicolour confocal micro-particle image velocimetry (micro-PIV). Measurement Science and Technology 22, 1-13.

Pal, S., Mushtaq, M., Banat, F., Sumaiti, A. 2018. Review of surfactant-assisted chemical enhanced oil recovery for carbonate reservoirs: challenges and future perspectives. Petroleum Science, 15, 77-102.

Riaud, A., Zhang, H., Wang, X., Wang, K., Luo, G., 2018. Numerical Study of Surfactant Dynamics during Emulsification in a T-Junction Microchannel. Langmuir 34, 4980-4990.

Roumpea, E., Kovalchuk, N.M., Chinaud, M., Nowak, E., Simmons, M.J., Angeli, P., 2019. Experimental studies on droplet formation in a flow-focusing microchannel in the presence of surfactants. Chemical Engineering Science 195, 507-518.

Salim, A., Fourar, M., Pironon, J., Sausse, J., 2008. Oil–water two-phase flow in microchannels: flow patterns and pressure drop measurements. The Canadian Journal of Chemical Engineering 86, 978-988.

Sang, L., Hong, Y., Wang, F., 2009. Investigation of viscosity effect on droplet formation in T-shaped microchannels by numerical and analytical methods. Microfluidics and Nanofluidics 6, 621–635.

Santiago, J., Wereley, S., Meinhart, C., Beebe, D., Adrian, R., 1998. A particle image velocimetry system for microfluidics. Experiments in Fluids 25, 316–319.

Sathe, M., Thaker, I., Strand, T., Joshi, J., 2010. Advanced PIV/LIF and shadowgraphy system to visualize flow structure in two-phase bubbly flows. Chemical Engineering Science 65, 2431-2442.

Shinohara, K., Sugii, Y., Aota, A., Hibara, A., Tokeshi, M., Kitamori, T., Okamoto, K., 2004. High-speed micro-PIV measurements of transient flow in microfluidic devices. Measurement Science and Technology 15, 1965-1970.

Silva, G., Leal, N., Semiao, V., 2008. Micro-PIV and CFD characterization of flows in a microchannel: Velocity profiles, surface roughness and Poiseuille numbers. International Journal of Heat and Fluid Flow 29, 1211-1220.

Steegmans, M., Schroen, K., Boom, R., 2010. Microfluidic Y-junctions: A robust emulsification system with regard to junction design. AIChE Journal 56, 1946-1949.

Steijn, V., Kleijn, C., Kreutzer, M., 2010. Predictive model for the size of bubbles and droplets created in microfluidic T-junctions. Lab Chip 10, 2513-2518.

Steijn, V., Kreutzer, M.T., Kleijn, C.R., 2007. μ-PIV study of the formation of segmented flow in microfluidic T-junctions. Chemical Engineering Science 62, 7505 – 7514.

Su, Y., Chen, G., Yuan, Q., 2013. Effect of Viscosity on the Hydrodynamics of Liquid Processes in Microchannels. Chem. Eng. & Tech 37, 427-434.

Su, Y., Zhao, Y., Chen, G., Yuan, Q., 2010. Liquid–liquid two-phase flow and mass transfer characteristics in packed microchannels. Chemical Engineering Science 65, 3947-3956.

Taylor, G., 1961. Deposition of a viscous fluid on the wall of a tube. J Fluid Mech. 10, 161–165.

Thulasidas, T., Abraham, M., Cerro, R., 1997. Flow patterns in liquid slugs during bubble-train flow inside capillaries. Chem Eng Sci 52, 2947–2962.

Tice, J.D., Lyon, A.D., Ismagilov, R.F., 2004. Effects of viscosity on droplet formation and mixing in microfluidic channels. Analytical Chimica Acta 507, 73-77.

Timgren, A., Tragardh, G., Tragardh, C., 2008. Application of the PIV technique to measurements around and inside a forming drop in a liquid–liquid system. Exp Fluids 44, 565–575.

Tsakiroglou, C., 2004. Correlation of the two-phase flow coefficients of porous media with the rheology of shear-thinning fluids. Journal of Non-Newtonian Fluid Mechanics 117, 1-23.

Tsaoulidis, D., Angeli, P., 2016. Effect of channel size on liquid-liquid plug flow in small channels. AIChE Journal 62, 315-324.

Utada, A.S., Fernandez-Nieves, A., Stone, H., Weitz, D., 2007. Dripping to Jetting Transitions in Coflowing Liquid Streams. PHYSICAL REVIEW LETTERS 99, 094502.

Wang, K., Lu, Y.C., Xu, J.H., Luo, G.S., 2009. Determination of Dynamic Interfacial Tension and Its Effect on Droplet Formation in the T-Shaped Microdispersion Process. Langmuir 25, 2153-2158.

Whitesides, G., 2006. The origins and the future of microfluidics. Nature 442, pages 368–373.

Wissen, R., Schreel, K., Geld, C., 2005. Particle image velocimetry measurements of a steam-driven confined turbulent water jet. Journal of Fluid Mechanics 530, 353 - 368.

Wong, V., Loizou, K., Lau, P., Graham, R.S., Hewakandamby, B.N., 2017. Numerical studies of shear-thinning droplet formation in a microfluidic T-junction using two-phase level-SET method. Chemical Engineering Science 174, 157–173.

Xu, J.H., Li, S.W., Tan, J., Luo, G.S., 2008. Correlations of droplet formation in T-junction microfluidic devices: from squeezing to dripping. Microfluid Nanofluid 5, 711–717.

Yao, C., Liu, Y., Xu, C., Zhao, S., Chen, G. 2018. Formation of Liquid–Liquid Slug Flow in a Microfluidic T-Junction: Effects of Fluid Properties and Leakage Flow. AIChE, 64, 346-357.

Zhao, Y., Chen, G., Yuan, Q., 2006. Liquid-Liquid two-phase flow patterns in a rectangular microchannel. AIChE Journal 52, 4052-4060.

Appendix A

The flow pattern remains constant across the length of the channel as can be seen by the images obtained by high-speed camera:

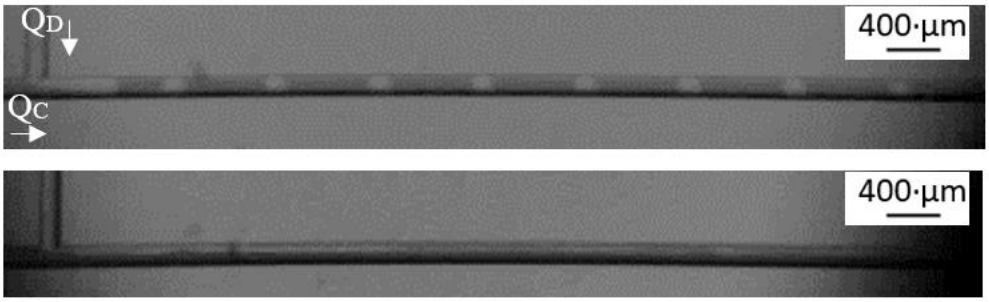

Figure 1: High-speed imaging of (a) plug flow (Q_C = 0.07 cm^3/min; Q_D = 0.02 cm^3/min) and (b) stratified flow (Q_C= 0.07 cm^3/min; Q_D= 0.06 cm^3/min).

The flow pattern map was also obtained using a 3000 Hz high-speed camera (Photron 3000). A white LED backlight with adjustable intensity was used to illuminate the channel. A small amount of commercial, black ink (Pelikan®) was added in the aqueous phase to differentiate between the phases in the captured images. The amount of ink added did not affect the interfacial tension.

Appendix B

The PIV camera calibration was done by using the known distance between the walls A and B (equal to the diameter) of the microchannel (Figure 2).

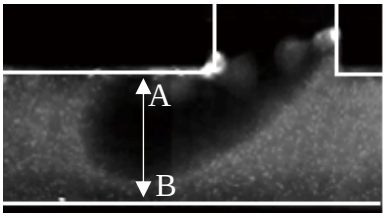

Figure 2: Target image used for PIV camera calibration.

The resolution was found to be 0.35 µm/pixel for the aqueous phase (CCD camera Link® Base with 2x magnification lens and 10x magnification microscope objective) and 0.5 µm/pixel for the organic phase (PCO Sensicam, Dicam pro® with 1x magnification lens and 10x

magnification microscope objective). The syringe pumps (KDS Scientific®), were also calibrated (by collecting an amount of liquid over a period of time) and the maximum uncertainty of the flow rates was ±2%. In addition, the flowrates were checked by measuring the velocity profile of single-phase flow inside the main channel (Figure 3).

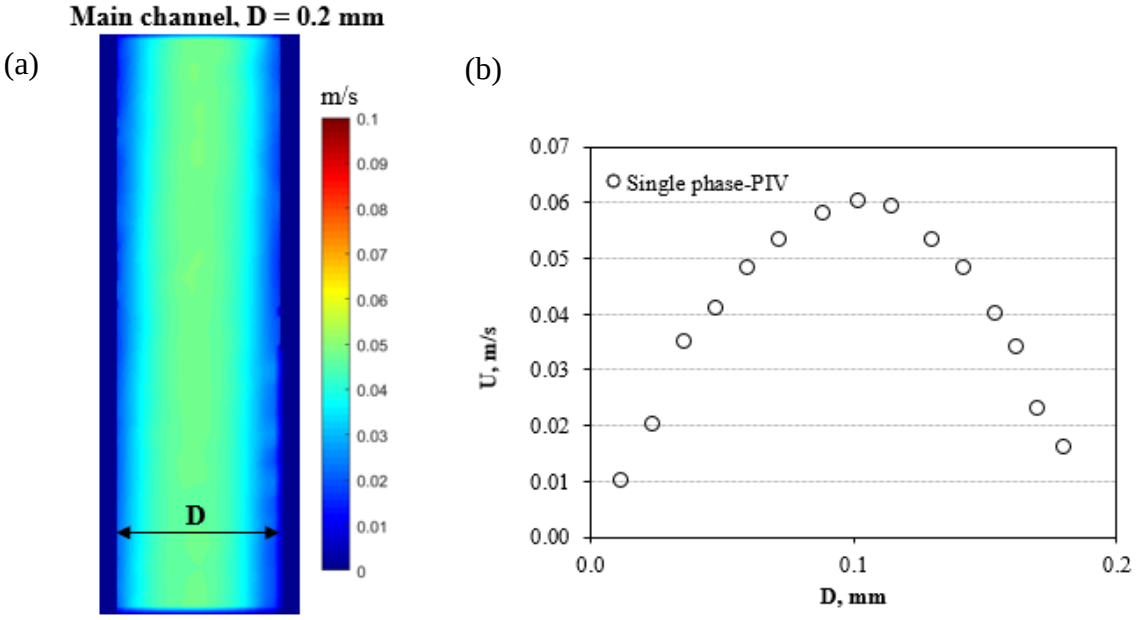

Figure 3: (a) Averaged velocity field of single-phase flow inside the channel captured with PIV (b) Velocity profile of across the channel diameter.

The flowrate was set at 0.06 cm^3/min for a water/glycerol flow. The velocity profiles from 100 images were collected and the experimental averaged velocity profile was calculated (Figure 23b). The mean velocity was found to be equal to 0.03 m/s. This value was compared against the average velocity based on the pump flowrate, Q, which was equal to 0.032 m/s ($u = \frac{Q}{A}$, where A = 3.14E-08 m^2 the cross-section area of the channel), giving a 6% difference from the value found from the velocity profile.

All the PIV data based on pixel measurements (plug length, droplet diameter, width neck, tip radius etc) have a maximum error uncertainty ±2%. All the PIV velocity data have a maximum error uncertainty 0.25 μm for the aqueous phase and 0.20 μm for the organic phase (similar to the uncertainty in locating the correlation peak as explained above).

The calculation of the uncertainty of the forces, is more complicated as the F_σ and F_D depend on more than two parameters. Using combination of errors, the uncertainty, ω, of the forces can be found:

$$\omega_x = \left[\left(\frac{\theta x}{\theta x1}\cdot\omega_{x1}\right)^2 + \left(\frac{\theta x}{\theta x2}\cdot\omega_{x2}\right)^2 + \cdots + \left(\frac{\theta x}{\theta xn}\cdot\omega_{xn}\right)^2\right]^{1/2} \quad \text{Equation 1}$$

where x1, x2,…, xn are the independent variables of a function x = x (x1, x2, …xn) and ω_{x1}, ω_{x2},…., ω_{xn} are the uncertainties of the variables. By solving Equation 1 for the interfacial tension force $F_\sigma = -\left(\sigma \cdot \left(\frac{1}{R_T} + \frac{2}{h}\right) - \sigma \cdot \left(\frac{1}{R_N} + \frac{2}{h}\right)\right) \cdot \left(\pi \cdot \frac{W_N^2}{4}\right)$ and for R_T = 118.9 μm ±2%, R_N = 417.9 μm ±2% and W_N = 50 μm ±2% (last step of formation), it can be found that:

$\frac{\theta F\sigma}{\theta R_T}$ = 0.00442, ω_{R_T} = 2.38E-06

$\frac{\theta F\sigma}{\theta R_N}$ = - 0.00036, ω_{R_N} = 8.36E-06

$\frac{\theta F\sigma}{\theta W_N}$ = - 0.02, ω_{W_N} = 1E-06

} $\omega_{F\sigma}$ = ± 0.05%

Similarly, the uncertainty of the F_D was found ± 0.2% . As for the Ca numbers calculated in the thesis, $Ca = \frac{\mu \cdot U_P}{\sigma}$, the viscosity and interfacial tension values have 0.005 Pa s and 0.001 mN/m uncertainty respectively (the uncertainty of the instrument) resulting thus in 0.025% – 0.074% uncertainty of the Ca number.

The small values of uncertainty of the different data as calculated above (i.e. velocity, plug and drop characteristics etc.) show the high reliability of the PIV measurements. However, there is a variation on plug length, neck width and film thickness data during measurements which is calculated based on standard deviation:

$$S.D = \sqrt{\frac{\sum_{i=1}^{N}(x_i - \bar{x})^2}{N-1}} \qquad \text{Equation 2}$$

where x_1 , x_2 , …., x_N are the values of the sample, $\bar{x}$ is the mean value of the sample and N is the number of the values. The results of standard deviation have been used as error bars in the figures.

Plug lengths were averaged over 200 micro-PIV images with standard deviation for all cases equal to 3.0-15.5% (Figure 5.1d). The film thickness was also averaged over 200 micro-PIV images and the deviation from the sample mean value was calculated 10% for the non-Newtonian solutions and 20% for the Newtonian (Figure 5.8). Depending on the flowrates, about 100-200 of the images were averaged to obtain the neck width during droplet formation. The standard deviation for all cases equal to 4.5-10 % (Figure 6.3). The low standard deviation

values show that each set of PIV data, i.e. plug length, film thickness etc., has small variation and most of the measured values are close to the mean one.